

LONG WAVELENGTH LUMINESCENCE FROM GaInNAsSb  
ON GaAs

A DISSERTATION

SUBMITTED TO THE DEPARTMENT OF MATERIAL SCIENCE AND  
ENGINEERING

AND THE COMMITTEE ON GRADUATE STUDIES

OF STANFORD UNIVERSITY

IN PARTIAL FULFILLMENT OF THE REQUIREMENTS

FOR THE DEGREE OF

DOCTOR OF PHILOSOPHY

Vincent Gambin

November 2002

© Copyright by Vincent Gambin 2003

All Rights Reserved

I certify that I have read this dissertation and that in my opinion it is fully adequate, in scope and quality, as dissertation for the degree of Doctor of Philosophy.

---

James Harris  
(Principal Advisor)

I certify that I have read this dissertation and that in my opinion it is fully adequate, in scope and quality, as dissertation for the degree of Doctor of Philosophy.

---

Paul McIntyre

I certify that I have read this dissertation and that in my opinion it is fully adequate, in scope and quality, as dissertation for the degree of Doctor of Philosophy.

---

Glenn Solomon

Approved for the University Committee on Graduate Studies

---

# Abstract

GaInNAs grown on GaAs has recently been found to optically emit at wavelengths longer than previously thought possible with material grown epitaxially on GaAs substrates. Adding small amounts of N to InGaAs pushes emission to longer wavelengths and offsets the large lattice mismatch between InAs and GaAs. Dilute-nitride GaInNAs alloys have quickly become an excellent candidate for low cost 1.3-1.55  $\mu\text{m}$  vertical cavity surface emitting lasers (VCSELs) and high power edge emitting lasers in the past few years. This has been an exciting discovery since commercially available low cost VCSELs are currently limited to 980 nm emission.

Nitride-arsenide alloys were grown by solid source molecular beam epitaxy (MBE) using a N radio frequency (RF) plasma cell. Due to the difficulties incorporating a significant amount of N in solid solution, growth of GaInNAs is substantially different than earlier III-V systems. Differences in crystal structure, the small size of N compared with As, and the high electronegativity of the N atom, cause a large miscibility gap between GaAs and GaN. The nitride-arsenide based crystal is grown under metastable conditions with low substrate temperatures and a highly reactive N radical plasma source. However, defects generated during this non-equilibrium growth are a source for non-radiative recombination and diminished photoluminescence (PL). By rapid thermal annealing the material after growth, defects are removed from the crystal and the material quality of the GaInNAs films improves significantly. By measuring structural changes that occur during anneal, new insight has been made into the mechanisms which cause the optoelectronic properties to improve.

In an effort to further enhance crystal quality, Sb present during GaInNAs growth is thought to act as a surfactant to maintain surface planarity, and phase coherence, resulting in increased PL efficiency. With the addition of Sb, we have observed both a sharp intensity increase in samples with a high In concentration and a bandgap past 1.3  $\mu\text{m}$ . Thus we have found Sb is not only a surfactant but a significant alloy constituent

which further redshifts the optical emission. Increasing the In or N content in materials with PL over 1.3  $\mu\text{m}$  normally drops optical intensity; however, using Sb, we can maintain high PL efficiency out to 1.6  $\mu\text{m}$ . Since both In and Sb in GaAs add compressive stress and the solubility of N in GaAs is limited, there is a need for GaNAs tensile strain compensating barriers for applications in multiple quantum well, high-intensity devices. With the development of GaInNAsSb alloys and strain compensated barriers, even longer wavelengths are possible on GaAs, greatly strengthening the dilute-nitride system as the technology of the future for long wavelength optoelectronic devices.

# Acknowledgements

I'd like to especially thank my advisor Professor James Harris for his dedicated support in my research and career as a graduate student. Because of his assistance, encouragement, and advice all the work presented here was possible. Thanks Coach!

I'd further like to thank the Material Science and Electrical Engineering faculty at Stanford for their assistance in my research. In particular, I'd like to thank my oral thesis committee Stacy Bent, Mike McGehee, Paul McIntyre, and Glenn Solomon, and my dissertation reading committee Paul McIntyre and Glenn Solomon. I'd also like to thank Gail Chun-Creech and Miho Nishi for their administrative support.

This work was supported by Drs. Bob Leheny and Elias Towe at DARPA and Drs. Yoon-Soo Park and Colin Wood at ONR through the Optoelectronics Materials Center, contracts MDA972-94-1-0003, MDA972-98-1-0002, MDA972-00-1-0024, DARPA/ARO contract DAAG55-98-1-0437 and ONR contract N00014-01-1-0010. Supercomputer time at the San Diego Supercomputer Center and the Texas Advanced Computing Center was obtained through a grant from the National Partnership for Advanced Computational Infrastructure.

Much of this work would have been virtually impossible without the support of fellow graduate students from the Harris group. I'd first like to thank the GaInNAs MBE gurus. Wonill Ha and Mark Wistey, fellow GaInNAs crystal growers who worked on the project at the same time; I can not thank you enough for all of your help, extremely valuable insight, and the countless hours working together on systems 4 and 5. I wish you both the best of luck and happiness in the future. To the previous MBE growers on the project, Chris Coldren and Sylvia Spruytte, I'd like to express my utmost gratitude for your hard work and training. I'd also like to thank the next generation of GaInNAs MBE grower Seth Bank, Homan Yuen, Kerstin Volz, and Thimor Gugov. Other people who were extremely instrumental in this thesis work include Glenn Solomon, for all his advice and support in this research, Vincenzo Lordi, for his help with the X-ray absorption

measurements and first principles calculations, other MBE growers, including Xian Liu, Chien Chung Lin, Thierry Pinguet, Qiang Tang, Kai Ma, Xiaojun Yu, Junxian Fu, and other members of the Harris group, including Rafael Aldez, Douglas King, Ofer Levi, Evan Thrush, Vijit Sabnis, and many others.

Also particularly important in this research was the outside support of many people. I'd like to recognize the support of Seongsin Kim, Danielle Chamberlin, Grant Girolami, and Jeffery Rosner from Agilent Technologies, Ralph Johnson and Virgil from Honeywell, and Peter Krispin from the Paul-Drude-Institut. Also, former colleagues from the Harris group and others assisted in X-ray absorption measurements at Spring-8 in Japan, including Toshiyuki Takizawa, Kazuyuki Uno, Masako Yamada, Ichiro Tanaka, Tomoya Uruga, and Satoshi Komiya. Similar measurements were also taken at Lawrence Berkeley National Labs with the help of Stephan Friedrich.

Finally, most important and instrumental in getting me to this point is the support and love from my family and friends. I'd like to thank my mother, father, and sister for their love and support.

# Table of Contents

Abstract .....	iv
Acknowledgements .....	vi
List of Tables .....	xi
List of Figures .....	xii
Chapter 1: Introduction.....	1
1.1 Motivation.....	1
1.2 Semiconductor Lasers.....	4
1.2.1 PIN Laser diode basics.....	4
1.2.2 VCSEL advantages .....	7
1.3 Long Wavelength VCSEL Materials .....	8
1.3.1 DBR materials.....	10
1.3.2 Long wavelength active region materials .....	12
1.3.3 GaInNAs based VCSEL.....	13
1.4 Outline of the Dissertation.....	14
Chapter 2: Molecular Beam Epitaxial Growth of (Ga,In)(N,As,Sb) .....	16
2.1 MBE Introduction.....	16
2.2 MBE Basics.....	18
2.2.1 Source material .....	18
2.2.2 MBE components.....	28
2.2.3 Traditional III-V MBE growth.....	32
2.3 GaNAs Growth.....	33
2.3.1 Nitrogen RF plasma .....	33
2.3.2 Plasma cell operation.....	34
2.3.3 RF plasma optimization.....	37
2.3.4 Nitrogen concentration control.....	40

2.3.5	Nitride-arsenide proprieties.....	42
2.3.6	Instability in a regular solution.....	43
2.3.7	Growth of homogeneous GaNAs.....	48
2.3.8	MBE growth conditions for GaNAs.....	49
2.4	GaInNAs(Sb) Growth.....	52
Chapter 3: (Ga,In)(N,As,Sb) Optical Characterization.....		53
3.1	Nitrogen's Effect on the Bandgap of GaAs.....	53
3.2	Luminescence of GaInNAs.....	54
3.2.1	Introduction to luminescence in solids.....	55
3.2.2	Improving photoluminescence of GaInNAs by annealing.....	58
3.2.3	Optimizing the photoluminescence of GaInNAs.....	62
3.3	Photoluminescence of GaInNAsSb.....	65
3.4	Temperature Dependent Photoluminescence.....	69
3.5	Cathodoluminescence of GaInNAs.....	73
Chapter 4: (Ga,In)(N,As,Sb) Material Characterization.....		79
4.1	Compositional Analysis.....	79
4.1.1	Determining the nitrogen concentration in GaNAs.....	79
4.1.2	Nitrogen calibration using X-ray diffraction.....	82
4.1.3	Nuclear reaction analysis Rutherford backscattering spectroscopy.....	85
4.1.4	Secondary ion mass spectrometry (SIMS).....	88
4.1.5	GaInNAsSb compositional analysis.....	89
4.2	Structural Changes on Anneal.....	93
4.2.1	Atomic rearrangement in GaInNAs.....	93
4.2.2	Deep level defects.....	95
4.2.3	Nitrogen out-diffusion.....	96
4.2.4	Phase segregation in GaInNAs.....	98
4.2.5	Changes in short range order.....	101
4.3	Critical Thickness and Strain Compensation.....	112
Chapter 5: GaInNAs(Sb) Lasers.....		118
5.1	GaInNAs Long Wavelength VCSELs.....	118
5.2	GaInNAsSb High Power Edge Emitting Lasers.....	120

Chapter 6: Conclusions and Future Work .....	124
6.1 Conclusions .....	124
6.2 Future Work .....	125
Chapter 7: References .....	127

# List of Tables

Table I. Material constants for As-based materials at room temperature [65,66]. .....	43
Table II. Material constants for N-based materials. Parameters for zinc blende crystal structures are based on theoretical models at room temperature [65,66]......	43
Table III. Lattice mismatch and interaction parameter for nitride and indium based III-V ternary alloys [69]. .....	47
Table IV. The Varshni fitting parameters for GaAs, GaN, GaInNAs, GaInNAsSb. GaAs [98] and GaN [99] values taken from literature while GaInNAs and GaInNAsSb were both measured. ....	72
Table V. Total nitrogen and interstitial nitrogen content on GaNAs, GaInNAs and GaInNAsSb before and after anneal. Rows in grey, labeled “prev. design”, are data taken from material grown with the initial nine hole front plasma cell aperture.....	88
Table VI. Summary of N K-edge as modeled and measured experimentally. In the calculated vales changes which best match the experimentally determined values are tabulated. ....	110
Table VII. PL energy difference between as- grown and annealed GaInNAs quantum wells with and without GaNAs barriers. ....	116

# List of Figures

Figure 1.1: Bandgap (energy [eV] on left and wavelength [nm] on right) versus lattice constant [ $\text{\AA}$ ] of common III-V materials. Shaded regions mark two alloys based on GaAs and InP which would be lattice matched and have wavelengths between 1300 and 1500 nm.....	3
Figure 1.2: Schematic of an in-plane laser.....	5
Figure 1.3: Schematic of a VCSEL structure.....	7
Figure 1.4: Transmission distance in silica fiber versus transmission speed for different wavelengths of available lasers [21]. .....	9
Figure 1.5: Dispersion and refractive index versus wavelength for commercially available doped silica fiber glass. There is a dispersion zero at 1.3 $\mu\text{m}$ standard silica fiber [22]. .....	9
Figure 1.6: Attenuation versus wavelength of light traveling in silica fiber. There is an attenuation minimum at 1.55 $\mu\text{m}$ for commercially available fiber [22]. .....	10
Figure 2.1: Schematic of source, shutter and substrate in the MBE chamber. ....	17
Figure 2.2: Schematic of the MBE growth chamber. Sources and shutters at the right, loading gate valve at the left, RHEED gun at the bottom, mass spectrometer and RHEED screen at the top, and the sample and beam flux ion gauge at the center of the drawing [35]. .....	18
Figure 2.3: Layout of the source furnaces in the two MBE systems used for GaInNAs based devices.....	19
Figure 2.4: Front of an SVT Associates plasma source with mounted PBN plate and 0.25 mm holes [58]. .....	34
Figure 2.5: Schematic of $\text{N}_2$ gas injection system. ....	35
Figure 2.6: Optical emission spectrum from back of plasma cell at 300 W RF power and 0.25 sccm flow of $\text{N}_2$ .....	38

Figure 2.7: Schematic dependence of emission intensity, ion count, and atomic to molecular ratio with the gas flow rate.....	40
Figure 2.8: Concentration of GaN in GaAs as a function of GaAs growth rate using 300 W RF power and 0.5 sccm flow of N <sub>2</sub> . Concentrations measured by HRXRD. A linear relationship was observed up to 10%. .....	41
Figure 2.9: Free energy versus composition of a system which exhibits a miscibility gap at low temperature ( $T < T_c < T^*$ ) [67].....	44
Figure 2.10: Free energy versus composition for (a) a stable solution in which C has a lower free energy than the mixture of phases A and B with energy M, (b) an unstable solution where the mixture energy M is lower than homogenous solution energy C, and (c) the spinodal point which marks the transition [67]. .....	44
Figure 2.11: A miscibility gap and a spinodal line for a regular solution [67]. .....	46
Figure 2.12: Curves for different concentrations of GaN in GaAs representing the boundary between growth conditions which would produce segregated two-phase material and conditions under which a single phase is stable. The parameters partial pressure of Ga and As versus sample temperature were varied.....	49
Figure 2.13: Photograph of a wafer with a GaNAs thin film grown on the surface with a substrate temperature too high. The ring around the grown wafer was masked by the wafer holder and is representative of the original wafer surface finish. ....	50
Figure 2.14: AFM surface scan of the sample photographed in Figure 2.13.....	51
Figure 3.1: Schematic of the PL/CL process in a direct bandgap material. ....	56
Figure 3.2: PL setup used for room temperature measurements. ....	59
Figure 3.3: Standard PL sample layer structure with AlGaAs cap. ....	60
Figure 3.4: PL of GaInNAs with 30% In and 1.5% N comparing as-grown material with RTA material at different temperatures. ....	61
Figure 3.5: PL intensity and full width half maximum for the PL sample of Figure 3.4. ....	62
Figure 3.6: Background subtracted PL results from 2 GaInNAs/GaNAs samples and 3 GaInNAsSb/GaNAsSb single QW samples. Intended N content remained fixed at 1.2%. ....	66
Figure 3.7: SIMS profile of In, Sb and N before and after the RTA process. The structure consisted of 3 GaInNAsSb QW's between GaNAsSb barriers. The In and Sb	

profiles were not significantly changed by the thermal process while annealing reduced the N concentration in barrier and QW. ....	67
Figure 3.8: Lattice constant versus bandgap for III-V alloys relevant to GaInNAsSb. ....	67
Figure 3.9: An illustration of the conduction and valence and N related energy levels of GaInNAs in k-space. ....	68
Figure 3.10: PL setup for low temperature measurements. ....	70
Figure 3.11: Temperature dependent PL from 15 K to 297 K of a single 70 Å QW 30% In, 1.2% N GaInNAs sample annealed at 760°C for 1 minute. ....	71
Figure 3.12: Schematic of the atomic energy levels versus decreasing lattice parameter (a). This illustration can be used as a guide to understand why the bandgap increases as temperatures decrease. ....	72
Figure 3.13: Normalized PL energy shift versus sample temperature for GaAs, GaInNAs and GaInNAsSb. GaAs data based on Varshni fit of tabulated data, GaInNAs data is from the measurement in Figure 3.11, and GaInNAsSb is a 1.45 μm RT PL sample of 90 Å single QW with 39% In, 1.2% N and an Sb beam flux of $8.38 \times 10^{-8}$ Torr. .	72
Figure 3.14: CL scan of 3 QW samples at a temperature of 4 K: (a) annealed 1.3 μm RT-PL GaInNAs, (b) annealed 1.48 μm RT-PL GaInNAsSb and (c) a 980 nm RT-PL InGaAs. ....	75
Figure 3.15: CL spectrum for the 3 QW GaInNAs sample imaged in Figure 3.14(a). The sample temperature was 4 K. ....	75
Figure 3.16: As-grown 3 QW GaInNAsSb CL spectrum with varied electron beam current from 1.5 nA to 500 nA. ....	77
Figure 3.17: The sample in Figure 3.16 annealed for 1 minute at 760°C intensity-dependent CL spectrum with electron beam currents from 1.5 nA to 500 nA. ....	77
Figure 3.18: A drawing of the conduction and valence energy band structure in real space assuming some non-uniformity in the N concentration. ....	78
Figure 3.19: CL image taken from (a) an as-grown GaInNAs sample and (b) the same sample post-annealed. ....	78
Figure 4.1: Auger electron and X-ray yield per K vacancy as a function of the .....	81
Figure 4.2: Escape depth for electrons of varying electron energy [102]. ....	81

Figure 4.3: (004) rocking curve of GaNAs on GaAs where the N was measured to be 1.27% GaN. The slightly tensile peak to the right of the GaAs peak is a thick film of dilute GaNAs formed when igniting and stabilizing the plasma cell behind a closed shutter.....	84
Figure 4.4: Reciprocal space map of the (224) diffraction of GaNAs on GaAs.....	84
Figure 4.5: Schematic of RBS setup. ....	86
Figure 4.6: NRA-RBS spectrum of a 150 nm GaInNAs film. The arrows point to the nitrogen peak for both channel and random crystal orientations. ....	88
Figure 4.7: XRD (004) rocking curve measurement of three 8 nm QW GaInNAsSb with 20 nm GaNAsSb barrier superlattice. Dynamical simulation shown below measured curve.....	91
Figure 4.8: Nitrogen and antimony SIMS profiles of a three QW GaInNAsSb sample with GaNAsSb barriers. The flux of N and Sb remained constant during growth. ....	92
Figure 4.9: Cross section TEM of six GaNAs QW with 10% N [61]. ....	94
Figure 4.10: XRD rocking curve of phase segregated InGaN grown on GaN [105].....	95
Figure 4.11: SIMS profile of the N signal from 2 GaInNAs QW in GaAs before and after anneal [61].....	97
Figure 4.12: As-grown and annealed (004) XRD rocking curve of a GaNAs 150 nm thin film. ....	97
Figure 4.13: SIMS profile of 3 GaInNAs QW's grown between GaNAs barriers. ....	98
Figure 4.14: XRD (004) rocking curves of the same GaNAs thin film on GaAs grown at different substrate growth temperatures.....	99
Figure 4.15: Cross section TEM image of poor quality GaInNAs, showing signs of quantum dot like behavior [114]. ....	100
Figure 4.16: Cross section atomic resolution TEM image of a 9 QW sample of GaInNAs with GaNAs barriers. The blown up image is from the top QW which shows little sign of phase decomposition. ....	101
Figure 4.17: (a) Schematic of an XAFS experiment, and (b) a drawing showing EXAFS interference of an emitted photoelectron based on nearest neighbor configuration and the subsequent fluorescent photon. ....	104

Figure 4.18: The BL01B1 beamline at Spring-8 used for measuring the XAFS signal for the In K-edge [120]. .....	104
Figure 4.19: The focusing optics and monochromator for the incident X-rays [120]. ...	105
Figure 4.20: Brilliance versus X-ray energy for the BL01B1 beam line. The In K-edge is at 27.92 keV [120]. .....	105
Figure 4.21: The fluorescence intensity from excited photoelectrons versus the incident X-ray beam energy for an InAs substrate and 10 nm GaInNAs films before and after anneal. ....	107
Figure 4.22: The radial distribution function for the In atom in the GaInNAs alloy before and after anneal. ....	107
Figure 4.23: Normalized N XAFS spectrum for as grown and annealed 3000 Å GaInNAs samples with 15% In, and a GaNAs 1500 Å film, all with 1.5% N. ....	109
Figure 4.24: Nitrogen K-edge energy shift in GaInNAs with increasing In-N bonds. The energy shift is plotted relative to GaNAs [123]. ....	109
Figure 4.25: The statistical probability for the number of In-N bonds for different In compositions with 3% N in a completely random alloy [123]. ....	111
Figure 4.26: Bandgap shift by increasing the number of In-N bonds in the crystal using a local density approximation (LDA) simulation [123]. ....	111
Figure 4.27: Lattice constant and total crystal energy in GaInNAs as a function of the number of In-N bonds [123]. ....	112
Figure 4.28: (004) XRD pattern from three QW GaInNAs/GaNAs and GaInNAsSb/GaNAsSb structures. ....	113
Figure 4.29: PL from as-grown and anneal GaInNAs, with and without GaNAs barriers. The composition of the quantum wells where the same for both samples [61]......	116
Figure 4.30: PL spectra for 3, 6, and 9 GaInNAs QWs with tensile strain compensated GaNAs barriers. ....	117
Figure 5.1: (a) Light output power and voltage vs. injection current (L-I-V) characteristic under room temperature continuous wave operation for $3.6 \times 3.6 \mu\text{m}^2$ and $5 \times 5 \mu\text{m}^2$ VCSELs. (b) Emission spectra at 1.3 mA ( $\sim I_{\text{th}}$ ) and 3.5 mA ( $\sim 2.6 I_{\text{th}}$ ) for a $5 \times 5 \mu\text{m}^2$ GaInNAs oxide confined VCSEL. ....	120

Figure 5.2: (a) SEM image of 3 ridge waveguide lasers, of 5, 10 and 20 $\mu\text{m}$ mesa structures. (b) Close up of the 5 $\mu\text{m}$ laser. ....	121
Figure 5.3: (a) Light output power vs. injection current (L-I) characteristic for 5 $\mu\text{m}$ wide ridge waveguide edge emitting GaInNAsSb laser under room temperature pulsed operation. (b) Emission spectra at 200 mA ( $\sim 1.2 I_{\text{th}}$ ) under pulsed operation at room temperature. ....	122
Figure 5.4: (a) L-I for a 3 QW GaInNAsSb ridge waveguide edge emitting laser. (b) Emission spectra at $1.2 I_{\text{th}}$ for same device. ....	123



# Chapter 1: Introduction

Currently, the only viable way to manufacture low cost vertical cavity surface emitting lasers (VCSEL) has been GaAs based epitaxy, utilizing the AlGaAs/GaAs mirror system. The major drawback has been the limited range of wavelengths available in the GaAs system, particularly the inability to reach the long-wavelength telecommunication band. GaInNAsSb on GaAs, a new alloy developed in this thesis research, may quickly become the active region material that allows GaAs-based devices to operate in this important wavelength band. While the material system has its own challenges, through careful material analysis and optimization, high quality material can be grown which outperforms the alternatives.

## 1.1 Motivation

Devices with emission wavelengths between 1.3 and 1.6  $\mu\text{m}$  are of primary importance in optical local (LAN) and metro (MAN) area networks, and long haul communications due to the dispersion zero at 1.3  $\mu\text{m}$  and minimum loss at 1.55  $\mu\text{m}$  in optical silica fiber. The requirements for optical communication lasers in these applications are a broad, stable operating temperature range (up to 90°C), emission spectra between 1.3-1.6  $\mu\text{m}$ , and moderate power (>10 mW). There is also significant interest in higher power pump lasers for Raman amplifiers to greatly increase the available bandwidth in existing fiber systems by enabling signal amplification over the entire transparency range for silica fiber. Current fiber amplifiers, known as erbium doped fiber amplifiers (EDFAs), can only amplify light between 1.5-1.6  $\mu\text{m}$ . Raman amplifiers can boost signal over a much larger range of wavelengths simply by propagating a high-power pump along with the signal down the fiber, providing gain at a frequency of about 13 THz (100 nm) downshifted from the pump radiation. The requirement for a Raman amplifier therefore is simply a high-power laser with

operating wavelengths between 1.2-1.5  $\mu\text{m}$ . Current commercial solutions for light sources in this wavelength range involve InP-based lasers with active regions such as GaInAsP. This material can quite readily have direct bandgaps between 1.2-1.6  $\mu\text{m}$  and can be lattice-matched to the InP substrate. However, there are several serious fundamental shortcomings that hinder its ability to cover this wavelength range [1], and make low cost lasers, particularly VCSELs, extremely difficult. Current commercially available telecommunications long wavelength InP-based lasers cost several thousand dollars.

An alternative solution to InP epitaxy would be to use materials grown on GaAs. However, alloys which are nearly lattice-matched to GaAs, historically have optical emission at wavelengths less than 1.1  $\mu\text{m}$ . Adding In to GaAs reduces its bandgap, but also increases the lattice parameter, and for material beyond 1.1  $\mu\text{m}$  deep level defects created by dislocations inhibit efficient radiative recombination. Recently, it has been found that GaInNAs grown on GaAs substrates optically emits at wavelengths longer than previously possible for epitaxial material. Research has shown that GaInNAs coherently lattice-matched to GaAs [2-4] can have a bandgap energy in the wavelength range of 1.3-1.55  $\mu\text{m}$  and have properties which would fulfill the requirements of optical communication systems [5]. Adding a small amount of N to GaAs alloys preserves the direct bandgap, has a type-I band offset, and can decrease the bandgap while shrinking the lattice constant. Adding N to InGaAs pushes emission to longer wavelengths and offsets the In lattice mismatch, making higher In concentrations possible. Figure 1.1 shows the available III-V alloys which can be grown on the GaAs and InP binaries with commercially relevant wavelengths marked. While GaN has a bandgap of about 3.4 eV, increasing the N in dilute nitride GaNAs bows the bandgap to much lower energies, theoretically to 0 eV. The bandgap reduction for a given lattice mismatch is much sharper than by adding In to GaAs.

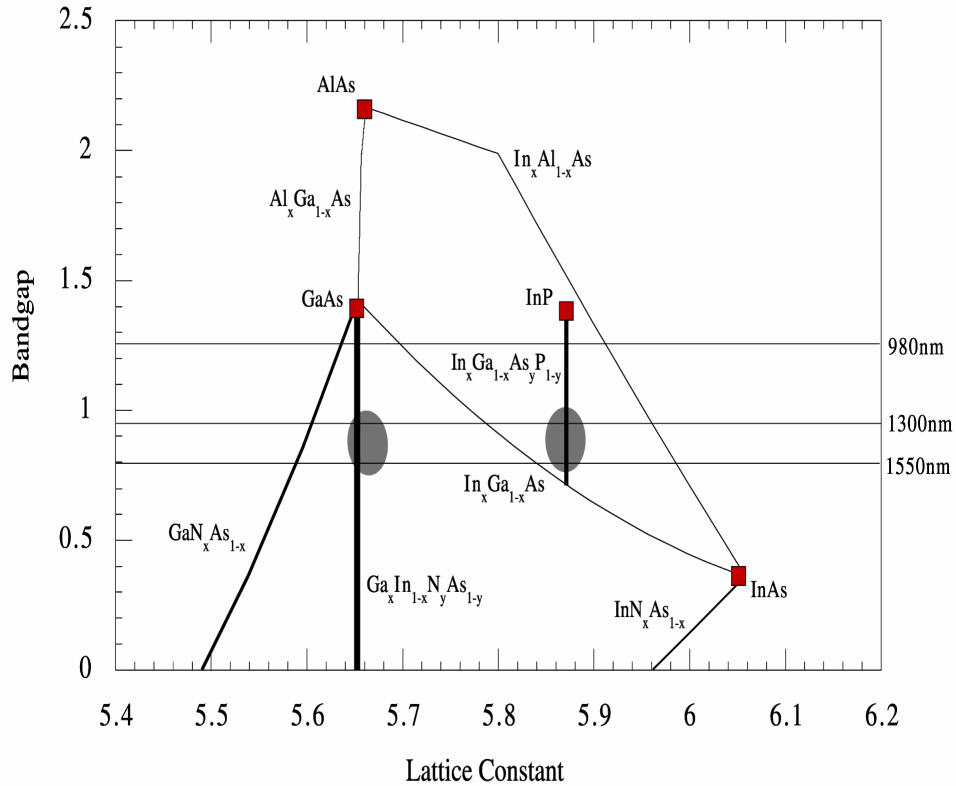


**Figure 1.1: Bandgap (energy [eV] on left and wavelength [nm] on right) versus lattice constant [ $\text{\AA}$ ] of common III-V materials. Shaded regions mark two alloys based on GaAs and InP which would be lattice matched and have wavelengths between 1300 and 1500 nm.**

At first the thought of using N to redshift the bandgap of GaAs would not seem logical considering the N solubility in GaAs is extremely small and the GaN bandgap is larger, not smaller, than GaAs. The large electronegativity of N and the mixing of cubic GaAs and hexagonal GaN crystal systems create the significant band bending and low solid solubility between the two systems. In fact, thermodynamic calculations predict less than 0.1% GaN solubility in GaAs which would greatly limit its utility. Many growth challenges exist in trying to make a homogenous GaNAs alloy due to these divergent properties of GaAs and GaN. However, by using metastable growth conditions, the solid solubility of N in GaAs can be extended to concentrations as high as about 5%. The bandgap is ultimately limited by the amount of In which can be added while remaining below the critical thickness for dislocation formation, and by the concentration of N before phase segregation is kinetically favored.

High PL efficiency GaInNAs material has been grown that extends out to 1.3  $\mu\text{m}$ , but beyond that wavelength, material quality commonly degrades rather seriously. Lasers utilizing these longer-wavelength active materials exhibit extremely high threshold current densities and low output power [6]. In this thesis research, a new technique was investigated to expand the feasible emission wavelengths for this material system. Sb present during GaInNAs growth has been thought to act only as a surfactant to improve quantum well (QW) planarity and PL [7,8]. With the addition of Sb, we have observed a sharp increase in radiative recombination with high In samples past 1.3  $\mu\text{m}$  and found it not only acts as a surfactant, but also incorporates, further reducing the bandgap. With this new GaInNAsSb alloy, operation can be extended to even longer wavelengths than possible with the GaInNAs quaternary.

## 1.2 Semiconductor Lasers

### 1.2.1 PIN Laser diode basics

The concept of optical communications using lasers has been around ever since the first laser was invented in 1960. In 1960 the first laser, using synthetic ruby, was reported by Theodore Maiman and introduced with the statement, "Usable communications channels in the electromagnetic spectrum may be extended by development of an experimental optical-frequency amplifier" [9,10]. It wasn't until the 1970's, with the introduction of low loss, step index multimode fiber, that the first demonstration of fiber optic communications was achieved using 850 nm AlGaAs lasers.

In general, a laser is made up of three components: a pump, gain medium, and resonant cavity. In semiconductor lasers, the pump is a source of both electrons and holes. This generation of carriers can occur either optically, such as exciting carriers by absorbing light with energies greater than the bandgap, or electrically, such as in a forward biased  $p$ - $n$  junction. In a  $p$ - $n$  junction, electrons are injected from the  $n$ -type doped region and holes injected from the  $p$ -type doped region. In a double heterostructure  $p$ - $i$ - $n$  diode, an intrinsic material of smaller bandgap acts as the gain medium and is placed between  $n$  and  $p$ -type doped semiconductors. Electrons and

holes collect in the intrinsic region and recombine with excess energy given off as either lattice vibrations or light. All  $p-n$  junctions give off light on passage of a forward bias current. Indirect gap semiconductors such as Si and Ge are very inefficient at light emission and give off most of this energy in the form of heat, while direct gap semiconductors, such as GaAs, InP and their alloys, are highly efficient at emitting photons.

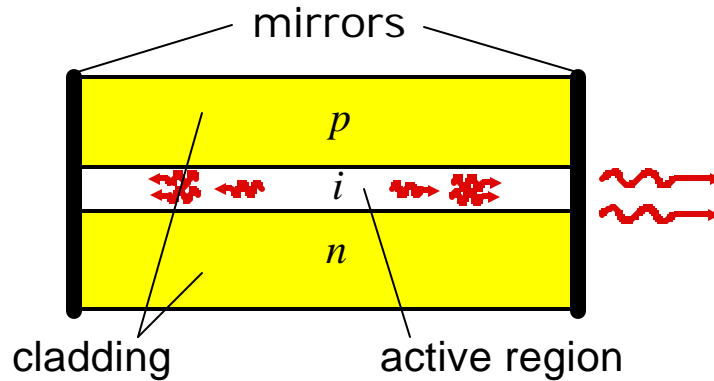


**Figure 1.2: Schematic of an in-plane laser.**

A resonant cavity can be created by making a waveguide and mirror structure. In an in-plane laser, the light which is created in the intrinsic region is guided due to the higher index of refraction in the active region than in the large bandgap cladding layers. Two mirrors placed at either end of the waveguide region, known as a Fabry-Perot cavity, allow the light to resonate, making many trips through the gain region. In an in-plane laser the mirrors are simply cleaved facets perpendicular to the active region. An in-plane  $p-i-n$  heterojunction laser is illustrated in Figure 1.2. Initially the light is spontaneously emitted from the active region. But under high current densities, the number of electrons in an excited state, or the conduction band, is greater than the number of electrons in the ground state, or the valence band, a condition known as population inversion. Above this inversion limit, light absorption is no longer the dominant mechanism and stimulated emission takes place. Light travels along the active region, being amplified the entire device distance which, for the in-plane laser case, is typically hundreds of microns.

In a VCSEL structure, shown in Figure 1.3, the mirrors are parallel to the active region, and light travels perpendicular through the thin active region. In this configuration, the light travels a very small distance through the gain medium on each pass so the mirrors must be highly reflective and active region must be highly efficient. Using a best case gain of  $1000 \text{ cm}^{-1}$  as an example, the reflectivity of the mirrors has to be 99.95% to insure gain. Fresnel reflection at the semiconductor-air interface is no longer sufficient as in the in-plane case and even metallic mirrors are only around 98% reflective and thus not sufficient. Dielectric materials and semiconductors have a very low absorption coefficient for photons with energies below the bandgap energy of the material. If two dielectric materials, with a differing refractive index are placed together to form a junction, light will be reflected at the discontinuity. The amount of light reflected off one such boundary is small. However, if layers of alternating semiconductor or dielectric are stacked periodically, each layer with an optical thickness  $\lambda/4n$ , the reflections from each of the boundaries will add in phase to produce a large reflection coefficient. The number of layers required to produce a highly reflective mirror at a particular wavelength is determined by the difference in the refractive index of the contrasting materials. These structures are known as distributed Bragg reflecting (DBR) mirrors. In semiconductor DBR layers, growth must take place epitaxially to reduce losses due to misfit dislocations, and must be transparent to the lasing wavelength of the active region. One example of a commercially available VCSEL design is an InGaAs quantum well laser using nearly lattice-matched GaAs/AlAs DBRs.

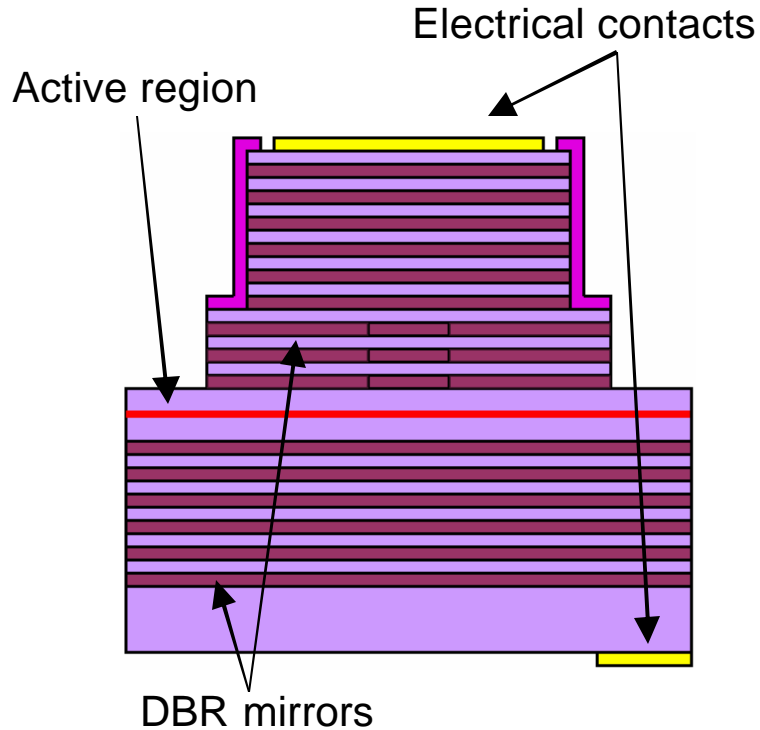


**Figure 1.3: Schematic of a VCSEL structure.**

### 1.2.2 VCSEL advantages

The first VCSEL structure was reported in 1965 by Melngailis [11,12] consisting of an  $n^+-p-p^+$  junction of InSb. When cooled to 10 K and subjected to a magnetic field to confine the carriers, the device emitted coherent radiation at a wavelength of around 5.2  $\mu\text{m}$ . Later, other groups reported vertical lasers by using grating surface emission [13,14]. Near IR vertical emission at around 1.5  $\mu\text{m}$  was achieved by Iga in 1979 [15] at the Tokyo Institute of Technology. These early VCSEL devices utilized metallic mirrors which resulted in high threshold current densities (44  $\text{kAcm}^{-2}$ ) while cooled with liquid nitrogen. Epitaxial mirrors for the GaAs/AlGaAs VCSEL were first grown in 1983 [16], with the first pulsed room temperature VCSEL produced in 1984 [17]. The reduction in the threshold current density came about with the reduction of the volume of the cavity, and currently GaAs/AlGaAs VCSELs with oxide current confinement have threshold currents as low as 9  $\mu\text{A}$  [18].

For the past 25 years VCSELs have been studied as a replacement for in-plane lasers due to their higher performance and reduced cost potential. Its design allows the lasers to be manufactured and tested on a single wafer using traditional semiconductor processing and testing technology. The VCSELs uniform, single mode beam profile and vertical emission simplifies coupling into optical fiber. This makes wafer-level *in situ* testing before packaging possible and greatly reduces manufacturing costs [19]. Large two dimensional arrays of devices can now be created; making new types of optical interconnects possible. However, with these advantages come a number of problems particularly in the fabrication and growth due to complex layer structures and operation at high powers. As mentioned above, the two most critical factors in creating high quality VCSEL structures is high reflectivity DBR mirrors and a high radiative efficiency gain medium. For high reflectivity, the highest performance semiconductor DBR mirrors available today are the lattice matched GaAs/AlAs mirror system based on GaAs. A high-gain active region grown on GaAs with bandgaps at the telecommunication wavelengths is the subject of this thesis and will be discussed in much greater detail.

### **1.3 Long Wavelength VCSEL Materials**

The vast majority of VCSELs produced today and by far the easiest to manufacture are the 850 nm GaAs/AlGaAs and 980 nm InGaAs/GaAs quantum well lasers with AlGaAs DBRs. Unfortunately, transmission rates are severely limited at these wavelengths in fiber optic systems due to high dispersion and attenuation as shown in Figure 1.4 for the 850 nm case [20][21]. At slow bit rates, less than 100 Mb/s, signals can travel for several kilometers, but at faster bit rates, 1 Gb/s and beyond, transmission is limited to tens of meters. These VCSELs are really only relevant for low-speed or short distance, low-cost applications. However, at longer wavelengths, attenuation and dispersion are much less a problem and at 1310 nm there is a dispersion zero, see Figure 1.6, and at 1550 nm there is an attenuation minimum, see Figure 1.6, in silica fiber. From Figure 1.4, it can be seen that by using these longer wavelengths, transmission distance and bit rate can be much greater for the same fiber

systems. Therefore, it is clear that longer wavelength VCSELs are needed to make better use of existing fiber optics telecommunication systems by replacing current 850/980 nm laser technology.

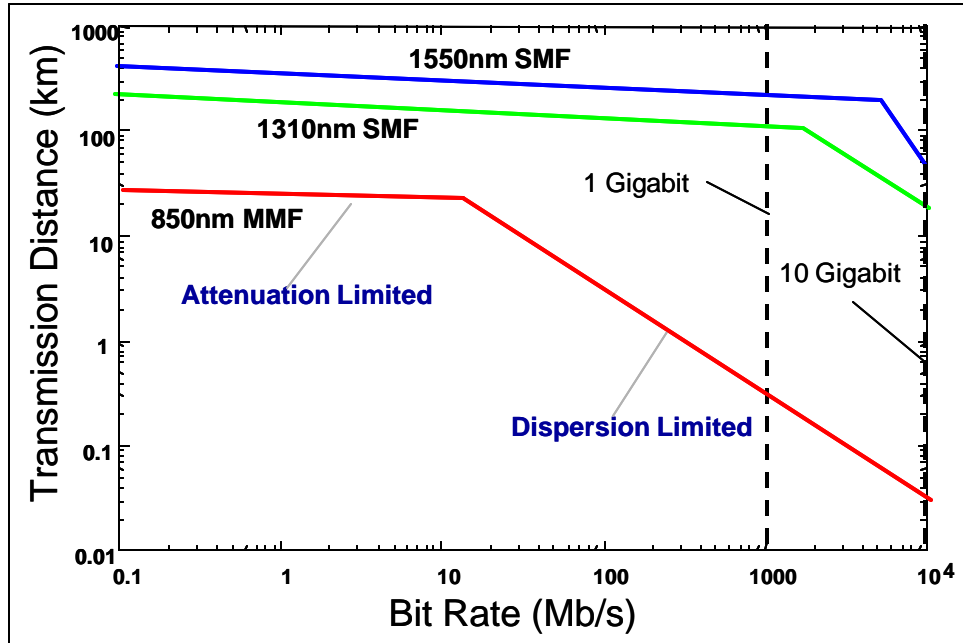


Figure 1.4: Transmission distance in silica fiber versus transmission speed for different wavelengths of available lasers [21].

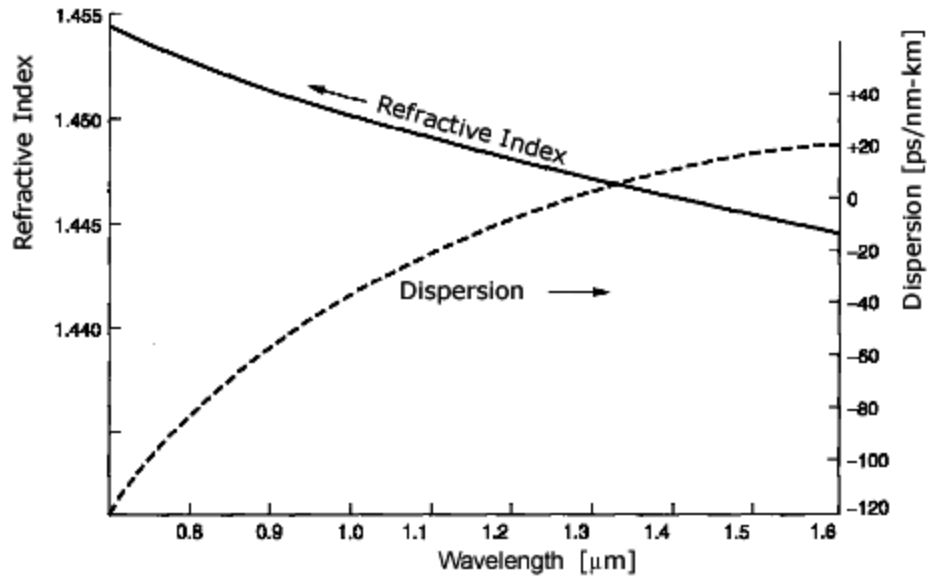


Figure 1.5: Dispersion and refractive index versus wavelength for commercially available doped silica fiber glass. There is a dispersion zero at 1.3  $\mu\text{m}$  standard silica fiber [22].

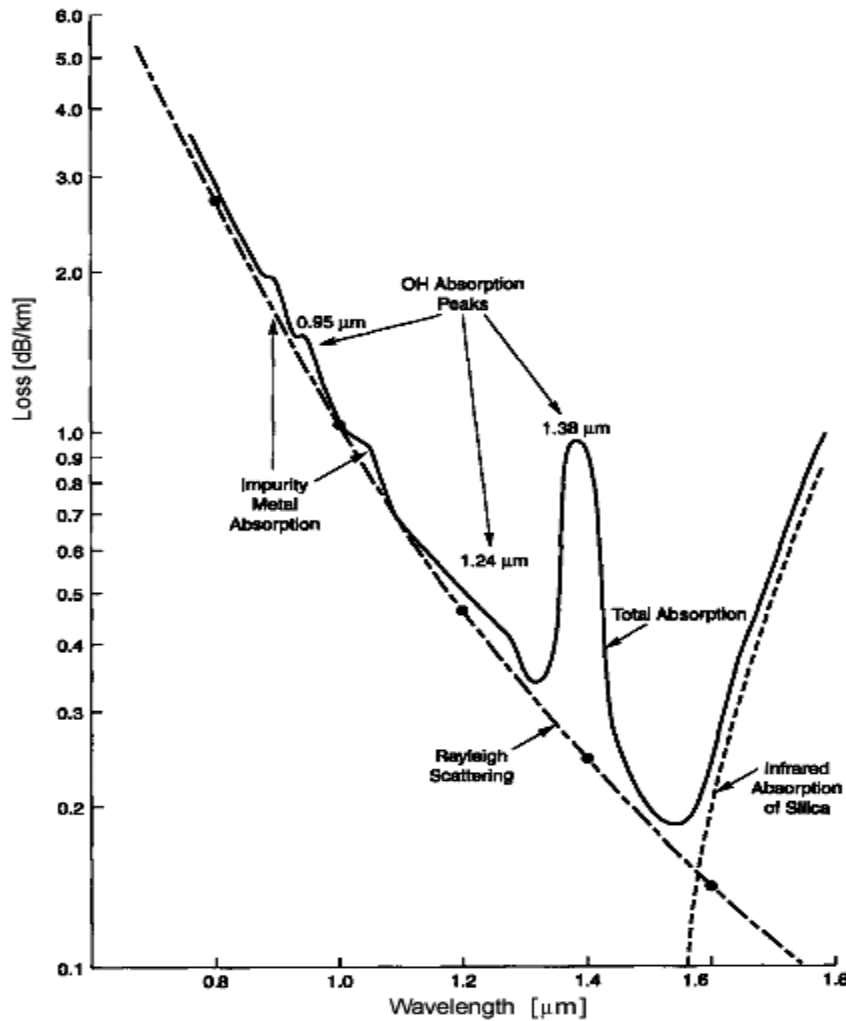


Figure 1.6: Attenuation versus wavelength of light traveling in silica fiber. There is an attenuation minimum at 1.55 mm for commercially available fiber [22].

### 1.3.1 DBR materials

The current approach for 1.3  $\mu\text{m}$  long wavelength lasers is  $\text{Ga}_{0.2}\text{In}_{0.8}\text{As}_{0.6}\text{P}_{0.4}$  quantum wells on InP substrates. This technology has worked well for in-plane lasers but there has been a great deal of difficulty in adopting this system to VCSEL structures. The refractive index contrast for materials based on InP, compared to GaAs, makes it very difficult to obtain mirrors of sufficient reflectivity. Figure 1.1 shows that in GaAs-based epitaxy there is the GaAs and AlAs binary and alloys with a large bandgap difference, hence, refractive index contrast, that is transparent to the active

region emission. However, for InAs, there are only ternary or quaternary alloys with a small bandgap offset that would be transparent to near-IR emission. Both the GaInAsP/InP and GaAlInAs/AlInAs mirror systems have been studied, but require greater than 50 mirror pairs due to the small index contrast at long wavelengths, while only 20-30 pairs are necessary for the GaAs/AlAs system. An alternative mirror design is AlGaAsSb lattice-matched to InP which has an improved index contrast. However, these layers are fairly resistive and have poor thermal conductivity causing heat generation in the active region. Secondly, this system does not exhibit ideal solid solubility, and during growth it is difficult to control the As and Sb ratio across the entire wafer.

Alternative approaches to the epitaxial DBR on InP are wafer fusion [23], metamorphic growth [24], or dielectric mirrors [25]. Wafer fusion uses conventional GaAs-based DBRs with a conventional InP-based active region using direct wafer bonding. Fabrication cost and complexity are dramatically increased and bonding can only take place on small sample sizes. In metamorphic growth, relaxed GaAs-based mirrors are grown on InP, however, it is extremely challenging to prevent dislocations from propagating into the upper mirrors. Furthermore, only the upper mirror is grown with this technique leaving the lower mirror with poor reflectivity. In both of these approaches, the interface is a source of defects for non-radiative recombination, carrier scattering, and optical absorption. In the last approach, dielectric mirrors are deposited after the epitaxial growth. Materials such as ZnSe/MgF, SiO<sub>2</sub>/TiO<sub>2</sub>, Si/SiO<sub>2</sub>, and Si/Al<sub>2</sub>O<sub>3</sub> have been used, but none are electrically conductive and they all typically have low thermal conductivity. This makes current injection into the active region and removing heat difficult. In addition, if the bottom mirror is made this way, the substrate must be removed.

AlGaAs DBRs grown on GaAs do not suffer from these shortcomings. GaAs and AlAs are nearly lattice matched and have a large difference in index of refraction. Therefore in order to get greater than 99.9% reflectivity, fewer pairs are needed. Furthermore, binary instead of ternary or quaternary alloys can be used, increasing the thermal conductivity of the mirror structure. As soon as more than a few percent of a third component is added to a binary compound, thermal conductivity can decrease

quickly by a factor greater than four. As an additional benefit, AlAs has a very well controlled oxidation behavior, enabling an  $\text{Al}_x\text{O}_y$  current and light confinement layer in the VCSEL design which helps lower laser threshold currents.

### 1.3.2 Long wavelength active region materials

Even for in-plane lasers, InP-based lasers tend to be much more costly than their short wavelength GaAs-based competition. The GaInAsP active region has a strong temperature dependence for laser properties, such as threshold current. Much of the temperature dependence arises from the small conduction band offset between GaInAsP and InP, where  $\Delta E_c = 0.4\Delta E_g$  [26,27]. With little confinement, the lighter electrons can escape from the quantum well given enough thermal energy. As the temperature increases, more electrons leak out of the well and the Auger recombination rate increases, reducing the available gain. With decreased gain, the current requirements increase heating the device further. As a result, InP-based lasers require external cooling in high performance applications, drastically increasing their cost and size, and limiting integration possibilities. Especially in VCSELs, the thermal properties of the gain medium are crucial due to high heat dissipation requirements and typically high DBR thermal resistance. In InP-based systems compared to GaAs-based systems, the available mirrors have lower thermal conductivity because of ternary and quaternary DBR alloys, more mirrors are necessary due to lower index contrast, and the active region is more thermally sensitive. These factors add up making VCSEL fabrication on InP extremely challenging.

In order to improve thermal performance, an alternative InP-based active region, GaAlInAs, has been used. GaAlInAs has a larger conduction band offset; however, growth is difficult due to non-ideal solid solubility, surface segregation during growth, and ordering. Also, the same inferior InP-based DBR mirrors would be used in a structure designed around this active region.

With all the challenges involved in making DBRs on InP, a new active region on GaAs with bandgaps at the telecommunications wavelengths has been widely investigated. GaAsSb grown on GaAs has been proposed for long wavelength VCSELs and 1.3  $\mu\text{m}$  continuous wave (CW) in-plane laser operation has been demonstrated

[28]. However, GaAsSb has a type-II conduction band offset with GaAs at high Sb concentrations and the conduction band offset has been predicted to be too small to strongly confine electrons in quantum wells at 1.3  $\mu\text{m}$ . This results in poor thermal performance and laser threshold currents for devices with a GaAsSb active region. InGaAs grown epitaxially on GaAs can reach about 1  $\mu\text{m}$  before strain induced deep level defects dominate in electron-hole recombination. However, InGaAs quantum dots (QD) have recently been studied for 1.3  $\mu\text{m}$  room temperature VCSELs [29]. Highly strained InGaAs layers give rise to a very thin wetting layer and strain induced islands or dots. As the QDs are nucleated and grown their size can not be precisely controlled giving rise to island fluctuations and a broadening of the emission spectra. Furthermore, carriers at room temperature tend to leak out from the dots and fill states in the wetting layer, further increasing spectral emission variations and decreasing device performance. While very impressive results have been demonstrated for edge emitting lasers, this approach has not been widely adopted commercially due to uniformity issues inherent in the uncontrolled QD growth and limited gain for VCSELs.

### 1.3.3 GaInNAs based VCSEL

In order to make low-cost high performance VCSELs at the telecommunication wavelengths, we believe several requirements must be satisfied. The active region needs to be both grown epitaxially to GaAs in order to take advantage of AlGaAs DBRs, and be thermally stable at standard operating temperatures without active cooling. Adding N to InGaAs reduces the alloy lattice parameter, increasing the amount of In possible, and allowing thicker layers to be grown before QD growth mechanisms dominate or dislocations relax film stress. A great deal of experimental and theoretical observations suggest the valence band offset between dilute nitride GaNAs and GaAs is very small and the majority of the bandgap offset comes from conduction band lowering [5,30,31]. Compared with InGaAs, the GaInNAs/GaAs junction would have an increased conduction band offset of around  $\Delta E_c = 0.7\Delta E_g$ , strongly confining the light  $\Gamma$ -valley electrons, while the small valence band offset will not significantly increase hole evaporation from the active region. Also,

GaInNAs/GaAs has been expected to follow a type-I offset, in which conduction and valence offsets are in a direction to confine both electrons and holes.

In many applications, the ability of a laser to have stable performance at fluctuating elevated temperatures without active cooling is of great interest, particularly for low cost applications. This is especially important in the case of high-power laser diodes where the amount of power generated causes the device temperature to rise significantly. It is also important for directly modulated laser applications where the temperature of the device varies with unpredictable conditions, such as ambient temperatures or network traffic. The characteristic temperature,  $T_0$ , of the laser diode is a measure of the temperature sensitivity of the device. Higher values of  $T_0$  imply that the threshold current density and the external differential quantum efficiency of the device increase less rapidly with increasing temperatures. Conventional AlGaAs lasers usually have  $T_0$  values above 120 degrees, while  $T_0$  values for InGaAsP active regions are only 60-80 K. GaInNAs quantum wells with GaAs barriers have been estimated to have  $T_0$  as high as 180 K [5] and values between 100 and 215 K have been experimentally observed [32].

Finally, unlike InGaAs quantum dots, quantum wells of GaInNAs on GaAs are expected to be homogeneous planar layers with sharp interfaces. Film strains are at levels below which quantum dot formation or relaxation normally takes place. However, unlike other III-V alloys, N is not fully soluble in GaAs. With enough thermodynamic driving force, phase separation between GaAs and GaN occurs and causes concentration fluctuations and highly non-uniform layers. Therefore, growth of GaNAs must proceed under metastable growth conditions, kinetically limiting phase segregation of GaN. By using low substrate temperatures during growth and a highly reactive atomic source of N, high crystalline quality, homogeneous GaInNAs can be grown.

## 1.4 Outline of the Dissertation

In this section an outline of this thesis will be presented.

Chapter 1 has provides a motivation for this work, including current competing alternatives to using a GaInNAs active region on a GaAs substrate for long wavelength lasers and several advantages in using GaInNAs active regions.

Chapter 2 covers MBE growth of both traditional III-V materials, such as InGaAs and AlGaAs, and the growth of the more complicated GaInNAs and GaInNAsSb alloy systems. Full details of the experiences and difficulties encountered while growing this new material are discussed. Techniques used to optimize the plasma and growth conditions in order to get the highest quality material are also covered. Material challenges with this alloy system, such as phase decomposition and metastable growth conditions are also presented.

Chapter 3 presents optical characterization techniques used to study the dilute nitride-arsenide alloys. First, the unique mechanism by which N reduces the bandgap of GaAs by band anticrossing is discussed. Optical measurements which detect luminescence in materials are shown in order to help better understand the effects of thermal annealing on luminescence, the dependence of the bandgap on temperature, and the compositional uniformity of this new material.

Chapter 4 covers material characterization measurements which were taken to understand incorporation of the alloy components. Also, analysis was done to understand structural changes that can affect luminescent properties after thermal annealing. The structural changes were used to explain intensity improvement and bandgap changes after high temperature anneal.

Chapter 5 presents results of several lasers grown and fabricated with the GaInNAs and GaInNAsSb active regions, and their performance.

Finally, chapter 6 concludes the thesis and discusses suggestions for future work.

# Chapter 2: Molecular Beam Epitaxial Growth of (Ga,In)(N,As,Sb)

In this chapter, the growth of GaInNAsSb and its alloys by molecular beam epitaxy (MBE) is discussed. Current technologies and techniques of MBE growth are covered in some detail, including the components chosen for the highest quality and most flexible growth. Included are techniques used to optimize GaNAs growth using conditions such as RF plasma parameters and growth temperature. Issues concerning solubility of GaN in GaAs and ways to grow GaNAs to prevent phase decomposition are covered. Since the growth of GaNAs is different than other traditional III-V semiconductors, the series of growths we used to calibrate and optimize the nitride-arsenide alloy will also be presented.

## 2.1 MBE Introduction

MBE was developed in the early 1970's as a technology to grow high-purity epitaxial layers of compound semiconductors [33,34]. Since then, it has evolved into a popular technique for growing III-V and II-VI compound semiconductors, as well as several other materials, such as oxides, Si and Ge. MBE can produce high-quality single crystal layers with very abrupt interfaces, monolayer control of thickness, precise doping and compositional accuracy. Because of the high degree of control and flexibility using MBE, it is a valuable tool in the development of sophisticated electronic, magnetic and photonic devices.

The essential elements of any MBE technique consist of a flux of molecules aimed at a single crystal substrate while under ultra high vacuum (UHV) background pressure. In solid source MBE (SSMBE), component molecular fluxes come in the form of evaporated or sublimated high purity elemental metal source materials. Under UHV pressure (around  $10^{-9}$ - $10^{-11}$  Torr) the mean free path for evaporated atoms is on

the order of tens of meters, much greater than any physical dimension of the vacuum chamber. Thus, a flux of evaporated material is referred to as a “beam” whereby negligible scattering occurs between source material and substrate. Growth rates are controlled within a few Å/s by precisely controlling the temperature of the effusion cell and therefore partial vapor pressure of each source material. A shutter or beam stop is placed in front of each source to modulate the presence of each component at the substrate as the growth proceeds. A drawing of the source material, shutter, molecular beam and substrate is shown in Figure 2.1. Under molecular flow vacuum conditions, shutters need only block the beam “line-of-sight” in order to completely shield depositing species. With monolayer per second growth rates, sub-second shuttering speed, and collision-free deposition, layers can be controlled with atomically abrupt transitions.

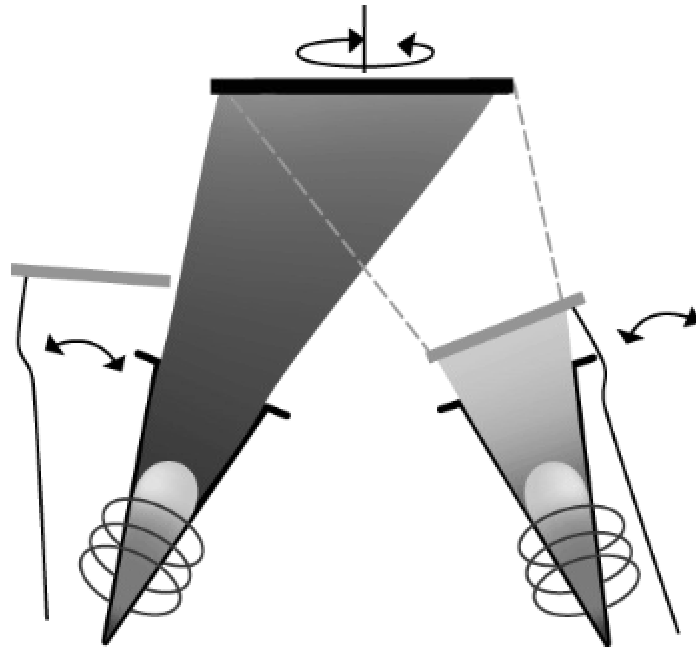


**Figure 2.1: Schematic of source, shutter and substrate in the MBE chamber.**

A Varian Mod Gen II system was used for the growth of dilute nitride GaInNAsSb in this thesis research. A schematic of the Varian Mod Gen II is shown in Figure 2.2. The system consists of two Mod Gen II growth chambers coupled by a UHV transition tube. An Auger electron spectroscopy (AES) chamber is also

connected to the transition tube in order to monitor surface contamination. Substrates enter the vacuum through a gate-valved load lock chamber where they are initially pumped and baked to remove water and other surface contamination. A magnetically transferred wafer trolley is used to hold and transport of up to 12 wafers under vacuum between the various systems.

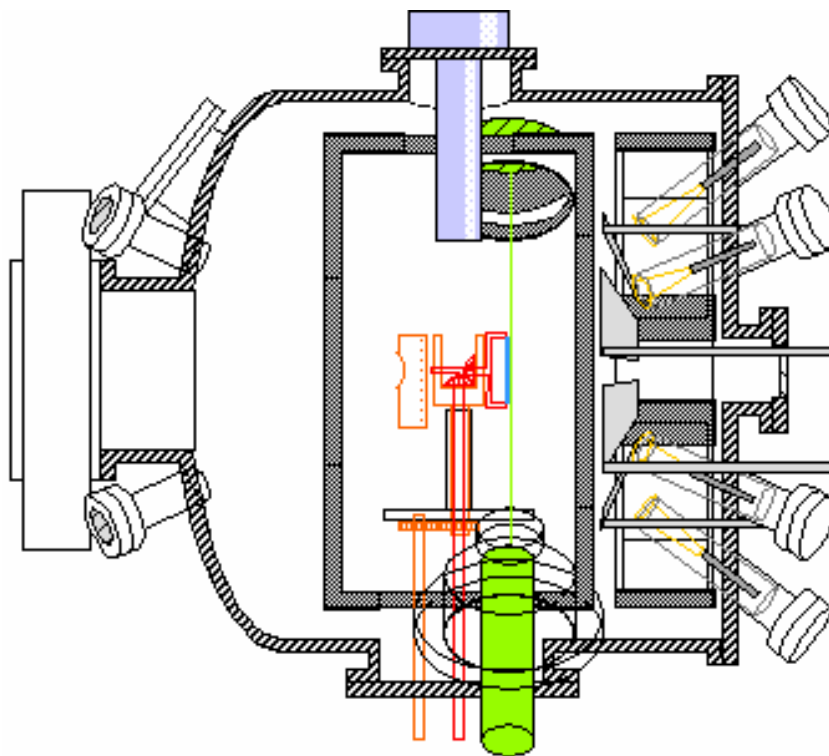


**Figure 2.2: Schematic of the MBE growth chamber. Sources and shutters at the right, loading gate valve at the left, RHEED gun at the bottom, mass spectrometer and RHEED screen at the top, and the sample and beam flux ion gauge at the center of the drawing [35].**

## 2.2 MBE Basics

### 2.2.1 Source material

Each Mod Gen II growth chamber consists of 8 effusion cells. With sources where precise thickness and compositional control is necessary, temperatures are fixed and growth rates are carefully measured before growth begins and not changed throughout the growth run. Therefore, in order to have layers with different alloy compositions in the same sample, multiple cells of the same source material are

necessary, hence limiting the number of unique sources present in an individual chamber. Consequently, multiple machines are coupled together allowing for greater flexibility in the materials available. Figure 2.3 shows the source material configuration for the two MBE chambers used for nitride growth at Stanford. System V is the chamber used to grow (Ga,In)(N,As,Sb), while system IV is primarily used for GaAs/AlAs DBR mirror growth.

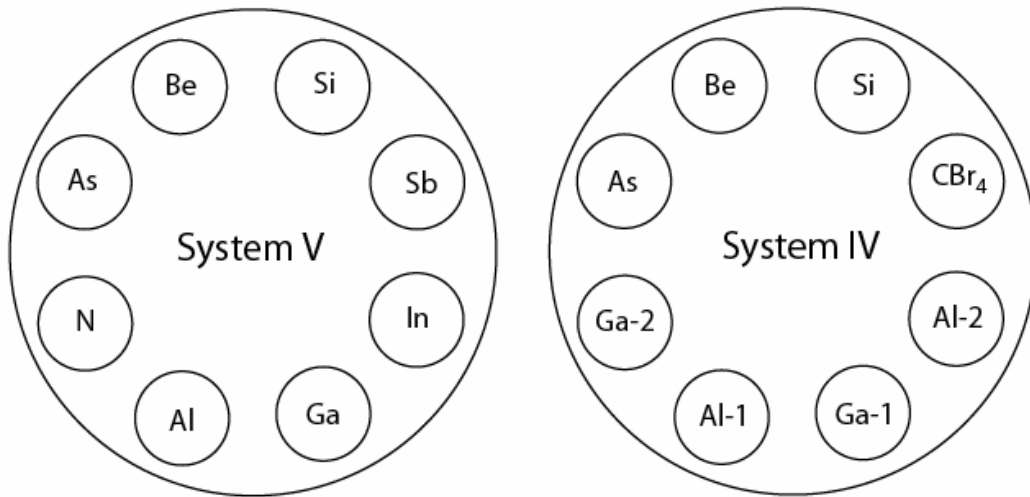


**Figure 2.3: Layout of the source furnaces in the two MBE systems used for GaInNAs based devices.**

#### 2.2.1.1 Group-V sources: As

During most traditional III-V growth, the group-V components (As, P, or Sb), must be present in overpressure since they desorb from the hot substrate and only stick as soon as an excess group-III atom is present. Since the sticking coefficient of the group III sources is approximately one at most growth temperatures, the growth rate is determined by the group-III flux. Overpressure of As during III-As growth is maintained at least 15 times the group-III flux with pressures on the order of  $10^{-5}$  Torr. Furthermore, as the substrate is initially heated past  $350^{\circ}\text{C}$ , As tends to sublime from the bare GaAs wafer, therefore, an excess partial pressure of As needs to be present over GaAs at elevated temperatures. For this reason, large quantities of As need to be available in the chamber and a 500 cc valved As cracker is used for this purpose.

The valve on the As cell is present mostly for convenience in typical growth runs. Since the As flux does not control the growth rate, a rough control of its vapor pressure using a valve is sufficient. Also, due to the large quantity of material that is heated, changing the temperature to control the flux is a very time consuming process. Heating the sublimator from idle to growth temperature can take over an hour. Finally, since a large quantity of material is present and can last a long time, the valve can be closed during a system opening to prevent oxide contamination during the maintenance of other components.

A cracking zone is placed after the valve and sublimator. This is a heated tube with Ta baffles which can convert  $As_4$ , the species which initially sublimates, into  $As_2$ .  $As_2$  has different growth kinetics than  $As_4$  on the growth surface, and material grown with cracked As ( $As_2$ ) can exhibit different characteristics. For example, GaAs grown using  $As_2$  has been shown to have improved PL, reduced deep level defects and lower C incorporation. However,  $As_2$  grown layers also exhibit more shallow donors and are frequently intrinsically *n*-type. Finally, substrate growth temperature can be lower using an  $As_2$  beam, as the incorporation kinetics are improved using the more reactive dimer.

#### 2.2.1.2 Group-V sources: Sb

A similar valved cracker can be used to sublimate and crack Sb. However, in this thesis research, an unvalved 100 cc Applied-Epi model 175 Sb cracking effusion cell was used. Without the presence of a valve, the cell was heated before growth, fluxes measured and then cooled as soon as growth ended. Antimony is sublimated as an  $Sb_2$  species, then cracked at high temperatures into a monomer.

In this particular cell, a Ti baffle and crucible are used which limit the temperature operation of the cell for two reasons. First, cracked Sb is highly corrosive and degrades most refractory metals, such as Ta and Ti. A standard metal valve would fail after just a few days of high temperature use. Second, after corroding the metal within the cell, trace contaminants can deposit on the substrate degrading sample purity. In fact, at full cracking temperatures, trace metals, which matched the alloy constituents in the Ti cracker, were found in samples by the manufacturer. In operation of this cell,

PL was found to decrease as cracking temperature increased; a potential sign of sample contamination. Newer versions of this effusion cell use pyrolytic boron nitride (PBN) valve, baffle and crucible which prevent this contamination problem, and, of course, costs a great deal more.

Before the introduction of Sb into the vacuum system, there seemed to be much trepidation about the Sb oxide “poisoning” vacuum systems, making pump down and bake difficult. Arsenic itself tends to make pump down more difficult due to the large surface area of the As flakes on the walls of the MBE system. However, during a bake the As oxide is quickly removed since it has a high vapor pressure at around 150°C. The remaining As background is then harmless to the growth process. Antimony on the other hand has an oxide which will only sublime at over 500°C. Therefore, if large amounts of Sb are used in a chamber, it is suggested that it be cleaned with every opening in areas of elevated temperature during growth. Luckily, in the GaInNAsSb layers grown for this thesis research, the Sb concentration is very small and only grown in very thin films, therefore, this should not pose a major problem in the vacuum chamber any time soon. The use of a valved Sb cell would also help alleviate this problem.

### 2.2.1.3 Group-V sources: N

The deposition of N is far more challenging than the other group-V materials due to the difficulties of injecting a reactive source of N. Many different sources of N have been used in the past, including ammonia, hydrazine, electron-cyclotron resonance (ECR) plasma or radio frequency (RF) plasma. In this thesis research, an SVT Associates [36] RF plasma source was used for all N deposition. It operates between 200 and 500 Watts at 13.56 MHz with a manually tuned RF matching network. Two other RF sources are popular for this particular application: the Oxford Scientific [37] RF plasma source and the Applied Epi [38] UNI-bulb. The SVT source was chosen at the time since it was the only model which had a removable PBN front plate aperture in which the number, size and orientation of holes could be modified to change the deposition behavior. This was particularly important initially since dilute nitride growth was so new at the time and most N sources were used for high growth rate GaN.

Another advantage of the SVT source is a fully transparent back viewport which allowed for direct monitoring of the plasma glow. However, use of this viewport for plasma characterization does have its drawbacks. For one, monitoring the optical emission of the plasma in this configuration has limited utility. Only the back periphery of the glow is really being measured which is not representative of the active species emitted from the front. Also, the plasma is then not completely confined by the PBN crucible which may sacrifice stable operation and compromise the containment of the N<sub>2</sub> gas.

In general, stability has been the greatest problem with this cell for low growth rate N deposition. Throughout the history of this source, instability came in many different forms. The different types of instability will be described in detail in the remainder of this section, with the intent that future users of this cell can learn from our initial experiences. Some of the problems include: difficulty maintaining a stable flow of injected gas at low flow rates; difficulty in igniting and maintaining a consistent plasma and its degradation over time; and thermal and power instability which sacrificed reproducibility of the deposition process.

The first problem came in the form of flow rate stability. However, this was actually a problem in the mass flow controller (MFC) used to inject the N<sub>2</sub> gas in conjunction with RF interference from the plasma cell. After better isolation of analog and digital circuitry of the MFC, very low, stable flow rates, as low as 0.1 sccm, were possible.

The next stability issue encountered was the difficulty igniting and maintaining the plasma. This problem seemed to worsen with time and it became clear that there were some degradation problems with the source. After months of using the source, the flow rate necessary to ignite the plasma would increase, and eventually the plasma would tend to go out intermittently during growth. There are many thoughts as to why the cell degrades with time, although the exact cause is not yet known. First, decomposition of the crucible is a known problem when using PBN to contain the plasma. The nitrogen from the PBN tends to desorb and the crucible becomes coated with boron dust. The only way around this problem is to replace the crucible regularly and to minimize the duration of the plasma during a growth. Also, As contamination

can be a problem in the crucible, since during a growth when the plasma is turned off, the cell is not heated and As can condense in the cell. In order to minimize this problem, either a gate valve can be used to isolate the cell or long growths which do not need the plasma can be avoided. Initially, we tried to heat the plasma cell during growth by turning on the RF power but not flowing N and igniting a plasma. This is actually not effective since there is a large degree of impedance mismatch between the RF power source and plasma coils while the plasma is turned off. All the power is then dissipated in the matching network capacitors and not through the plasma coils in the cell.

Finally, another likely source of poor stability and degradation is the grounding or coupling of the RF power from the matching network into the plasma coils. Each time the cell was connected to the power supply the plasma stability worsened. After a while, the plasma would go out with shutter openings, or quick changes in flow rate. At times enough charge would build up on the ground plane of the power feedthrough that it would frequently spark and also destabilize the plasma. This problem was apparent since the RF reflected power between cell and matching network was much higher than specifications, indicating a power coupling issue. Replacing the RF matching network box caused many of these issues to go away, however, a new power feedthrough design is recommended to further solve plasma stability problems with this cell.

One major difference in cell designs between manufacturers is the type of variable capacitors used for impedance tuning in the matching network box. SVT decided to use much cheaper open air parallel plate tunable capacitors, while Applied-Epi and Oxford employ a much more reliable vacuum sealed design. The open air capacitors are much more sensitive to changes in the ambient environment such as humidity, temperature and electrostatic attraction of dust particles which can degrade the capacitors. This could be a problem in future use and may be one reason that changing the matching box after two years improved stability.

Another stability problem with the SVT source, not found with other manufacturers, has been thermal and power stability. This cell takes as long as 30 minutes for the temperature and reflected RF power to stop fluctuating. Over that time,

plasma properties and N deposition rates are expected to change. In other cells this process only takes a few seconds. One factor in thermal stability is the higher than normal power required by this cell over others. The RF coils which contain the plasma are less tightly wound than in other cells, reducing the coupling efficiency and overall power density. Therefore, much higher powers (300 W versus 60 W in other cells) are required to maintain a glow, generating much more heat around the coils which take time to stabilize. Also, better thermal shielding and heat sinking may play a role in heat removal and thermal stability. The current solution to this problem has been to run the cell for a given time before nitride growth begins. However, this is not viable in some cases since the layers before the nitride growth can be very thin and only a few minutes would be available to stabilize the plasma.

Another issue in all plasma deposition cells, not related to stability, has been the so-called “blow by” of reactive N around the shutters. This means that with the shutter closed and plasma running, a significant amount of N deposits in the growing material. In our case, this has been on the order of one tenth the deposition rate of N in layers with an open shutter. This indicates that the N deposition is not completely line of sight and the active species can survive the path around the shutter, bouncing off the walls of the chamber. In many cases, this problem can be ignored, however, it has been found that if the plasma is running during AlGaAs DBR growth, the laser thresholds are extremely high. Also, the blow-by occurs during plasma ignition and during growth rate instability, making the concentration in this region inconsistent. In other shutter configurations which less effectively block the cell aperture, the problem is more severe and as much as 50% shutter blow-by has been observed. This effect can be greatly reduced by using better shutter designs, or placing the source behind a differentially-pumped gate valved port.

Plasma deposition is a very complicated technology and ways to optimize deposition and remove defects are not completely understood. Further discussions of plasma cell operating procedure and plasma characterization will be discussed in later sections.

#### 2.2.1.4 Group-III sources: Ga and In

The group-III metals, unlike most group-V sources, have a significant vapor pressure through evaporation instead of sublimation. Therefore, the source material has to be taken past its melting point and, consequently, the shape of the melt affects the shape of the molecular beam. Under As rich conditions, the shape of the beam greatly affects the growth rate uniformity across the wafer. Another difficulty particular to Ga and In is that neither wets PBN, the most common crucible material. Over time evaporated and re-condensed material beads up on the walls of the crucible. The droplets then fall back into the hot liquid and spray metal onto the substrate, creating the so-called “oval defects” [39,40]. The original crucible geometry consisted of a conical trumpet shape which was designed to minimize the effect of the changing melt volume during source material depletion. However, there are many disadvantages to this design. First, the crucible capacity is reduced using this shape over other designs. Also, there is a tendency for droplets to condense on the cooler lip and then fall back into the melt. Lastly, there is a large amount of wasted material since the beam expands uncontrolled past the substrate and deposits material on the walls of the chamber.

The first modification to design was the use of the two zone heater [41]. In this configuration a separate filament ensures the tip is always hotter than the source material and the evaporation at the tip is greater than at the base. This greatly reduces oval defects caused by metal droplets at the tip. The next alteration to the crucible design was the SUMO cell which consisted of a straight walled cylindrical crucible with a small tapered orifice. This source also makes use of the dual filament heater design preventing droplets from forming on the tip. It also has the added benefit of flux uniformity since now the beam profile is defined more by the tip opening and not as much by the depleting melt surface. It also reduces thermal transients caused by the insulating properties of a closed shutter, increases the charge capacity over conical crucibles, and increases the efficiency now that the beam can be more focused on the substrate.

Both conical and SUMO crucibles, and single and dual filament sources were used in the MBE systems at Stanford. It has been found that the dual filament design

does reduce oval defects when using Ga and In cells and does improve flux stability during the course of a growth. However, it has been reported that in dual filament conical cells, source material efficiency does decrease. SUMO cells have been found to improve oval defects even further, and reduce the long term beam profile changes due to source material depletion effects. Using a dual filament SUMO cell, oval defects were observed to be reduced by approximately ten times. The increased capacity is also useful since the most common reason to open the chamber is to replace depleted group-III metals.

An important operating parameter which effects shutter transient and oval defects is the heating configuration between the two tips. The manufacturer's specification indicates many different ways to control temperature between the two zones. The least stable configuration has been to control the tip heater using the base thermocouple. The reason for this arrangement is to keep the tip much hotter than the base to prevent droplets from forming on the tip but to better control base temperature since it controls the evaporation rate. While this may work well for long growths and utilizes only one temperature controller, it has been found to be most susceptible to shutter transient instability. A shutter opening was found to influence the tip temperature by up to 10°C. Thus far, the most stable operation has been to control both zones independently with their respective thermocouples, but with the tip fixed at 150 degrees hotter than the base. This seems to provide the most stable heating, reduced oval defects and minimized shutter transients.

One disadvantage to an evaporation source over a flow controlled deposition source is the difficulty in changing the growth rate *in situ* without recalibrating. Unlike controlling gas flow rates, evaporation rate is only loosely controlled by source temperature, therefore, compositional grades by MBE become very difficult. Current MBE systems alleviate this problem by using multiple group-III sources and digitally grading composition. However, this solution can be quite wasteful, increases the number of sharp interfaces in a structure, increases cost and reduces the reliability of MBE systems. Until there is a better solution for MBE group-III sources, this will always be a disadvantage over gas injection techniques. With future MBE source design, one can imagine a valved evaporation source which could control growth rate

with a calibrated valve position. This is much more challenging than designing a valved sublimation source since the condensate could liquefy and clog the source. Nevertheless, it might be possible for Ga and In since they would not wet a hot PBN valve and this solution has been considered by component manufacturers.

#### 2.2.1.5 Group-III sources: Al

An evaporation source for Al is very similar to Ga and In, except that Al wets PBN and tends to creep out the top of the crucible. Therefore, an Al source needs to have a cold tip to prevent the charge from running out of the cell. Since the metal wets the crucible, and has a large thermal expansion and a high melting point, one has to be careful while freezing the melt so the crucible does not break. Even though Ga expands 3.1 percent on solidifying, there is less risk when freezing since it does not wet and its melting point is near room temperature. Double wall crucibles are manufactured for Al source material, however, this is only really recommended to prevent catastrophic failure if the crucible were to crack. Replacing the Al crucible after every freeze is still always recommended.

#### 2.2.1.6 Dopant sources: Be, Si, C

Providing dopants during growth is much easier and with higher quality results than implanting or diffusing them in the GaAs crystal. A common *n*-type dopant in GaAs is Si and *p*-type dopants are Be and C. Using a sublimation thermal source, Si can dope GaAs across a wide range of electron concentrations with little diffusivity. On the other hand, Be and Zn have much lower achievable hole concentrations with much higher diffusivity. Beryllium is also deposited using an evaporation thermal source, however, at high dopant concentrations it diffuses interstitially and segregates towards the surface, limiting the dopant concentration to below  $10^{20} \text{ cm}^{-3}$ . Carbon does not have these issues, but it is much harder to deposit. As an alternative to using a C filament source,  $\text{CBr}_4$  gas injection systems have recently been used for high doping densities. Carbon does not have the same surface diffusion problem the other *p*-type dopants have and can incorporate in the  $10^{20} \text{ cm}^{-3}$  range with no evident Br incorporation. The  $\text{CBr}_4$  is cracked at the substrate, eliminating the need for pre-

cracking in the gas injector. In this thesis research Si, C and Be were used for GaAs doping.

The main operational difference between a dopant effusion cell and a group-III effusion cell is the calibration of the incorporation rate. The vapor pressure from a dopant cell is too small for an accurate beam flux measurements to be taken. Therefore, the evaporation temperature is calibrated directly to dopant concentration using *ex situ* carrier concentration measurements. Also dopant cells are commonly ramped in temperature to give dopant grades, since the precise incorporation rate is not usually necessary, the dopant effusion cell is small, and the temperature ramp can be correlated well with the doping level.

## **2.2.2 MBE components**

### 2.2.2.1 MBE source shutters

Of all the MBE components, source shutters can be a highly problematic component and is a major source of system down time and non-uniformity in growth rates. The source shutter is a thin piece of material shielding the substrate from line of sight with the evaporating molecular beam. The current shutter materials available are Ta or PBN, both with their own tradeoffs. Both have different effects on shutter reliability and growth rate instability from shutter transients. Shutters tend to be unreliable since source material will stick to its surface, increasing the weight or dripping between the shutter and chamber wall, freezing it shut. Both Ga and In do not stick to PBN but wet Ta therefore PBN is the preferred material for these source shutters. Aluminum does wet PBN and Ta therefore there is no difference in shutter material in this case. Another advantage of PBN over Ta is the reduction of thermal shutter transients. This occurs when the shutter closes over the source and insulates the heaters. Then when the shutter opens for growth, the heat loss quickly increases in the cell and the temperature first decreases, followed by heater compensation, which results in growth rate oscillations. Also, the large changes in heat from shutter openings can have an effect on substrate temperatures. Tantalum greatly insulates the source heaters, contributing to substrate thermal transients. PBN shutters greatly reduce this problem since the material is transparent to the thermal radiation. Also, a two zone heater with

properly controlled tip and base temperatures better isolates the source material temperature from the shutter thermal transients. For some reason, Al is less susceptible to these temperature fluctuations, possibly due to its higher heat capacity. Because of this, and its wetting properties, Ta is a viable solution for Al shutters while PBN is preferred for Ga and In.

One exception to this shutter configuration is with the growth of GaN. Here the growth takes place under Ga-rich conditions with a few monolayers of group-III metals coating the growth surface. In this growth mode there is enhanced surface mobility and improved N incorporation. During the high temperature GaN growth, Ga tends to desorb from the substrate and coat the shutters. Then after ramping a source temperature or closing a shutter, Ga will desorb from the shutter and deposit back onto the substrate. In order to alleviate this problem, Ta shutters are used in GaN chambers since they absorb more heat and help prevent Ga from ever condensing.

#### 2.2.2.2 *In situ* monitoring

Many different types of *in situ* measurements can be taken during MBE growth. Some of the properties which can be measured include growth rate, substrate temperature, layer thickness, composition, film stress, and surface metrology. In many cases, the most important growth parameter is the group-III growth rate. The simplest way to determine growth rate is to measure the beam flux of a source that has a known growth rate versus beam flux dependence. However, between each growth, particularly if the source temperature has recently been ramped a great deal, this is only accurate to within about 5%.

Many more accurate optical techniques can be used to monitor growth rate, such as normal incidence reflectivity using a white light, or a monochromatic beam [42,43], pyrometric interferometry [44], ellipsometry [45,46], or optical flux monitoring [47]. In normal incidence reflectivity, incident light interferes with different layers on the substrate and layer thickness can be calculated using the known index of refraction for each layer. Difficulties include the coating of optical viewports which need to be exposed for an extended period of time, and an uncertainty in the index of refraction and temperature of each layer. However, by self-calibrating using RHEED oscillations

or *ex situ* techniques and using pyrometry to measure the temperature, normal incidence reflectivity can be a powerful technique to control layer thickness and composition.

A new optical monitoring technique that is being developed for MBE is optical flux monitoring. This technique passes monochromatic light, which is in resonance with an atomic absorption edge for each source, close to the heated substrate where the growth is occurring. This measurement can be extremely accurate and may actually determine dopant fluxes which typically don't contribute appreciably to the growth rate. When combined in a closed-loop system, optical flux monitoring can significantly contribute to composition and growth rate control over the course of a growth. This type of measurement was not used for the samples grown in this work, but could greatly improve layer thickness and compositional control in future growths and could possibly enable compositional grading.

One of the most useful *in situ* monitoring tools used for very accurately growth rate calibration is reflection high-energy electron diffraction (RHEED). Intensity oscillations from electron diffraction provide a quick, direct measure of growth rate [48]. As growth is initiated, the crystal surface is smooth and the specular electron reflection is bright. As growth proceeds and the next layer nucleates, adatoms and islands form and the specular spot dims due to scattering until the layer is fully covered and diffraction becomes bright once again. As monolayers deposit the RHEED intensity continues to oscillate and the oscillation frequency is proportional to the monolayer coverage and the period of intensity oscillations corresponds to one complete monolayer of growth. Measuring RHEED oscillations has many limitations and really can only be done for the first 5-50 monolayers of growth. Intensity oscillations can only be measured without substrate rotation, which leads to non-uniformity across the wafer and damps the diffraction signal after a few seconds. Since the measurements are only taken at the start of the growth, shutter transients are a source of error and the measured growth rate is typically faster than the actual value. However, this may give a more accurate measurement for thin layers. Despite the limitations, being a direct measure of layer deposition it can be accurate to within a couple of percent. RHEED oscillations are possible when rotating the sample, but it

requires several hundred r.p.m. substrate rotation and sampling the diffraction intensity at only specific azimuthal angles [49].

Another *in situ* measurement particularly important to homogenous nitride-arsenide growth is substrate temperature. Two-color infrared pyrometry was used to measure sample temperature during growth. The pyrometer is specifically designed to be insensitive to window coating problems and instrument alignment errors. In order to calibrate the pyrometer, various known temperatures can be used, including the GaAs oxide blow-off temperature at 582°C [50], the In melting temperature at 157°C [51], the Si-Al eutectic at 577°C [52], or various surface reconstruction transition temperatures [53]. Using RHEED, one can clearly monitor these transition temperatures on the substrate. Unfortunately, most pyrometers are not sensitive to blackbody emission below 400-450°C. At low temperatures, an accurate substrate temperature reading can be taken by measuring the GaAs bandgap via transmission using radiation from the substrate heater or a white light source. This can be a highly accurate temperature monitor since the GaAs bandgap is a well defined function of temperature. However, uncertainty in the doping levels of the bare GaAs wafer and the dopant influence on bandgap versus temperature can add some degree of error.

Other types of measurements can also be taken during growth. One useful measurement that was not used, but would be applicable to highly strained GaInNAs growth, is the real time quantitative measurement of accumulated stress. The measurements are performed by following stress-induced substrate curvature during growth through the deflection of a laser beam [54,55]. This measurement would be useful in strained film growth, since it can quickly determine the critical thickness in films by measuring the point where stress is relieved through dislocation generation.

### 2.2.2.3 Vacuum pumps

The proper vacuum system can be a key factor for rapid pumping times and high quality material growth. During traditional III-V SSMBE growth, the most important pump is the liquid nitrogen cryoshroud that surrounds the substrate. This can greatly reduce defects and cross source contamination. For GaAs growth, only a cryoshroud and an ion pump are necessary to maintain a  $10^{-10}$  Torr background after a

chamber bake. During N plasma growth, large amounts of N<sub>2</sub> are injected into the system. A high pumping speed cryopump, such as a Helix Technology CT-8 [56] provides sufficient pumping with N capacity of over 1,000 liters. Vacuum can be maintained for weeks before cryopump regeneration. During nitride growth, background pressures get too high and pumping speeds are too low for a typical ion pump. A turbo pump would be a viable alternative to a cryopump, avoiding the frequent cryopump saturation and regeneration cycle.

### **2.2.3 Traditional III-V MBE growth**

In traditional III-V growth, group-III sources control the growth rates depositing with a unity sticking coefficient. Therefore, precise group-III temperature control is crucial in obtaining reproducible results, since changes as little as 0.5°C can lead to growth rate changes as large as one percent. Extremely stable feedback loops are used for temperature control using type-C Tungsten-Rhenium thermocouples and proportion, integral, and derivative (PID) temperature controllers. These feedback loops can be accurate within 0.1 degrees, however, that is only at full power; at lower power they are much less accurate. The most accurate way to power the source heaters is to use direct current (DC) power supplies with variable voltage and constant power. However, currently at Stanford, silicon-controlled rectifier (SCR) alternating current (AC) power supplies are used for all source heaters due to their lower cost. DC power supplies are used only for substrate temperature control, since AC power would interfere with the RHEED gun electron beam.

Before growth begins, samples are loaded in a load lock and baked at around 350°C; above that, As desorbs from the GaAs surface. The wafers are then loaded onto the substrate heater using a magnetically coupled transfer rod. The substrate heater can rotate on two axes; one axis rotates between loading and growth positions, and another is a continual azimuthal rotation (hence the name “CAR”) used for substrate uniformity. Sample temperature is first ramped to the As desorption temperature where the As is turned on to prevent desorption. Then at 580°C, the oxide blow-off is monitored by RHEED and the sample is held at around 600°C for 15 minutes to completely remove any contaminants. After the high temperature outgassing, a thick

GaAs buffer layer is grown to flatten the surface and cover any defects present on the bare wafer. Before the sample is loaded, flux measurements are taken for each source to roughly measure growth rates. At this time, more accurate RHEED intensity oscillations can be measured for growth rate calibration.

At temperatures up to about 650°C, Ga incident on a GaAs substrate has unity sticking coefficient. For the highest quality and lowest surface roughness films, GaAs is grown right around the GaAs oxide blow off temperature of 580°C. AlAs on GaAs has near unity sticking even above 700°C, but high quality, low surface roughness AlAs is grown about 20 degrees hotter than GaAs. Microscopy techniques sensitive to surface roughness are a good measure for the proper growth temperatures. Depending on whether the sample roughness is ordered along crystallographic directions or randomly oriented, one can determine if the sample temperature was too hot or cold during growth. InGaAs on GaAs is grown at much lower temperatures. Indium desorbs from GaAs at temperatures higher than about 430°C. Despite this, high quality InGaAs is commonly grown around 480-520°C under careful substrate temperature control, since desorption rates are a strong function of surface temperature.

## **2.3 GaNAs Growth**

### **2.3.1 Nitrogen RF plasma**

Among the many ways to deposit N by MBE, the highest quality material grown thus far has been using an RF plasma source. Nitrogen solubility in GaAs is very low, and N<sub>2</sub> incorporation in GaAs would be negligible. Even though standard MBE growth is carried out far from thermodynamic equilibrium, a highly reactive N source, such as a plasma, is necessary for appreciable incorporation. Dissociated atomic and molecular radicals and ions are generated in the plasma and escape from a front aperture plate towards the substrate, depositing in high concentrations. Ions generated in the plasma can be accelerated by the RF fields and cause substantial energetic ion damage to the growing epitaxial layer, while radical neutrals should inflict little damage and incorporate on substitutional sites. There are many different parameters which can control the plasma, including forward RF power, reflected RF

power, injected  $N_2$  flow rate, ion deflection plate bias, and the size, number and location of holes in the front plate which allows N to escape. Few analytical techniques are currently available in the MBE to measure the plasma properties and determine ideal operating conditions. Furthermore, it is not yet clear what characteristics of the plasma are beneficial to high quality crystal growth and which contribute to crystalline defects. An RF plasma is chosen over other plasma sources for its low ion count and high atomic dissociation yield [57].

Dilute nitride GaNAs is a relatively new alloy in the III-V field and RF plasma sources had originally been used to growth high growth rate GaN. Plasma cells and gas injection systems were designed for growth rates around  $1 \mu\text{m/hr}$ , although recent high quality GaN growth has been done at much lower rates. Originally, the plasma source was modified to run at low flow rates (0.1-1 sccm) by using 9 holes in the front exit aperture, each 0.25 mm in diameter. The holes were arranged in a square geometry of  $3 \times 3$  spaced about 3 mm apart in order to maximize the uniformity of the escaping radical N. A photograph of the front of the plasma source with a 30 hole output aperture is shown in Figure 2.4.

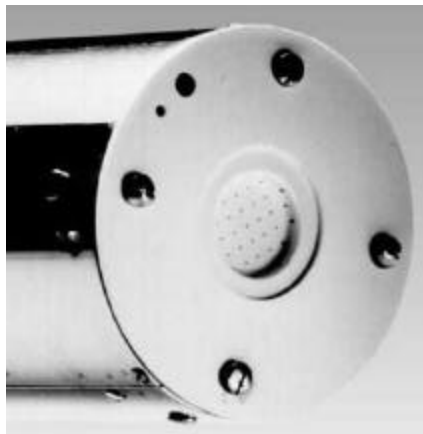


**Figure 2.4: Front of an SVT Associates plasma source with mounted PBN plate and 0.25 mm holes [58].**

### **2.3.2 Plasma cell operation**

A gas injection system, see Figure 2.5, was designed close to the MBE system to regulate a stable flow of ultra high purity  $N_2$  into the MBE. A low flow rate (5 sccm

at full scale) mass flow controller (MFC) placed behind a manual variable leak valve was used to accurately control flow rates. A low pumping speed turbo pump was used to purge the N<sub>2</sub> lines and to pump the system when the leak valve to the chamber was closed. The highest purity gas and a gas filtering system were chosen to reduce O<sub>2</sub> contamination from the N<sub>2</sub> gas handling system, which is potentially a significant source of defects in the nitride grown material. Nitrogen is injected into the plasma cell and the plasma is ignited using the following procedure:

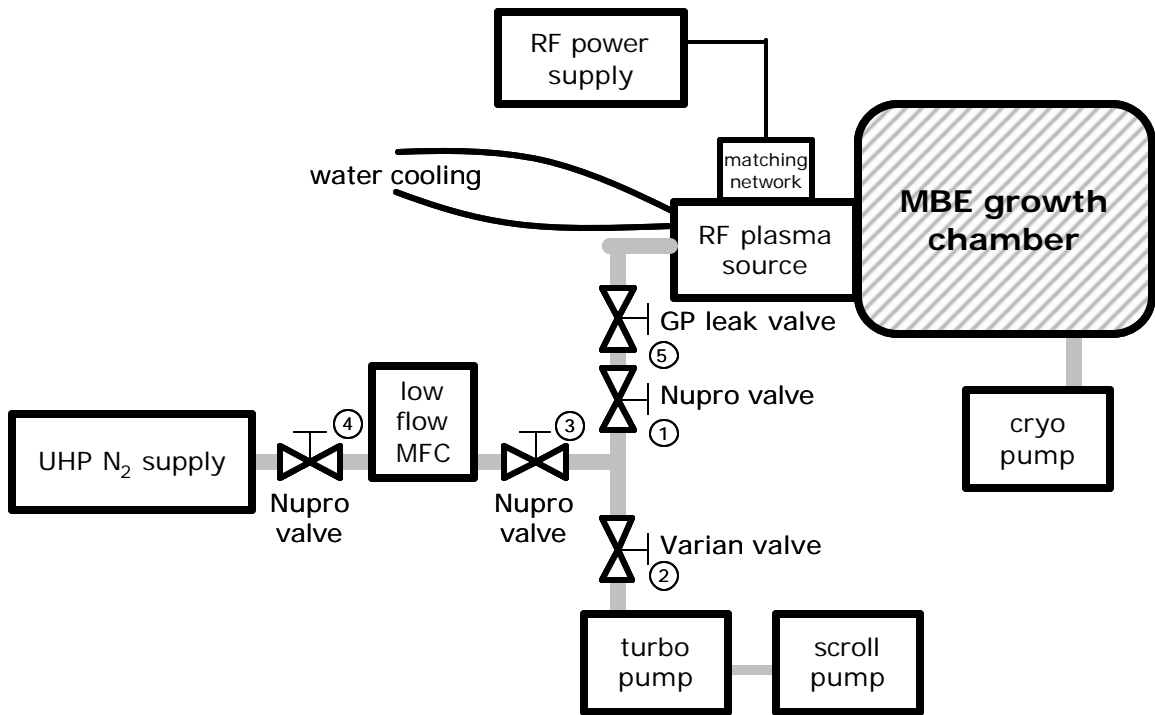


**Figure 2.5: Schematic of N<sub>2</sub> gas injection system**

1. With the valve (1) to the plasma source closed, the lines beyond the MFC are pumped by first setting the mass flow to zero and opening the valve (2) to the turbo and valve (3) to the MFC.
2. Valve (4) is opened and N<sub>2</sub> is flowed through the MFC at around 1 sccm for 10 minutes to purge the system.
3. The RF power to the plasma cell is ramped to 300 W and the leak valve (5) to the MBE chamber is opened to about 50% of full scale. The RF reflected power is minimized using an impedance matching box to

around 60 W. While the turbo pump is running, the chamber pressure only reaches the mid  $10^{-6}$  Torr.

4. The valve to the turbo pump is closed and a plasma is ignited in the cell almost immediately. At this point, the pressure in the chamber reaches the mid  $10^{-5}$  Torr. Since the gas is well contained in the plasma source by a crucible with a small aperture, the pressure in the cell is on the order of mTorr. At these high pressures, the mean free path for the gas is very short and the plasma is mostly made up of molecular  $N_2$  radicals. The intensity of the glow is very weak and is called the plasma “low intensity mode.”
5. The  $N_2$  flow is then reduced to around 0.2 sccm and the plasma changes into (within about 30 seconds) a “high intensity mode.” Under these lower pressures the mean free path is longer and there is a high ratio of atomic to molecular N generated by the RF field.
6. In the high intensity mode, the RF power is coupled very efficiently into the plasma and the impedance characteristics quickly change. Using the RF matching box, the reflected RF power is again minimized, this time to a value usually around 1-5 W. The flow rate is then very slowly raised to 0.25 sccm, while the reflected power is kept minimized.
7. Under these final flow conditions, chamber pressure is in the low  $10^{-5}$  Torr range and with the shutter closed, N incorporation is very low. The shutter can then be opened and closed to modulate the N beam.

The flow rate used during growth was originally developed to have low incorporation of N and to maximize the atomic to molecular N ratio. Optimization of the plasma will be described in the following section. However, it quickly became clear that the MFC was not very stable at a flow rate of 0.25 sccm. With the RF power on, the flow rate would drift around  $\pm 20\%$ , frequently causing the plasma to go out. Faced with this problem, a decision was made to reduce the number of holes in the front aperture plate so the flow rate could be increased. While there were a number of stability problems found in the plasma cell design itself, as discussed in section 2.2.1.3, this particular issue turned out to be a defect in the MFC. After frequent discussion

with the manufacturer of the MFC (Unit Instruments [59]), it was eventually discovered that the digital and analog electronics were not properly isolated and the controller would be highly susceptible to noise under RF interference. The MFC was repaired and the low flow operation while using the RF power was now noise-free, however, the plasma cell had already been modified. A new front plate was installed with 4 holes, each 0.25 mm in diameter, and this time in a Y configuration. There were some expected and unexpected consequences to this change.

By reducing the number of holes in the exit aperture, as expected the required flow rate for the same deposition rate increased. By reducing the holes by more than half, the optimal flow rate increased from 0.25 sccm to 0.5 sccm (from step 6). The flow rate necessary to change into high-intensity mode (step 5) now decreased from 0.2 sccm to the lower limit of the MFC (between 0.1 sccm to completely closed). This was because the pressure within the cell crucible was now much higher for the same flow rate. Plasma properties are expected to be different and an unexpected improvement in material quality which resulted will be discussed in section 4.1.3.

### **2.3.3 RF plasma optimization**

Many questions still exist when trying to understand deposition mechanisms using a plasma deposition source. With optical emission spectroscopy (OES), one can optimize the atomic N versus molecular N yield, or by using an ion counter, the ion emission from the plasma can be minimized. However, it is not yet known which plasma species incorporates as substitutional N, and which species damages crystal, incorporates in interstitial sites, or leads to deep level defects. Using the current understanding of plasma deposition, steps were taken to optimize cell operation. The plasma operating parameters were optimized in order to reduce the number of ions and increase the atomic to molecular N yield.

Optical emission from the N plasma glow was taken by coupling the light from the back of the cell through a fiber optic cable into a spectrometer and the emission spectra was detected using an optical chopper and standard lock-in techniques. The measured OES for the N plasma running at 300 W is shown in Figure 2.6. The relative yield of molecular N<sub>2</sub> is proportional to the intensity of the broad peaks located at

approximately 550, 580, and 650 nm. The broad linewidth is related to the quantized molecular rotational modes in the plasma. The atomic N yield in the plasma is proportional to intensity of the sharper peaks located at 740, 820 and 870 nm [60]. The ratio of the peak intensity of an atomic transition peak and a molecular transition peak is proportional to the ratio of atomic to molecular N in the plasma. This procedure was performed as a function of flow rate and RF power [61], however, as mentioned above, this procedure is not entirely accurate. The spectrum is taken from the back of the cell, while the emission from the front, where the active N leaves the cell towards the substrate, is absorbed as it travels through the plasma. The pressure in the cell is relatively high and a great deal of recombination of dissociated species can occur near the front apertures where the N escapes.

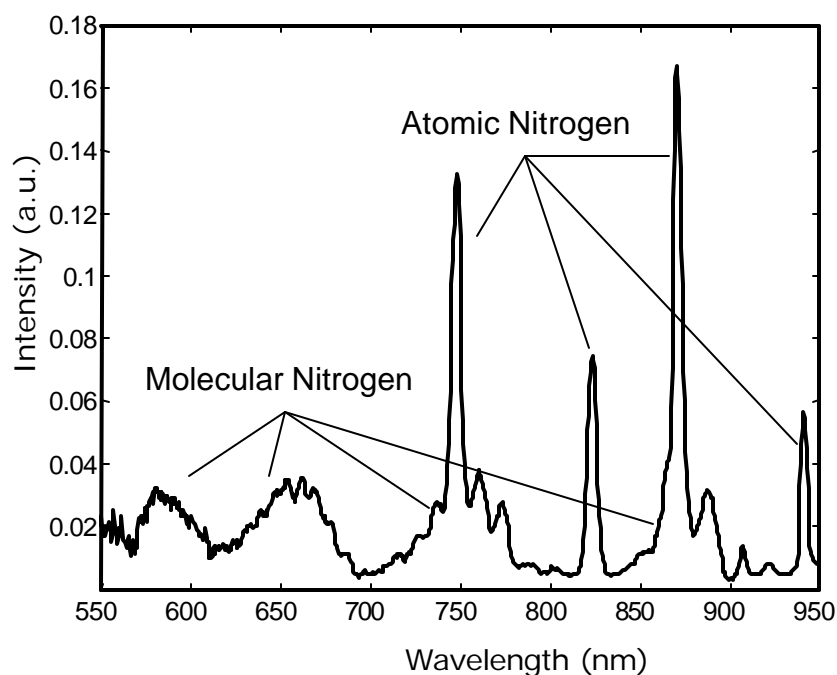


**Figure 2.6: Optical emission spectrum from back of plasma cell at 300 W RF power and 0.25 sccm flow of  $N_2$ .**

Another important plasma property is the amount of high energy species that escapes from the cell and inflicts damage to the epitaxial layer. These can either be ions that leave the plasma and are accelerated due to their charge, or ions that are accelerated within the plasma, recombine with an electron before leaving but still

escape highly energized from the cell. With proper plasma design, a deposition cell should have a very small amount of ions accelerating towards the substrate. Two ion deflection plates are located in front of the exit aperture in order to deflect the ions away from the sample. These plates can be biased with a high voltage while the cell is operating. However, with the above operating parameters, very little difference in material quality was found with and without bias on the plates. Extremely high energy ions may still travel unabated towards the sample and accelerated neutrals would not be deflected by the charged plates. Other plasma conditions can also strongly affect the energy of emitted species, including the mean free path of the gas in the cell. By increasing the pressure in the cell by reducing the size of the front aperture, the number of ions and high energy neutrals can decrease.

With all these issues in mind, a quick procedure was developed in order to initially optimize plasma cell parameters. Since the atomic N optical emission is much brighter than molecular N, simply measuring the total emission intensity with a Si photodetector can give an indication of the atomic to molecular ratio. The flow rate of gas to the cell strongly influences the atomic yield by affecting the mean free path of gas species in the cell. At a low flow rate, the integrated intensity is small since the plasma density is decreased. While increasing the flow rate, the emission intensity increases, reaches a peak, and then begins to fall. Above the peak emission intensity, the mean free path of the plasma is too short and the atomic species recombine too quickly. Below the peak emission intensity, the mean free path is long and ion creation and emission is high. An ideal flow rate is slightly above the peak intensity condition, so that atomic yield is still high, but both ions and accelerated neutrals quickly scatter and cannot leave the cell. This relationship of plasma properties as a function of flow rate is drawn schematically in Figure 2.7.

Next, the optimized RF forward power can be determined. In most cases, the power should be enough to sustain a stable plasma, but not too high whereby it generates higher energy species. Both the minimum stable power for ignition and sustained growth were determined by trial and error. As discussed in section 2.2.1.3, the minimum power is greatly influenced by RF coil design, and for the SVT plasma source, stable operating conditions were possible for powers only above 250 W. Other

manufacturers design cells which are stable at around 60 W. Finally, the reflected RF power can be optimized. Any mismatch off the minimum reflected power will be dissipated by the capacitors in the matching box. Therefore, the impedance should be closely matched. However, the minimum reflected power can change based on many environmental factors, so in order to maintain consistent forward power between runs, a reflected power slightly off minimum was used. In this case, 1-3 W was the typical minimum reflected power, thus 5 W was chosen as the standard constant reflected power for all runs.

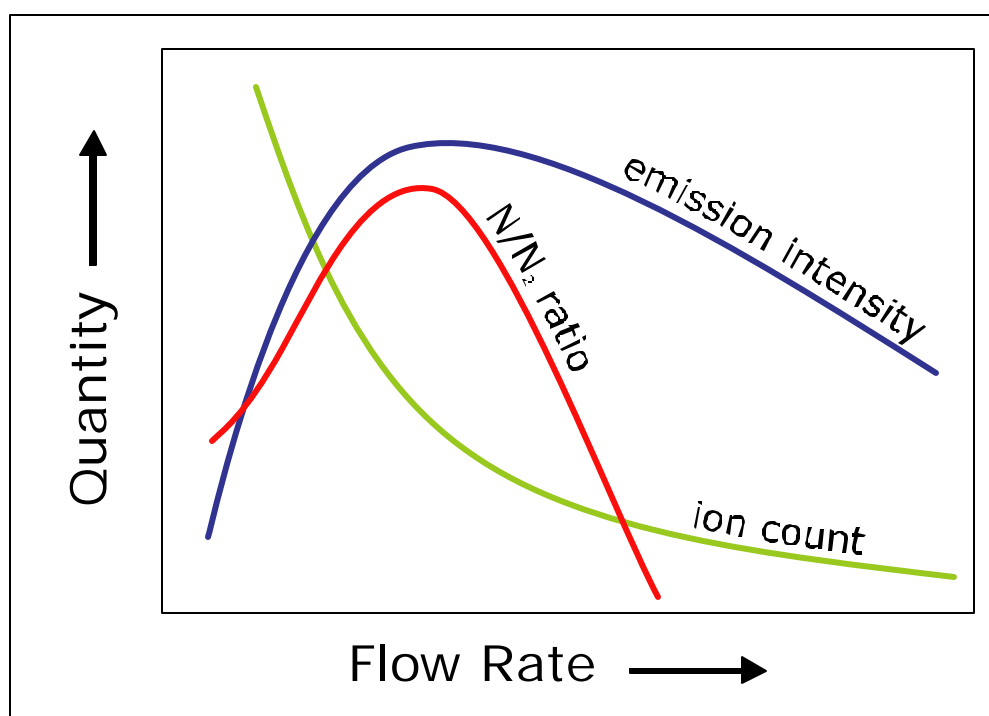


**Figure 2.7: Schematic dependence of emission intensity, ion count, and atomic to molecular ratio with the gas flow rate.**

### 2.3.4 Nitrogen concentration control

After following the plasma optimization technique, as described in the previous section, the cell parameters were fixed at 300 W with 0.25 sccm for nine holes and 0.5 sccm for the four hole aperture. To control the N concentration in epitaxial growth, it is essential to have reproducible and consistent plasma operation. In order to achieve this,

the plasma source was operated under the above conditions and variation of N composition was achieved by varying the group-III growth rate. It was found that the N concentration follows an inverse dependence on group-III growth rate, with a linear dependence up until concentrations as high as 10%, as shown in Figure 2.8 [61]. This dependence is due to the fact that within a certain energy range of the depositing N species, all incident N sticks and is incorporated in the GaAs growth front. The faster the GaAs growth rate, the lower the N composition. Other research groups control N incorporation by varying the flow rate or RF power, however, as explained above, varying power or flow rate can greatly modify plasma operating characteristics and can change material quality.

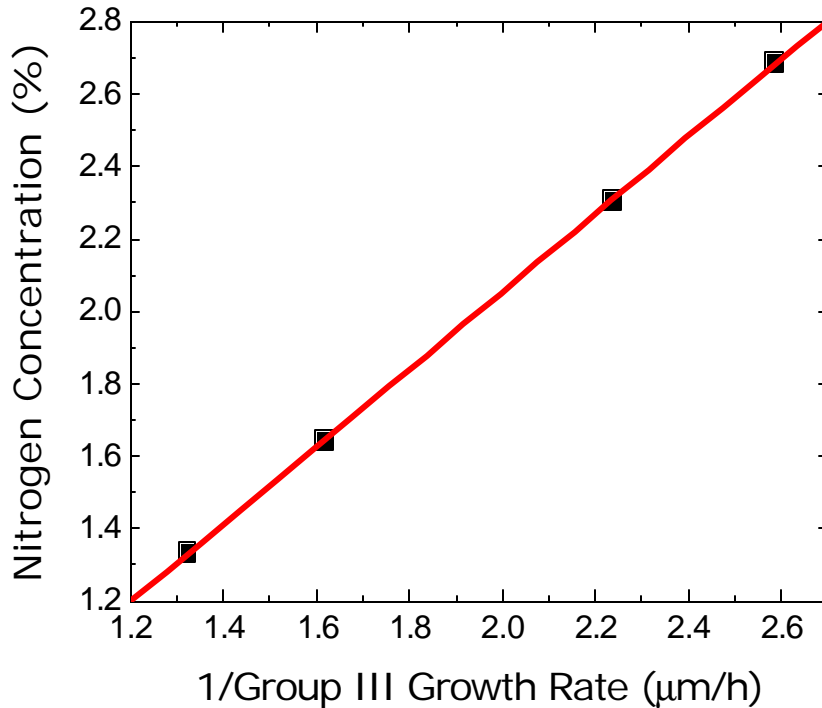


**Figure 2.8: Concentration of GaN in GaAs as a function of GaAs growth rate using 300 W RF power and 0.5 sccm flow of  $\text{N}_2$ . Concentrations measured by HRXRD. A linear relationship was observed up to 10%.**

The unity sticking-like characteristic of N deposition is very beneficial and different than the growth dependence of other mixed group-V systems. For instance, in the mixed As-P system, both components desorb from the surface and their desorption

rates are highly dependant on substrate temperature and the flux of the other component [62]. Reactive N which deposits on substitutional sites is relatively independent of the temperature at the surface and acts much like a dopant or a group-III component with unity sticking coefficient. This improves compositional control and wafer uniformity during crystal growth.

### **2.3.5 Nitride-arsenide proprieties**

Nitrogen and arsenic are very different elements and, consequently, GaAs and GaN have significantly different properties. Table I lists selected material properties for arsenide based materials while Table II lists material properties for relevant nitride based materials. Because of the difference in size and electronegativity (3.05 for N, 2.18 for As) between the N and As atoms, the two compounds vary greatly in electronic structure, bandgap, mechanical properties, and crystal system (hexagonal versus cubic). Because of the high electronegativity and small size of the N atom, the nitride based materials, in general, have stronger, shorter bonds, resulting in a larger bandgap and stiffer mechanical properties. Due to the large differences in electronic structure there is a very large miscibility gap between the GaAs-GaN range of alloys. In fact, on the dilute nitride side only a fraction of a percent of GaN is soluble in GaAs under equilibrium conditions [63,64]. Materials grown with more than this concentration of N would undergo phase segregation in which GaN and GaAs would separate into a two phase inhomogeneous material. This second phase could act as non-radiative recombination centers or lead to inhomogeneous material with fluctuating composition and bandgap.

**Table I. Material constants for As-based materials at room temperature [65,66].**

	GaAs	InAs
Crystal structure	Zinc-blende	Zinc-blende
Lattice Parameter [Å]	a = 5.6533	a = 6.058
Energy Gap [eV]	1.428	0.358
e <sup>-</sup> Mobility [cm <sup>2</sup> /Vs]	9300	2000-4000
e <sup>-</sup> Effective Mass (G) [m <sub>0</sub> ]	0.0636	0.026
Free Energy of Formation (D G <sup>0</sup> <sub>f</sub> ) [kcal/mol]	-16.97	-10.22
Elastic Constants: c <sub>11</sub> [GPa]	1221	832.9
c <sub>12</sub> [GPa]	566	452.6
c <sub>44</sub> [GPa]	600	395.9

**Table II. Material constants for N-based materials. Parameters for zinc blende crystal structures are based on theoretical models at room temperature [65,66].**

	GaN	GaN	InN	InN
Crystal structure	Wurtzite	Zinc-blende	Wurtzite	Zinc-blende
Lattice Parameter [Å]	a = 3.19 c = 5.185	a = 4.5	a = 3.545 c = 5.703	A = 4.98
Energy Gap [eV]	3.507	3.299	2.07	1.94
e <sup>-</sup> Mobility [cm <sup>2</sup> /Vs]	440		250	
e <sup>-</sup> Effective Mass (G) [m <sub>0</sub> ]	0.2	0.15	0.12	0.12
Free Energy of Formation (D G <sup>0</sup> <sub>f</sub> ) [kcal/mol]	-33.04		-22.96	
Elastic Constants: c <sub>11</sub> [GPa]	390	293	233	187
c <sub>12</sub> [GPa]	106	159	92	125
c <sub>44</sub> [GPa]	105	155	48	86
c <sub>13</sub> [GPa]	145		115	
c <sub>33</sub> [GPa]	398		224	

### 2.3.6 Instability in a regular solution

The regular solution model is a convenient way to classify different types of solutions according to the interaction strengths of the different components. In any solution there is a movement of atoms causing localized fluctuations of composition. With a thermodynamic driving force, these fluctuations may result in a configuration that reduces the energy of the system and the material can decompose into a mixture of phases. If the energy of the decomposed mixture is lower than the homogenous solution, the system will be most stable as a mixture of phases. Figure 2.9 illustrates an example of the free energy of a solution where, at low temperatures,  $T < T_c$ , it becomes unstable as a homogeneous solution.

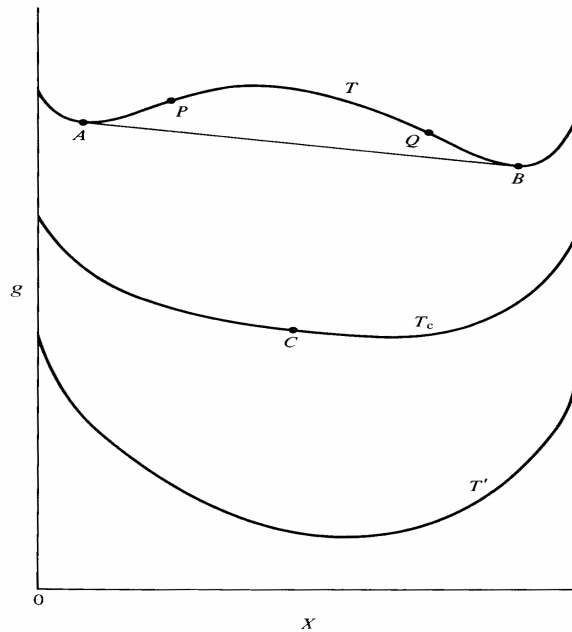


**Figure 2.9: Free energy versus composition of a system which exhibits a miscibility gap at low temperature ( $T < T_c < T'$ ) [67].**

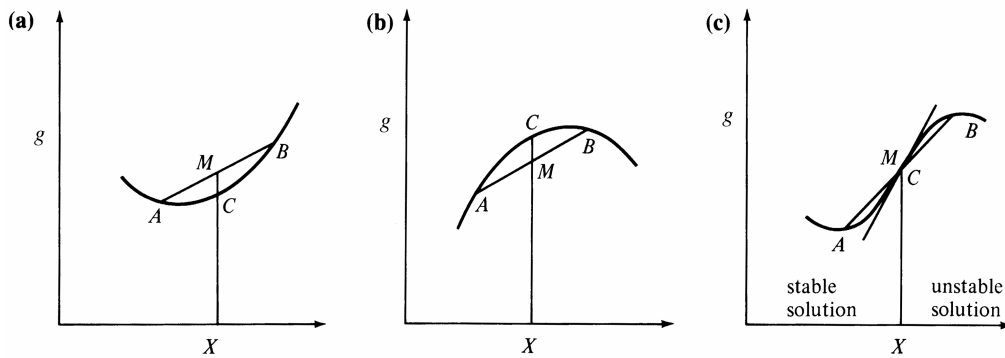


**Figure 2.10: Free energy versus composition for (a) a stable solution in which C has a lower free energy than the mixture of phases A and B with energy M, (b) an unstable solution where the mixture energy M is lower than homogenous solution energy C, and (c) the spinodal point which marks the transition [67].**

Figure 2.10 illustrates the possible free energy versus composition in a binary system. In Figure 2.10(a) the free energy curve is concaved upward. The free energy of the mixture, M, of phases A and B would be higher than the homogenous solution C. Therefore, the system is stable with respect to compositional fluctuations if,

$$\frac{\partial^2 G_m}{\partial X_2^2} > 0, \quad (2.1)$$

where  $G_m$  is the free energy of the mixture. On the other hand, if the free energy curve is concaved downward such as Figure 2.10(b), the mixture M has a lower energy than the solution C. Therefore, the system is unstable if,

$$\frac{\partial^2 G_m}{\partial X_2^2} < 0. \quad (2.2)$$

The inflection point, where

$$\frac{\partial^2 G_m}{\partial X_2^2} = 0, \quad (2.3)$$

as shown in Figure 2.10(c), is called the spinodal point and becomes the boundary between stability and instability. Compositions in which a solution is more stable as a mixture of phases undergo spinodal decomposition by segregating through composition fluctuations.

A general expression for the Gibbs free energy of a regular solution is defined as,

$$G_m = X_1 G_1^0 + X_2 G_2^0 + RT(X_1 \ln X_1 + X_2 \ln X_2) + \Omega X_1 X_2, \quad (2.4)$$

where  $X_1$  and  $X_2$  are the concentrations for components 1 and 2,  $G_1^0$  and  $G_2^0$  are the Gibbs free energy of the pure components 1 and 2,  $R$  is the gas constant,  $T$  is the temperature of the system, and  $\Omega$  is the interaction parameter for the two components in the solution. To determine the boundary of the miscibility gap, the first derivative of equation 2.4,

$$\frac{\partial G_m}{\partial X_2} = (G_2^0 - G_1^0) + RT(-\ln X_1 + \ln X_2) + \Omega(1 - 2X_2), \quad (2.5)$$

is taken. Taking the second derivative of equation 2.4, in order to determine the spinodal point, results in,

$$\frac{\partial^2 G_m}{\partial X_2^2} = RT \left( \frac{1}{X_1} + \frac{1}{X_2} \right) - 2\Omega. \quad (2.6)$$

By combining equations 2.3 and 2.6, the boundary of spinodal decomposition, as defined by the spinodal line, is given by:

$$X_1 X_2 = \frac{RT}{2\Omega}. \quad (2.7)$$

This line is a symmetric parabola around the midpoint of composition as shown in Figure 2.11. A more general case with asymmetric free energy dependence can also be derived yielding similar results [67]. The equation of the miscibility line, where the first derivative of the free energy becomes zero, is given by:

$$\ln \frac{X_2}{X_1} = \frac{\Omega}{RT} (X_2 - X_1). \quad (2.7)$$

For systems which exhibit very little solid solubility, such as the dilute nitride system,  $X_1 \ll 1$ . Therefore, equation (2.7) can be rewritten as

$$X_1 = \exp\left(-\frac{\Omega}{RT}\right). \quad (2.8)$$

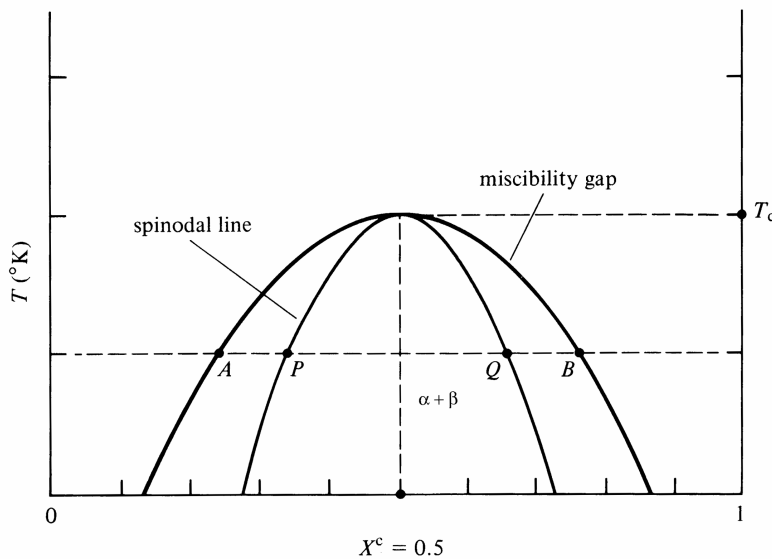


**Figure 2.11: A miscibility gap and a spinodal line for a regular solution [67].**

A regular solution can be modeled with simply the interaction parameter,  $\Omega$ , and the critical temperature for miscibility,  $T_c$ . For III-V materials, the delta lattice parameter (DLP) model can be used to calculate the interaction parameter based on the assumption that the bonding energy is related linearly to the bandgap, and the average

bandgap varies as  $a_0^{-2.5}$  (where  $a_0$  is the lattice parameter). The interaction parameter for III-V semiconductors then becomes [68]

$$\Omega = 4.375K \frac{\Delta^2}{\bar{a}^{4.5}}, \quad (2.9)$$

where  $K$  is a constant,  $\Delta=a_1-a_2$  or the lattice parameter difference of the components, and  $\bar{a}=(a_1+a_2)/2$  which is the average lattice parameter. The DLP model is actually very accurate since errors in the calculation of the component enthalpy cancel the error in the calculated alloy enthalpy [62]. The constant  $K$  in the equation can be determined from experimental data or from the valence force field (VFF) model. The VFF model assumes that the microscopic strain energy associated with the distortion of bonds in the alloy equals the enthalpy of mixing [64]. Table III lists the lattice mismatch and the interaction parameter derived from the DLP model for various III-V ternary alloys [69]. Using this calculation and the above data, the GaNAs alloy has a solubility of only  $10^{13}$   $\text{cm}^{-3}$  at temperatures even as high as  $800^\circ\text{C}$ . However, structural differences between GaAs and GaN are not factored into these equations and may influence solubility, particularly at higher concentrations. While the regular solution does have its shortcomings, it can be applied to give qualitative information about the stability of a system when mixing. In particular, it suggests that mixing a homogenous solution of GaN in GaAs with significant component quantities will be very challenging due to thermodynamic factors.

**Table III. Lattice mismatch and interaction parameter for nitride and indium based III-V ternary alloys [69].**

	Lattice mismatch $\Delta a/a$ [%]	Interaction parameter $W$ (DLP model) [kcal/mol]
<b>InGaAs</b>	7.2	2.815
<b>GaInP</b>	7.1	3.63
<b>GaNAs</b>	20	42.78
<b>GaNP</b>	18.9	28.90
<b>AlNAs</b>	22.3	57.93
<b>AlNP</b>	19.5	45.53
<b>InNAs</b>	17.3	26.71
<b>InNP</b>	14.6	19.68

### 2.3.7 Growth of homogeneous GaNAs

Despite the low predicted value of solid solubility of GaN in GaAs, homogeneous growth can occur at concentrations as high as 10%. It has been found that uniform material growth is highly dependent on growth temperature and the group-V vapor pressure [70]. It has been shown that this behavior can be modeled using traditional thermodynamic assumptions [71].

During the growth of GaNAs, two chemical reactions take place,



and



where the superscripts  $G$  and  $S$  refer to the gaseous and solid phases, respectively. The GaNAs alloy can be represented as a strictly regular solution. The equilibrium reaction constants are then calculated as a function of temperature and elemental partial pressures. For each reaction the chemical potentials must satisfy the following conditions,

$$m_{Ga}^G + \frac{1}{2}m_{As_2}^G \geq m_{GaAs}^S, \quad (2.12)$$

and

$$m_{Ga}^G + \frac{1}{2}m_N^G \geq m_{GaN}^S, \quad (2.13)$$

where  $m$  represents the chemical potential for each species. These equations can also be represented as,

$$p_{Ga}^G (p_{As_2}^G)^{1/2} \geq K_1 (1-x) \exp\left(\frac{\Omega x^2}{RT}\right), \quad (2.14)$$

and

$$p_{Ga}^G p_N^G \geq K_2 x \exp\left(\frac{\Omega(1-x)^2}{RT}\right), \quad (2.15)$$

where  $p^G$  represents the pressure of each species in the gaseous phase,  $K_1$  and  $K_2$  are the equilibrium constants of each reaction,  $x$  is the GaN fraction, and  $T$  is the temperature of the substrate. After solving these inequalities and determining values for the

constants [61], the results are graphed in Figure 2.12. The graph plots partial pressure of the Ga and As gaseous phases as a function of the substrate temperature. The line represents the boundary for different concentrations of GaN in GaAs between stable single phase material and decomposed two phase material. A box labeled “MBE Window” represents the typical partial pressures and substrate temperatures compatible with MBE growth of traditional III-V materials. This model predicts that the growth temperature needs to be sufficiently low and As partial pressure high in order to grow uniform single phase GaNAs. It can also be seen that the necessary temperature and vapor pressures are not a strong function of GaN concentration.

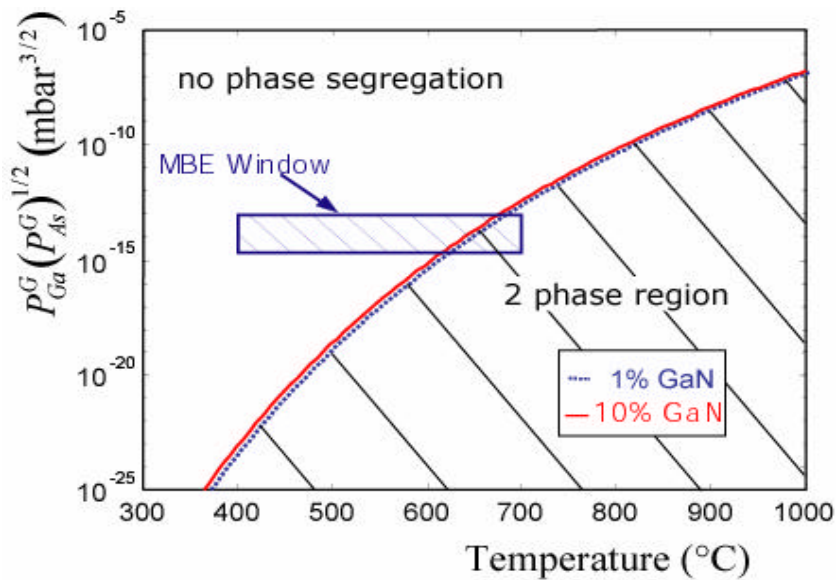


**Figure 2.12: Curves for different concentrations of GaN in GaAs representing the boundary between growth conditions which would produce segregated two-phase material and conditions under which a single phase is stable. The parameters partial pressure of Ga and As versus sample temperature were varied.**

### 2.3.8 MBE growth conditions for GaNAs

With a thermodynamic driving force for phase decomposition, and growth under metastable conditions, such as low substrate temperatures and high As vapor pressure, the growth of GaNAs is unlike other III-V alloy systems. In other traditional III-V systems, low substrate temperatures are used to prevent desorption which allows for better compositional control but are not required for phase stability. For instance,

InGaAs is commonly grown around 450°C, a temperature in which the In has unity sticking coefficient. However, with careful substrate temperature control for a well defined desorption rate, InGaAs can be grown hotter to produce better material quality. With dilute nitride GaNAs, on the other hand, at higher temperatures, the surface morphology becomes poor and in the wafer looks hazy. At high substrate temperatures, surface diffusion kinetics are fast enough that the material is able to segregate into two phases and the surface becomes very rough. A photograph of a GaNAs thin film grown too hot is shown in Figure 2.13, and an AFM surface scan of the same sample is shown in Figure 2.14. This two phase material grown at high substrate temperatures has very poor optical properties with almost no luminescence since the majority of the carriers recombine non-radiatively. Since GaNAs growth is very different than other III-V alloys, and its growth rate cannot be measured like other metal sources, the growth procedure for the growth of high quality material will be covered in the rest of this section. These steps are not the only way to calibrate nitride-arsenide growth, but can serve as a guide and can highlight potential difficulties unique to this material.



**Figure 2.13: Photograph of a wafer with a GaNAs thin film grown on the surface with a substrate temperature too high. The ring around the grown wafer was masked by the wafer holder and is representative of the original wafer surface finish.**

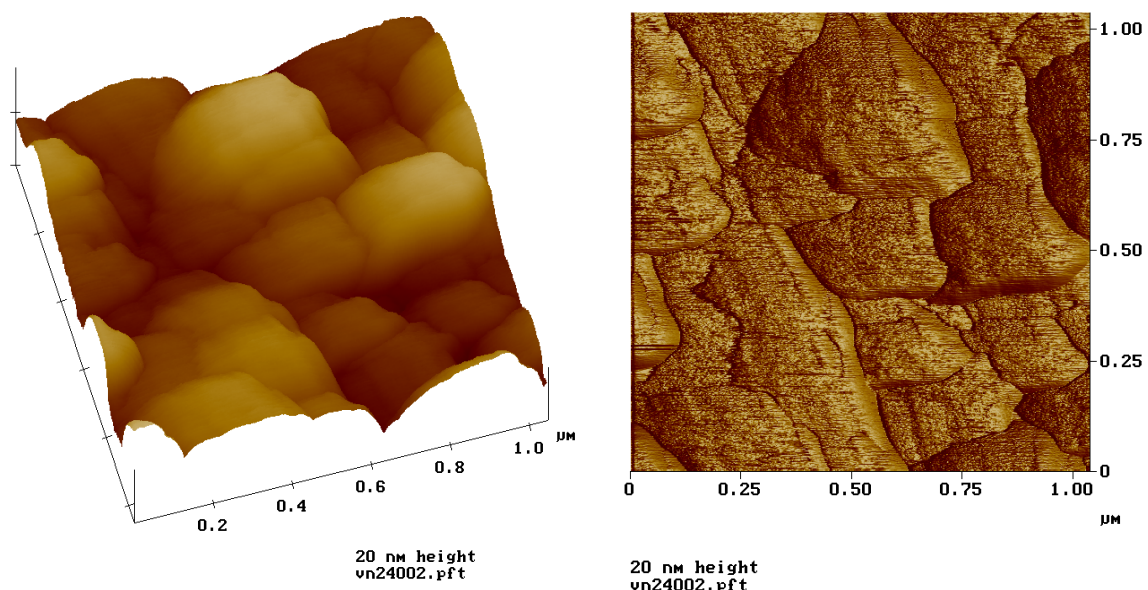


**Figure 2.14: AFM surface scan of the sample photographed in Figure 2.13.**

The first step for growing high quality GaNAs is the optimization of the RF plasma source as described in section 2.3.3. In practice, a plasma source for MBE should have few holes in the exit aperture to provide a high pressure inside the cell for a low ion plasma, but maintain low pressure inside the MBE growth chamber. The correct hole count, hole size, and N<sub>2</sub> flow rates are based empirically on the type of cell, power used, distance from the substrate, and many other factors which are certainly not well established. The initial calibration growth should be done using a stable plasma with a high growth rate of GaAs at around 160°C (200°C, as measured by the thermocouple) below the oxide blow off temperature (580°C). This ensures the film is grown with fairly dilute concentrations in the homogeneous growth regime. Measuring both bandgap absorption and XRD rocking curves can help calibrate alloy concentration. At these low temperatures, desorption should not be a problem and the N incorporation should follow an inversely proportional linear dependence with group-III growth rate. Next, PL samples can be grown as a function of growth temperature in order to optimize PL. Luminescence intensity should increase with increasing substrate temperature until a temperature is reached where decomposition occurs. This temperature can be quite a sharp transition and once the maximum temperature for

homogeneous growth is found, future growth for high quality material should be around 10 to 15 degrees below this value. Decomposed material can usually be quickly detected by eye. In grazing incidence with the surface under a UV lamp, the surface loses its mirror finish and looks gray or hazy. Sometimes only portions of the wafer are hazy, most commonly the center area where the substrate temperature is the hottest. The substrate temperature needed for homogenous material can be different for every system. It depends greatly on the plasma cell used and its characteristics. Changing the RF power, N<sub>2</sub> flow rate, exit aperture, and distance between plasma and substrate may all affect this temperature threshold.

## **2.4 GaInNAs(Sb) Growth**

Adding In to the GaNAs is fairly straightforward. The addition of In does not seem to affect the high temperature threshold for 2D growth of homogeneous material. The temperature necessary for nitride-arsenide growth is below the temperature at which In desorption is a problem. Therefore, during GaInNAs growth, In is assumed to have unity sticking coefficient at these temperatures and does not seem to be effected by the incorporating N. Since the amount of N added to GaAs is limited thermodynamically, for the longest possible wavelengths, In is added to the strain limit of the material. Indium is perfectly soluble in GaAs and phase decomposition is usually not a problem with the ternary. Instead dislocations and other deep level defects are common near the critical thickness strain limit which reduces the PL and quantum efficiency of InGaAs lasers in this material. The same issues should be relevant with GaInNAs near the strain limit.

Finally, the addition of Sb is also similar to other III-V materials. The Sb is sublimated, cracked and the beam flux is measured before growth. Calibration of Sb incorporation was done with XRD rocking curves of GaAsSb, and Rutherford backscattering spectroscopy (RBS). However, there currently is evidence that Sb does not have a unity sticking coefficient when mixed with N and In. This behavior will be covered in section 4.1.5. Other issues involved in Sb deposition were covered in section 2.2.1.2.

# Chapter 3: (Ga,In)(N,As,Sb) Optical Characterization

Optical measurements taken to better characterize bandgap and radiative efficiency will be covered in this chapter. The unique way N affects the bandgap of GaAs is first discussed in order to better understand the band structure of the N-As alloys. The theory behind luminescence and the measurements taken on GaInNAs is presented, particularly the improvement in radiative efficiency with thermal anneal is emphasized. A variety of luminescence measurements were taken, including, temperature dependent PL, cathodoluminescence (CL), and power dependent CL. Using the imaging mode and power dependence capability of CL, nonuniformity of GaInNAs layers was observed and studied in detail.

## 3.1 Nitrogen's Effect on the Bandgap of GaAs

It has been observed that by adding N to GaAs the bandgap does not follow a linear dependence between the binary compounds, also known as Vegard's law. Instead, there is an extremely large bandgap bowing towards lower energies [72], as seen in Figure 1.1. In fact, the bandgap drops much sharper in the dilute nitride regime than by adding equal concentrations of In. Many theories have arisen to explain the mechanism for this extreme bandgap bowing. Two theories have recently been popularized, both suggesting that dilute N does not alloy with GaAs in the traditional sense, but due to the large difference in atomic orbital energy and size between As and N, the N atom causes significant distortion in the electronic structure of the crystal.

The first theory states that N instead of alloying with GaAs contributes an impurity-like level to the band structure of GaAs similar to a dopant level. However, unlike a typical dopant, N does not contribute charge since it is isoelectronic with the crystal. Furthermore, instead of lying within the bandgap of GaAs, the N level exists

above the conduction band. There is then a strong interaction and anticrossing between the conduction band and the narrow resonant band formed by N states. There has been a great deal of experimental evidence of this resonant N level band anticrossing, and many theoretical models to support the theory [72-81].

A second theory has recently been suggested that explains the bandgap bowing differently. Instead, it is theorized that N distorts the GaAs lattice and can cause the normally indirect L valley in the band structure of GaAs to interact and mix with the  $\Gamma$  valley causing the conduction band to lower. The  $\Gamma$ -L intermixing also has a body of experimental and theoretical evidence to support it [82-84]. In particular, first principles local density approximation (LDA) theoretical calculations suggest a strong repulsion between  $\Gamma$ , X, and L levels occur in GaNAs without involving a N impurity level [85].

Both theories predict the correct behavior of the bandgap when adding N to GaAs and in fact, both the theoretically predicted and experimentally observed N resonant level is very close in energy to the L valley in GaAs. This suggests that no matter which theory of bandgap repulsion is eventually proven correct, the predicted effect on the GaAs bandgap will remain the same.

### **3.2 Luminescence of GaInNAs**

According to the bandgap versus lattice parameter dependence of GaInNAs, the quaternary alloy can have an arbitrarily small bandgap while remaining lattice-matched to GaAs. With current deposition technology, it is not yet possible to arbitrarily reduce the bandgap since there is a miscibility gap between GaN and GaAs that covers the majority of the alloy composition. This large region of decomposition limits the amount of N incorporation in GaAs while maintaining homogeneous material. Therefore to produce long wavelength material with high luminescent efficiency, the N content is limited to 5% or less, and In is added to the strain limit of the material. Even by limiting the N concentration to under a few percent, the GaInNAs alloy exhibits poor optical properties. It is not until the material is annealed after growth does the

luminescence efficiency improve, attaining a level which make it an attractive material for light emitting devices.

### 3.2.1 Introduction to luminescence in solids

Luminescence is the term used to describe the emission of radiation from a solid when it is supplied with energy [86]. The different types of luminescence are distinguished based on the method of excitation to create excess electron-hole pairs. For example, PL arises from the absorption of photons, cathodoluminescence (CL) is from bombardment with a beam of electrons, while electroluminescence (EL) results from the injection of carriers by application of an electric field (either AC or DC) across a *pn* junction. Whatever the form of energy input to the luminescent material, the desired final stage in the process is an electronic transition between two energy levels and resulting emission of a photon with an energy equal to this transition energy difference.

The system gains energy from the absorption process with the various types of pump sources. In PL, if the pump source energy is greater than the bandgap energy between valence and conduction band, the absorption of photons creates electrons in the conduction band and holes in the valence band that are higher in energy than at the bandgap minimum in order to conserve energy in the absorption process. Excited electrons and holes then quickly relax non-radiatively through interactions with phonons to lower energies in the conduction and valence band, respectively. Electrons at the bottom of the conduction band then recombine with a hole at the top of the valence band, either radiatively, giving off a photon, or non-radiatively, creating a large number of phonons and local heating. After a characteristic lifetime,  $\tau_{tot}$ , the system will return to the ground state; this process is shown schematically in Figure 3.1. The recombination time of the various transitions are related by,

$$\frac{1}{\tau_{tot}} = \frac{1}{\tau_{nr}} + \frac{1}{\tau_r} \quad (3.1)$$

where  $\tau_{nr}$  is the non-radiative lifetime and  $\tau_r$  is the radiative lifetime. For a direct bandgap semiconductor, like GaAs, the absolute minimum in the conduction band is aligned in momentum, or k-space, with the maximum in the valence band. Here a

transition between an electron in the conduction band and a hole in the valence band can occur with little momentum change, or simply with the emission of a photon. For an indirect gap material, such as Si, when the electrons are at the minimum in the conduction band they need to change in momentum to transition to the valence band maximum. This can only take place in a second order process by interacting with a phonon, thus drastically reducing radiative efficiency. Radiative recombination in bulk semiconductors occurs predominantly via three different processes, interband transitions, recombination via impurity centers and exciton recombination.

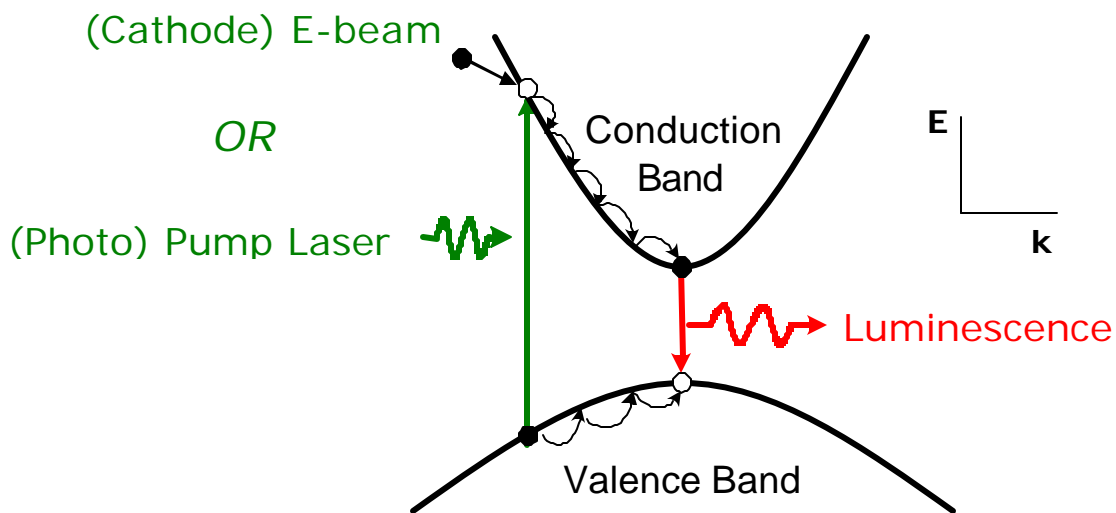


Figure 3.1: Schematic of the PL/CL process in a direct bandgap material.

Interband transitions occur between bands such as the conduction and valence band both in direct and indirect gap material. A transition must conserve the total wave vector of the system. The photon wave vector is given by  $2\pi/\lambda$ , while the electron wave vectors can be anywhere between the first Brillouin zone boundaries, between  $-\pi/a$  and  $+\pi/a$ , where  $a$  is the crystal lattice spacing. For visible radiation,  $\lambda$  is approximately  $5 \times 10^{-5}$  m while the crystal lattice spacing is around  $10^{-10}$  m, hence  $2\pi/\lambda \ll \pi/a$ . The photon wave vector is thus orders of magnitude smaller than the possible electron wave vectors. Consequently, if the only particles involved are an electron and a photon, then the electron must make a transition between initial and final states having virtually the same wave vector. On an E-k diagram, therefore, only vertical transitions are allowed.

It is possible to have non-vertical transitions, such as in an indirect bandgap system. But to conserve the wave vector, a phonon must either be created or destroyed simultaneously. However, because now three particles are involved instead of just two for the indirect transition process, the transition is much less probable. The following expression defines the spontaneous radiative recombination rate following a quantum mechanical derivation [87]:

$$R = \frac{ne^2}{m_0^2 c^3 \hbar^2} M^2 \left[ \frac{2k_B T}{p \hbar^2} \right]^{3/2} \sqrt{\mathbf{m}_x \mathbf{m}_y \mathbf{m}_z} E_g \left[ 1 + \frac{3k_B T}{2E_g} \right] e^{-E_g / k_B T}, \quad (3.2)$$

where  $n$  is the refractive index,  $m_0$  is the free electron mass. The term  $\mathbf{m}_x$  is the reduced carrier mass in the  $x$  direction, defined as

$$\frac{1}{\mathbf{m}_x} = \left( \frac{1}{m_{e,x}} \right) + \left( \frac{1}{m_{e,h}} \right), \quad (3.3)$$

with similar terms for  $y$  and  $z$ . The expression for  $M$  can be written as

$$M^2 = \frac{1}{4\mathbf{p}} \sum_{l=1}^2 \int d\Omega_k |e_{kl} P_{cv}|^2, \quad (3.4)$$

where  $e_{kl}$  is the polarization direction of the photon with the momentum  $k$ , the sum is over two polarizations, the averaging is over all photon momentum directions, and  $P_{cv}$  is the interband transition matrix element at the  $\Gamma$  point of the Brillouin zone. The interband radiative recombination coefficient can be defined according the equality

$$R = Bnp, \quad (3.5)$$

where  $B$  is a constant and  $n$  and  $p$  are carrier concentrations. Joining equations,  $B$  can be rewritten as

$$B = \frac{ne^2}{m_0^2 c^3 \hbar^2} M^2 \left[ \frac{2p \hbar^2}{k_B T} \right]^{3/2} \frac{1}{(\bar{m}_x \bar{m}_y \bar{m}_z)^{1/2}} E_g(T) \left[ 1 + \frac{3k_B T}{2E_g(T)} \right], \quad (3.6)$$

where,

$$\bar{m}_x = m_{e,x} + m_{h,x}, \quad (3.7)$$

with similar equations for the  $y$  and  $z$  terms. Calculated values for  $B$  in indirect bandgap materials are around 100 times smaller than for direct bandgap materials. Therefore band-to-band radiative transitions for indirect bandgap semiconductors are relatively rare and are much more likely for direct bandgap materials.

Interband transitions occur at bandgap energies or above, however, less than bandgap transitions are possible. One type of less than bandgap recombination occurs via impurity centers for which three types of recombination involving either initial or final state electron energies associated with the impurity energy levels. These include conduction band-acceptor level transitions, donor level-valence band transitions and if a pair of donors and acceptors is physically close together, then donor-acceptor transitions are possible. In material with even no defects, less than bandgap transitions are possible since exciton states exist within the energy gaps. Excitonic states can be visualized as Bohr-like states in which an electron and hole are bound Coulombically and have a common center of mass. The electron and hole are relatively weakly bound and the exciton states are situated just below the bottom of the conduction band and above the valence band, with binding energies that are small compared to most bandgaps (~10 meV).

### **3.2.2 Improving photoluminescence of GaInNAs by annealing**

A schematic of the PL system used for room temperature PL measurements is shown in Figure 3.2. An Ar ion laser with a wavelength of 514.5 nm was used as a pump source. The pump power incident on the samples was fixed at 250 mW and kept constant for all samples in order to better compare data between samples. Standard lock-in techniques were used to improve the signal to noise ratio by chopping the incident beam and feeding the output signal to a lock-in amplifier. A ½ meter SPEX spectrometer and an InGaAs photodiode measured the optical spectrum. A slit size of 3 mm and a grating blazed at 1200 nm was used for all measurements. Before the samples were measured, the white light system response was taken for the spectrometer and optics. This background response was used to normalize measurements in order to better compare intensities and spectral features over a broad wavelength range. In order to calibrate intensity, a standard PL sample of GaAs quantum wells with AlGaAs barriers was first measured. A HeNe laser with a known wavelength of 632.8 nm was sent through the spectrometer to calibrate the grating angle. Absorption of the laser and surface recombination can drastically change luminescence efficiency, so the distance between the quantum wells and the surface was kept the same and a large bandgap

AlGaAs cap layer was grown to inhibit surface recombination. A drawing of the standard PL sample structure used to compare material quality is shown in Figure 3.3. The AlGaAs cap and thickness are always kept the same and only the active region, barriers, and number of quantum wells is changed between samples. In the future an AlGaAs diffusion barrier would not be necessary since it can complicate other material analysis of these samples.

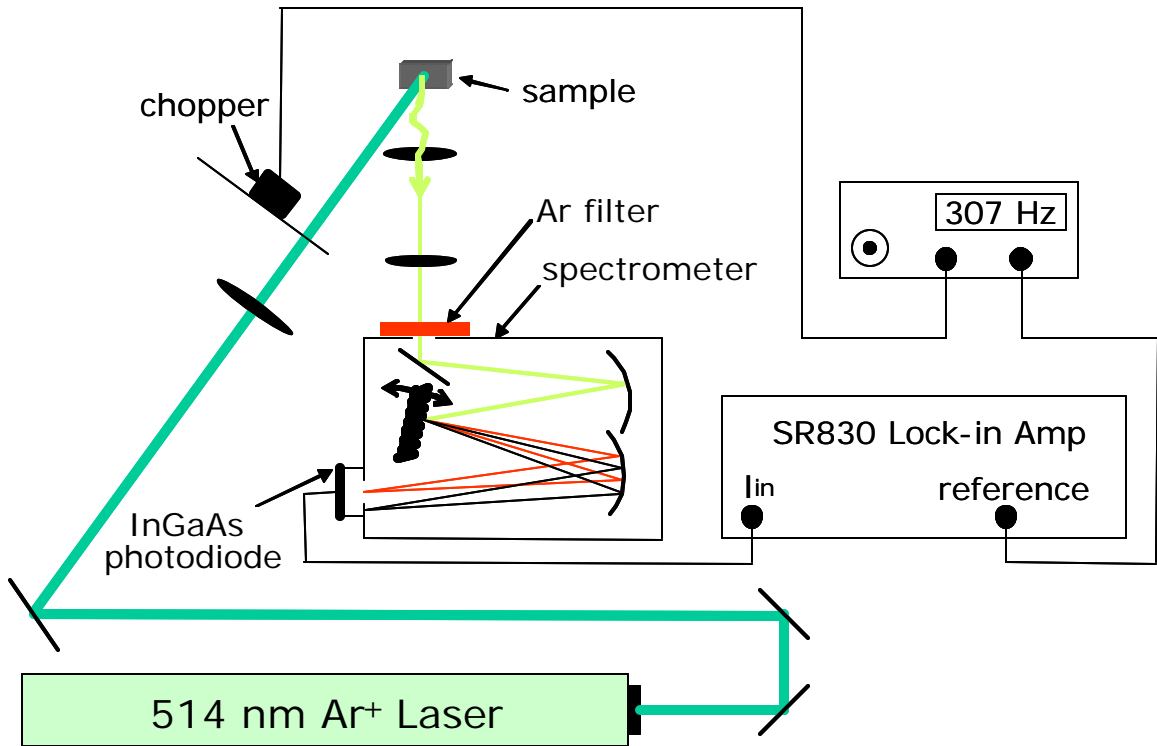
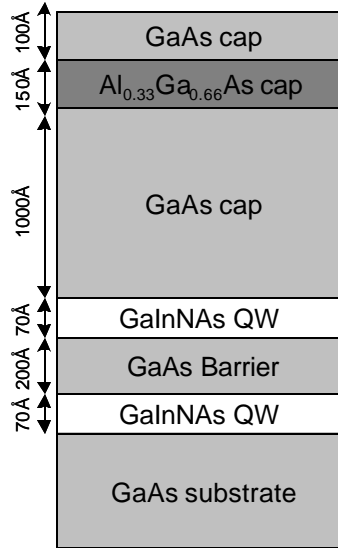


Figure 3.2: PL setup used for room temperature measurements.



**Figure 3.3: Standard PL sample layer structure with AlGaAs cap.**

The spectral output of a typical GaInNAs PL sample is shown in Figure 3.4. The peak labeled “as grown” is the sample measured directly after being grown. The intensity is very low, and would not be very useful in a device application due to poor radiative recombination efficiency. The wafer was then cleaved into many pieces, and using an AG heatpulse 310 annealer, the same samples were rapid thermal annealed (RTA) at different times and temperatures. The PL from samples annealed at three different temperatures, all at one minute are also plotted in Figure 3.4. Several observations can be seen in the thermal anneal behavior. First is that the peak intensity rises with increasing anneal temperature and then drops above a certain temperature as shown in Figure 3.5. Second, the full width at half maximum (FWHM) decreases with increasing annealing temperature. This is an indication that the material quality is improving with the thermal treatment and non-radiative centers, such as deep level defects, are being removed from the sample. Typical improvements in peak intensity are between 50-100 times in some samples. The third evident feature of the annealing behavior of GaInNAs is that with increasing temperature, the PL shifts to shorter wavelengths or larger energies. This is evidence of a shift in bandgap energies of the material with increasing anneal temperatures. Unfortunately the shift is always to shorter wavelength while for device applications, longer wavelengths are desirable.

The concentration of N is limited by the miscibility gap, and In is limited due to critical thickness concerns, therefore, the blueshift on anneal increases the difficulty of making an alloy of GaInNAs with the desired longer wavelengths. The origin of the intensity improvement and the blueshift of the PL wavelength will be covered in further detail in future sections.

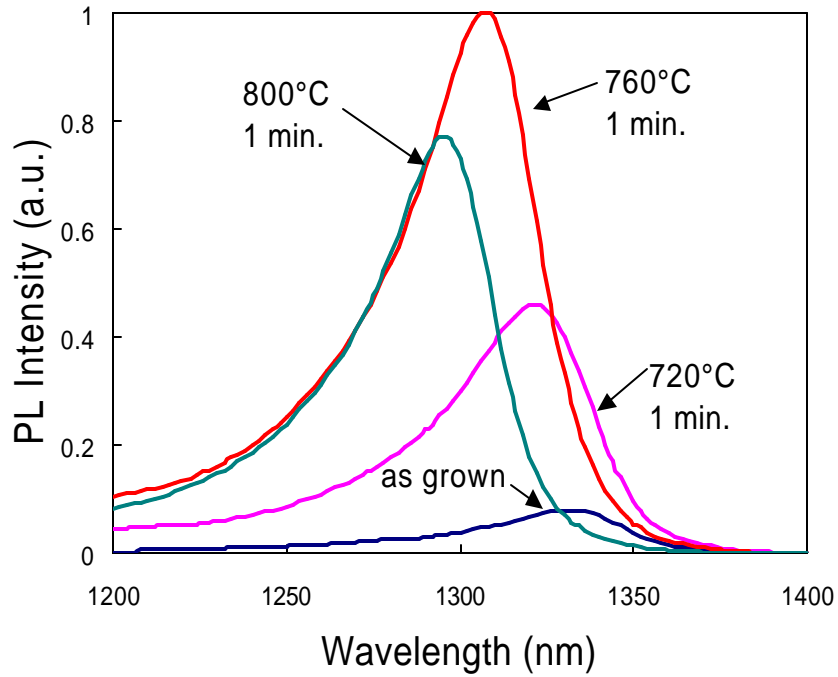


**Figure 3.4: PL of GaInNAs with 30% In and 1.5% N comparing as-grown material with RTA material at different temperatures.**

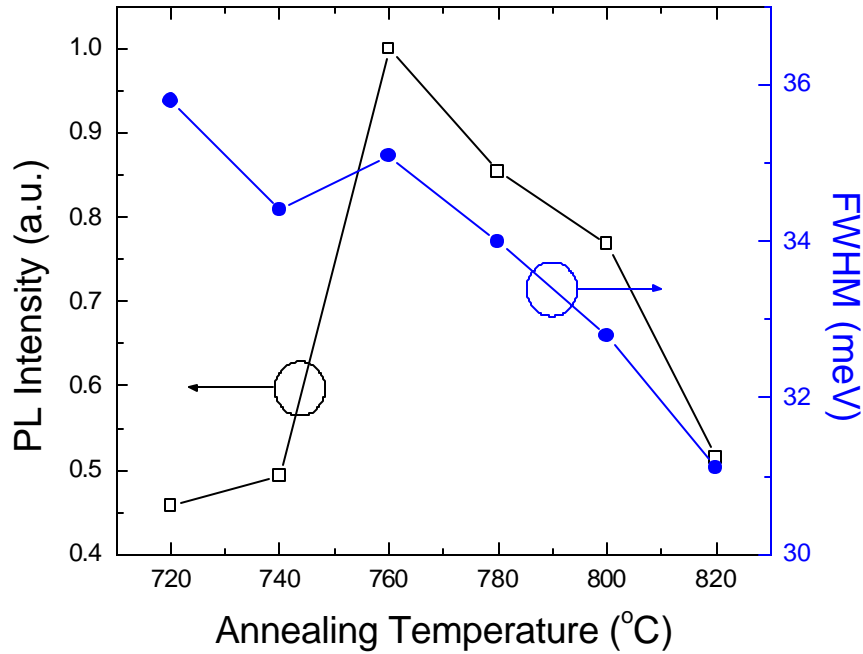


**Figure 3.5: PL intensity and full width half maximum for the PL sample of Figure 3.4.**

### 3.2.3 Optimizing the photoluminescence of GaInNAs

Compared to a 1.1  $\mu\text{m}$  InGaAs quantum well sample, the PL intensity of a GaInNAs active material sample at 1.3  $\mu\text{m}$  is typically 5-10 times lower. The best long wavelength devices made with GaInNAs are usually inferior to similar shorter wavelength InGaAs devices. Either through the process of depositing the N or inherent in the alloy itself, the material contains a high density of non-radiative recombination centers. Many steps were taken in both MBE growth and subsequent annealing to improve PL and reduce the defects present in the material. Since PL is greatly affected by anneal time and temperature, optimizing the RTA process was the first step in improving material quality. For each growth, samples were annealed for at least eight different times and temperatures. It was found that growth conditions, such as substrate temperature, number, and thickness of quantum wells, In and N composition, and plasma properties all change the ideal thermal treatment. For example, more quantum wells increases the ideal anneal temperature from 760°C for one minute for a single quantum well to 820°C for three minutes for a three quantum well sample.

Many other factors were considered with regard to improving PL intensity, including growth temperature, As over-pressure, plasma conditions, quantum well structure and alloy composition. Substrate temperature during GaInNAs growth plays the most important role in PL intensity since temperature controls both the likelihood of phase segregation and the incorporation of deep level defects. With a temperature that is too high, the material phase segregates and the surface morphology becomes very rough. Consequently, the PL intensity can fall off by orders of magnitude. With a temperatures that is too low, the material incorporates too many defects typical of low growth temperatures and the PL efficiency also decreases quite significantly though not as rapidly as with too high growth temperatures.

Another growth parameter, the group V-V As-N ratio, was changed by modifying the As overpressure. Relatively high group-V overpressures are common for GaAs and InGaAs, however, very low group-V overpressures are beneficial in GaN growth since Ga rich conditions help smooth the surface of the substrate. It is thus not immediately clear which of these conditions might be best in the case for GaInNAs growth, since GaNAs is grown under metastable conditions and increasing mobility of the group-III components under metal rich conditions may increase the kinetics towards phase segregation. It was found from the PL data that reducing the As overpressure only served to slightly reduce PL intensity, unlike the improvement seen in GaN grown under Ga rich conditions.

Plasma conditions were also optimized in order to improve PL efficiency. Accelerated species from the plasma, such as ions, are known to damage III-V materials and could increase the deep level defects in the material. Two ion deflection plates were placed at the exit aperture of the plasma source and biased at high voltages in order to deflect the charged ions. However, with proper plasma cell operation, charged ions leaving the cell appeared to be low and, consequently, little change in PL peak intensity was found by using the deflection plates. Other operating parameters of the plasma cell, such as RF power, aperture hole count, and flow rate, have an effect on the PL intensity. At this stage, only a limited range of RF power and flow rates were investigated and only two apertures were changed to optimize the plasma with respect to the PL. In the future, further optimization would be possible by putting an isolation

valve between the MBE chamber and the N plasma source. Because of the 1-3 week down-time involved when opening the MBE chamber, only two apertures were investigated during the two plus years of this research. Incorporating an isolation valve on the N source would enable far more experiments in this parameter space of the N source.

While increasing the N content has a negative effect on PL, the volume of N containing material also has a major influence on PL intensity. Structures with a larger volume of N containing layers show signs of reduced luminescence efficiency and higher temperature anneal requirements. Using N in the barriers around the quantum wells seems to reduce PL intensity, and single quantum wells generally have higher PL than multiple quantum wells. After about three quantum wells, the PL intensity then increases with an increasing number of quantum wells if strain compensating GaNAs barriers are used. However, it is common when pumping quantum wells with a pump energy greater than barrier layer bandgap, as in these measurements, the luminescence from multiple quantum wells does not scale with a linear relationship. This is because the majority of the absorbed carriers recombine in the barriers or at the surface and not in the wells. Using a pump source energy between the quantum wells and barriers allows for a more accurate measure of quantum well scaling, but such a source was not available.

For a given wavelength, the ratio of In to N concentration in the alloy can greatly effect the quality of the material. It is assumed that the addition of N contributes most of the defects, therefore, at shorter wavelengths a higher In to N ratio is desired to minimize defects. But as the In content increases in the film, strain becomes a problem and dislocation density increases. For longer wavelengths, more N then has to be added or a strain compensated structure can be used. Even at the optimal In/N ratio in longer wavelength material, optical properties, such as PL intensity, and device performance, such as threshold current density, rapidly degrade proportionally to bandgap in material from 1.2  $\mu\text{m}$  to around 1.5  $\mu\text{m}$ . Material past 1.5  $\mu\text{m}$  typically contains too many defects and even after annealing shows no detectable PL. To push to longer wavelengths, new strain compensating structures, better plasma deposition, or a new alloy needs to be developed to reach the desirable wavelength of 1.55  $\mu\text{m}$ .

### 3.3 Photoluminescence of GaInNAsSb

At wavelengths beyond 1.3  $\mu\text{m}$ , the PL of GaInNAs generally decays very rapidly with increases in either In or N; this can be either due to non-radiative relaxation processes or phase separation of N or In. In other alloy systems grown under metastable growth conditions, surfactants have been shown to improve incorporation and sticking of depositing species. In systems such as SiGe [88], GaInP [89], and high indium InGaAs [90], the surfactants Te, Bi, and Sb have been used to reduce the surface energy of the substrate and facilitate incorporation and wetting of the immiscible component. The large surfactant atom sits on the surface and modifies the surface tension of the substrate. An adatom of a depositing component can then wet the surface, exchange sites with the surfactant, and bond in a lattice site. Surfactant growth has been suggested in order to improve the incorporation of N and reduce surface segregation [7,8,91-94]—the most likely mechanism for phase segregation. By using Sb in this work, 2-D growth was maintained in material with higher In and N compositions than previously possible and samples showed high-intensity luminescence at wavelengths longer than 1.5  $\mu\text{m}$ . Figure 3.6 illustrates the effect of adding Sb to GaInNAs at concentrations of In which normally produce very low PL intensities. Figure 3.6(a) shows the brightest single quantum well GaInNAs PL sample grown thus far (intensity is normalized to one). Increasing the In to 35% while fixing the N content, the luminescence intensity drops off by over three orders of magnitude (Figure 3.6(b)). However, with the same N content, adding even more In, but also adding Sb in increasing amounts (Figure 3.6(c-e)), the PL efficiency is recovered, approaching the level of the best 1.3  $\mu\text{m}$  GaInNAs material but at wavelengths as long as 1.6  $\mu\text{m}$ . In fact, the 1.5  $\mu\text{m}$  sample, Figure 3.6(d) has a peak PL intensity of over 50% the peak intensity of the best 1.3  $\mu\text{m}$  sample, Figure 3.6(a).

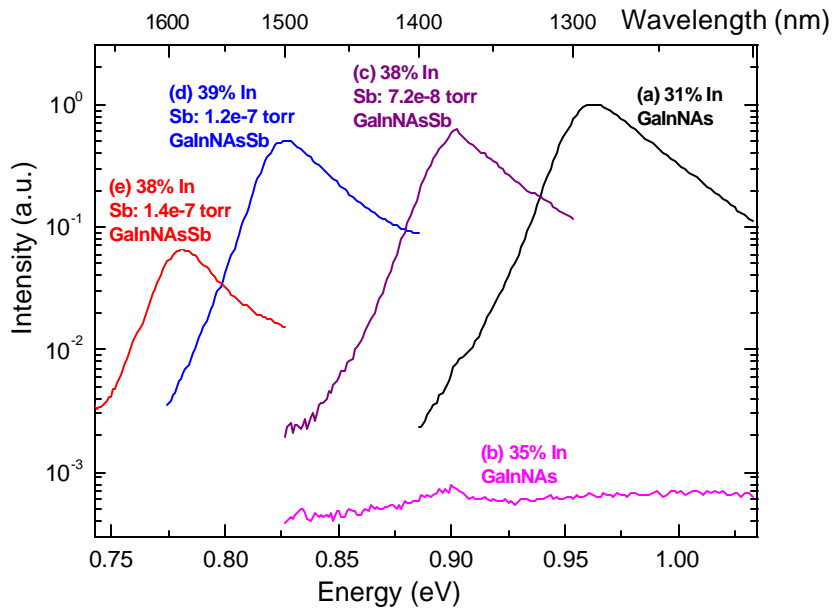


**Figure 3.6: Background subtracted PL results from 2 GaInNAs/GaNAs samples and 3 GaInNAsSb/GaNAsSb single QW samples. Intended N content remained fixed at 1.2%.**

In previous studies, Sb was only thought of to act as a surfactant in GaAs. However, with further investigation, we found that it incorporates into the alloy at levels as high as 10% in nitride-arsenide materials. Therefore, in the new alloy of GaInNAsSb, the Sb is actually present at levels above the N, as shown in the SIMS profile data in Figure 3.7. As an alloy component the addition of Sb at first glance does not seem like a major improvement to the alloy. Figure 3.8 shows the lattice constant versus bandgap for GaAsSb alloys. From the plot, it is observed that adding Sb contributes less to bandgap reduction than In and has an increase lattice mismatch to GaAs. However, the most important effect of adding Sb is the ability to maintain 2-D growth with higher N and In compositions. Furthermore, by adding Sb, a small N increase of about 10% was observed [95]. This result suggests that by changing the surface properties, lower energy N radicals may incorporate more efficiently as substitutional atoms, thus increasing the incorporation rate. This observation is somewhat incongruous with the idea of N having unity sticking coefficient, however, it is believed that the range of N radicals which incorporate do not readily desorb.

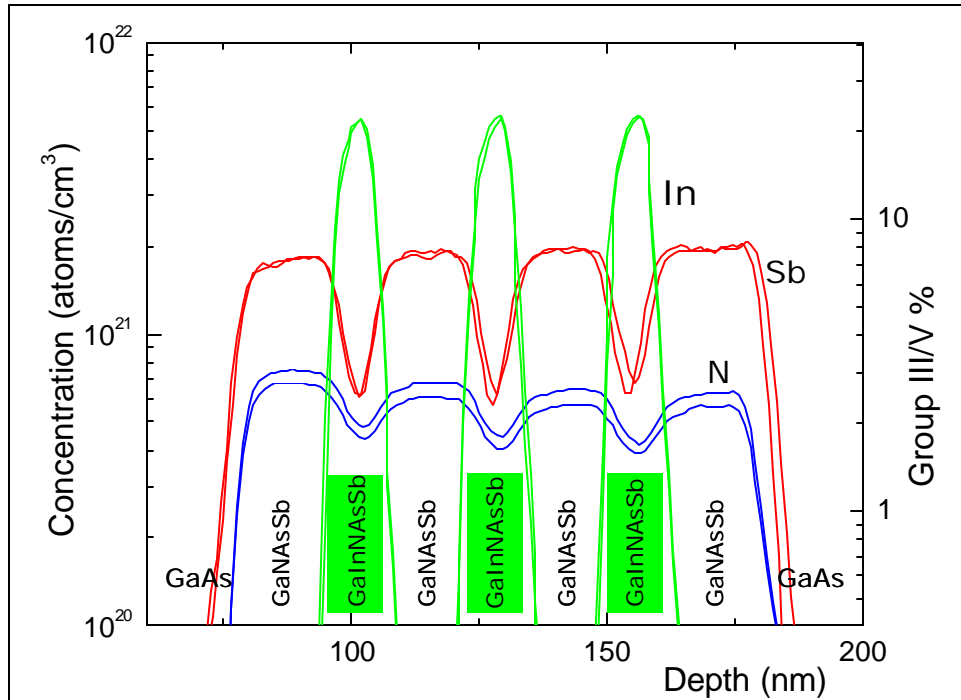


Figure 3.7: SIMS profile of In, Sb and N before and after the RTA process. The structure consisted of 3 GaInNAsSb QW's between GaNAsSb barriers. The In and Sb profiles were not significantly changed by the thermal process while annealing reduced the N concentration in barrier and QW.

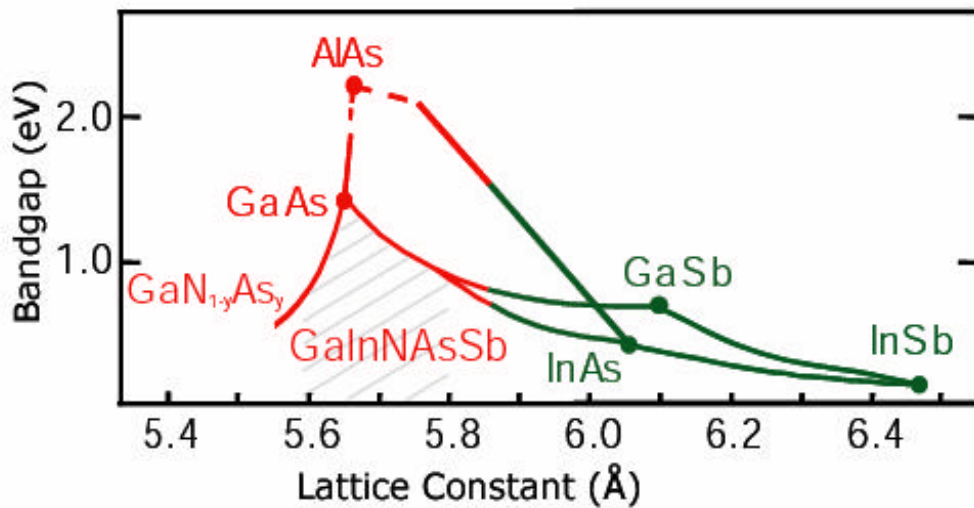
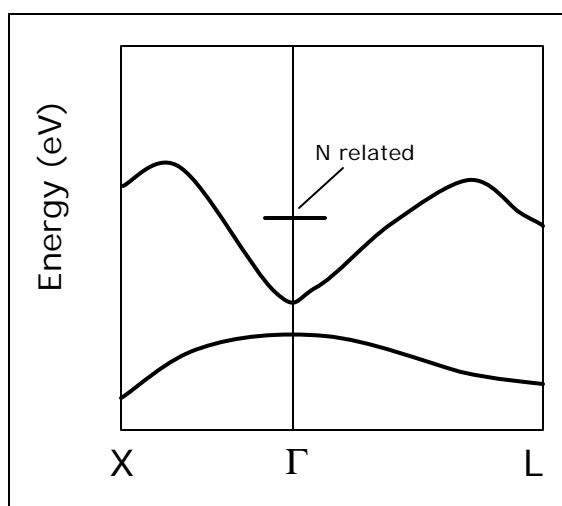


Figure 3.8: Lattice constant versus bandgap for III-V alloys relevant to GaInNAsSb.

One notable and surprising behavior of adding Sb to GaInNAs is the strong redshift of the PL by adding small amounts of additional Sb, as seen in Figure 3.6.

While it was found that Sb slightly increases the N concentration in the alloy, the additional Sb and N alone do not account for the wavelength shift from about 1.4 to 1.6  $\mu\text{m}$  in luminescence. One explanation could be that Sb effects the band structure of GaInNAs and increases the effect other components, particularly N, have on the bandgap. To better illustrate this concept, a band diagram for GaNAs with the N related level is shown in Figure 3.9. The addition of In is known to significantly decrease the conduction band, creating a large conduction band offset with respect to GaAs. Since the N related level may be fixed in energy to the L valley, lowering the conduction band may reduce the anticrossing interaction between the N level and the  $\Gamma$  valley, reducing the effect of N addition on the bandgap for increasing In composition InGaAs alloys. On the other hand, Sb is known to shift the valence band, increasing the large valence band offset with GaAs, and in fact decreasing the L and X conduction band minima at high concentration, since GaAsSb has a type-II band offset with the conduction band. Therefore, adding Sb to GaNAs may in fact increase the anticrossing interaction between the N level and the  $\Gamma$  conduction band minimum, enhancing the effect of N on the bandgap of GaAs. In the binary compounds the  $\Gamma$  to L valley separation is 0.296 eV in GaAs, 0.716 eV in InAs, and 0.063 eV in GaSb [65]. As a result, small additions of Sb in GaNAs may play a greater role in bandgap reduction than originally expected.



**Figure 3.9: An illustration of the conduction and valence and N related energy levels of GaInNAs in k-space.**

### 3.4 Temperature Dependent Photoluminescence

By changing the sample temperature while measuring PL, new information can be gained about a material. To derive the temperature dependence of the radiative recombination rate, an important parameter is the dependence of bandgap energy with temperature of the material. In many semiconductors, the empirical Varshni formula [96] approximates the observed temperature dependence of the band gap:

$$E_g(T) = E_g(0) - \frac{gT^2}{T + b}, \quad (3.8)$$

where  $E_g(0)$  is the bandgap energy at 0 K, and  $g$  and  $b$  are constants for a given material, where  $b$  is proportional to the Debye temperature. The relationship is based on a  $T^2$  energy dependence below the Debye temperature and a  $T$  energy dependence above the Debye temperature. Alternatively, a more physical expression can be used to describe the temperature dependence of the interband transition in which the energy threshold decrease proportionally to the Bose-Einstein statistical factor for phonon emission plus absorption [97]:

$$E_g(T) = a - b \left( 1 + \frac{2}{e^{\frac{\Theta_B}{T}} - 1} \right), \quad (3.9)$$

where  $(a-b)$  is the bandgap energy at 0 K, and  $b$  represents the strength of the exciton-average phonon interaction, and  $\Theta_B$  is the average frequency of both the acoustic and optical phonons. The temperature dependence of the linewidth of the interband transitions in semiconductors can be expressed as:

$$\Gamma(T) = \Gamma(0) + \frac{\Gamma_{ep}}{e^{\Theta_{LO}/T} - 1}, \quad (3.10)$$

where  $\Gamma(0)$  represents the broadening due to temperature independent mechanisms, such as impurities, dislocations, and surface scattering, and  $\Gamma_{ep}$  is the strength of the exciton-LO phonon coupling, and  $\Theta_{LO}$  is the average frequency of the longitudinal optical phonons since optical phonons are the main contributors to the linewidth broadening.

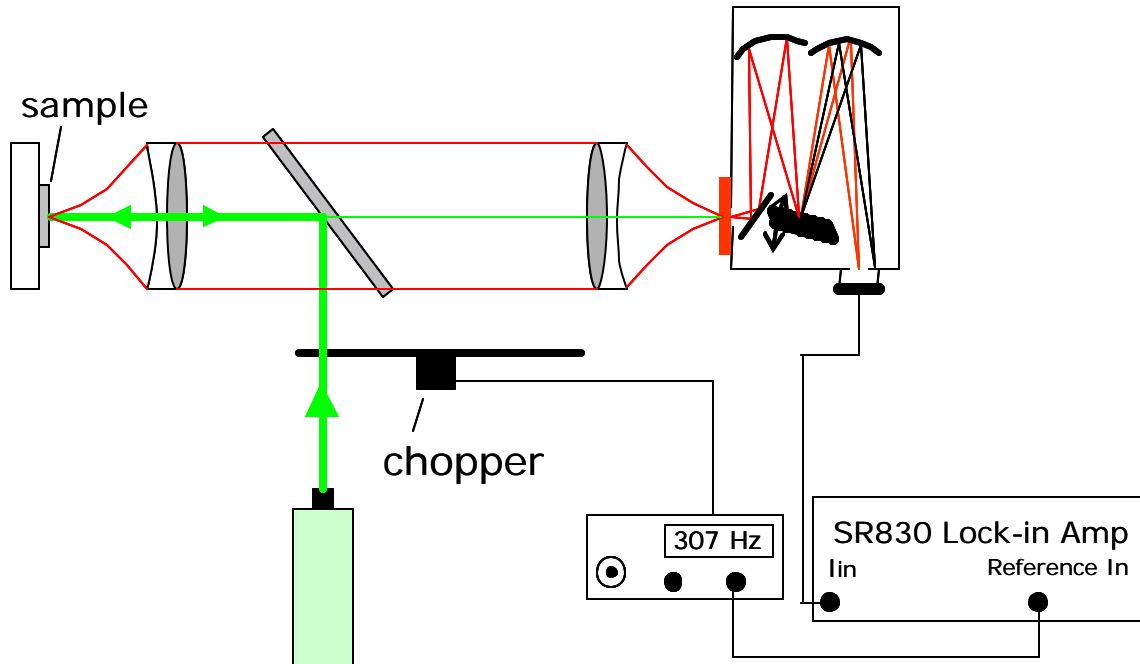


**Figure 3.10: PL setup for low temperature measurements.**

In order to measure the temperature dependence, the PL samples were cooled using a continuous flow liquid He cryostat which was pumped down to below 1 mTorr for thermal isolation. The PL setup used to make measurements at low temperature is shown in Figure 3.10. An Acton Research SpectraPro spectrometer was used to measure the spectrum with standard lock-in techniques using an InGaAs photodetector and 450  $\mu\text{m}$  slit openings. An  $\text{Ar}^+$  laser was used as a pump source at 80 mW incident power. The temperature dependent PL data from 15 K to room temperature of a 70  $\text{\AA}$  single GaInNAs quantum well sample with 30% In and 1.2% N annealed at 760 $^\circ\text{C}$  for 1 minute is shown in Figure 3.11. The most notable features of the data are that the spectra both redshifts and decreases in intensity with increasing temperature. This is normal and can be readily explained from the temperature dependent luminescence of direct gap semiconductors. The PL redshift comes from the reduction of bandgap with increasing temperature. The bandgap decreases with temperature since at higher temperature, through thermal expansion, the lattice constant of the material becomes larger and in general the larger the interatomic distances, the smaller the bandgap. This is shown schematically in Figure 3.12. The PL intensity increases with decrease temperature because the non-radiative recombination rate decreases with decreasing

temperature because the carrier diffusion length decreases. A summary of the data for this sample and a GaInNAsSb sample which exhibited 1.45  $\mu\text{m}$  room temperature PL is shown in Figure 3.13. For comparison, GaAs data from an empirical data fit from Varshni fit [98] is also shown in Figure 3.13. While each sample has a different bandgap, the data was plotted as energy shift for comparison sake. It was found that the PL of both GaInNAs and GaInNAsSb have a lower temperature dependence than GaAs. This is different from the characteristic temperature,  $T_0$ , defined in section 1.3.3, as that is more a device parameter based primarily on quantum well confinement of electron and holes. The data measured here is a material property based purely on bandgap changes with temperature. The decreased bandgap temperature dependence is further evidence of the desirability of this material in devices applications. A summary of the Varshni fitting parameters of equation 3.8 is shown in Table IV.

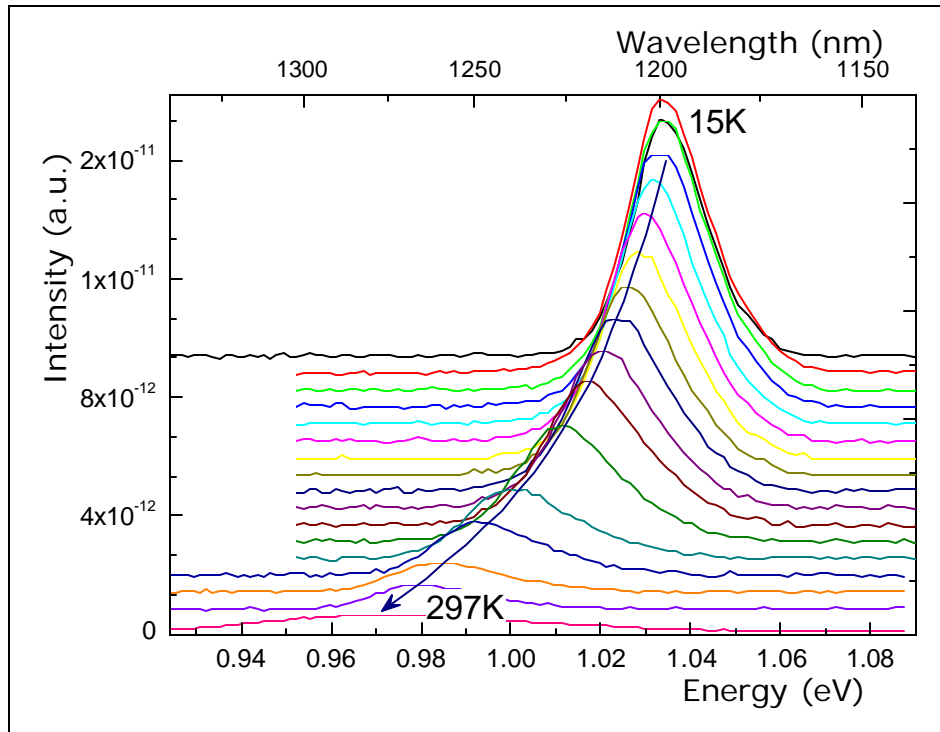


**Figure 3.11: Temperature dependent PL from 15 K to 297 K of a single 70 Å QW 30% In, 1.2% N GaInNAs sample annealed at 760°C for 1 minute.**

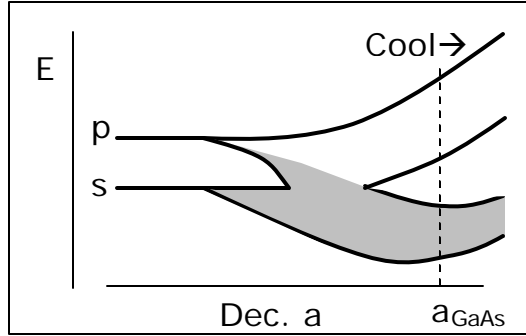


**Figure 3.12: Schematic of the atomic energy levels versus decreasing lattice parameter (a). This illustration can be used as a guide to understand why the bandgap increases as temperatures decrease.**

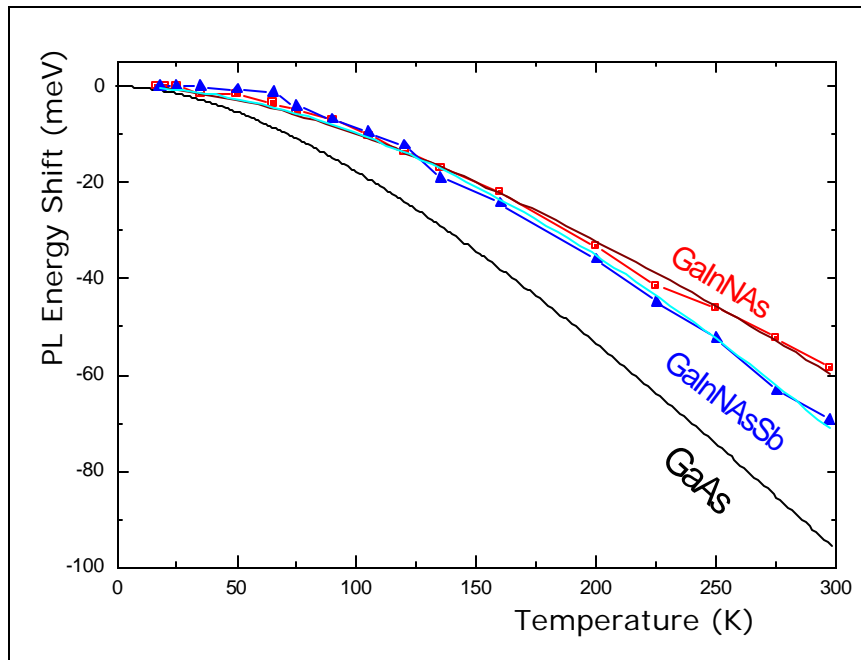


**Figure 3.13: Normalized PL energy shift versus sample temperature for GaAs, GaInNAs and GaInNAsSb. GaAs data based on Varshni fit of tabulated data, GaInNAs data is from the measurement in Figure 3.11, and GaInNAsSb is a 1.45 mm RT PL sample of 90 Å single QW with 39% In, 1.2% N and an Sb beam flux of  $8.38 \times 10^{-8}$  Torr.**

**Table IV. The Varshni fitting parameters for GaAs, GaN, GaInNAs, GaInNAsSb. GaAs [98] and GaN [99] values taken from literature while GaInNAs and GaInNAsSb were both measured.**

	g [meV/K]	b [K]
GaAs	0.5408	204
GaN	0.939	722
GaInNAs	0.414	315
GaInNAsSb	0.913	834

From the dependence of PL energy with temperature, one can gain insight into the mechanisms for spontaneous emission. At low temperature in some inhomogeneous material with phase segregation or quantum dots, carriers can be locally confined in regions of lower energy fluctuations in the bandgap. As the temperature increases the carriers are thermally excited out of the localized levels in the material into delocalized higher bandgap regions. If this localization exists in the sample, the PL energy versus temperature dependence shows an s-shaped behavior. The bandgap begins to shrink at low temperatures, but at intermediate temperatures, the apparent bandgap quickly increases due to this local excitation of carriers, and then continues to decrease again at even higher temperatures. The material measured here did not exhibit this behavior. Therefore it can be concluded that for these samples, there is no observable localized recombination in annealed GaInNAs and GaInNAsSb.

### 3.5 Cathodoluminescence of GaInNAs

The emission process in CL is the same as that for PL, however the excitation source is a high energy electron beam rather than incident photons. When a beam of energetic electrons of energies above around 1 keV hits a solid, a fraction about 10% backscatters from the surface while the remainder penetrates into the solid. As they travel into the material they rapidly lose energy, mainly by impact ionization generating electron hole pairs as they travel. Eventually the electron hole pairs thermally settle to the lowest energies of the conduction and valence bands. Much of the energy of the incident electron is converted into phonons (thermal energy), therefore the CL process is considerably less efficient than PL. It has been found experimentally that the penetration depth of the primary electrons,  $R_e$ , depends on the incident electron beam energy,  $E_b$ , with the relationship [100],

$$R_e = \left( \frac{0.052}{\mathbf{r}} \right) E_b^{1.75} \quad (3.11)$$

where  $\mathbf{r}$  is the material density in  $\text{g/cm}^3$ . Therefore, by increasing the beam energy the secondary carriers which contribute to luminescence will be generated deeper in the

sample. This allows for the measurement of luminescence from deeply embedded quantum wells in laser structures.

Since CL measurements are usually taken in a scanning electron microscope (SEM) while measuring the luminescence, there is also the ability to scan the electron beam and image the sample. However, since the CL efficiency is very low, samples must be cooled in order to get sufficient signal. Figure 3.14 shows CL from GaInNAs, GaInNAsSb, and a 980 nm InGaAs standard sample measured at 4 K. The images are taken by scanning the electron beam across the surface of the sample while imaging the luminescence with the spectrometer at a fixed wavelength. Figure 3.14(c) is a CL image from an InGaAs quantum well sample which has 980 nm room temperature PL. From the image, it is clear that luminescence is very homogeneous across the surface of the sample suggesting very homogeneous material with a uniform bandgap. When measuring GaInNAs with 1.3  $\mu\text{m}$  room temperature luminescence, Figure 3.14(a), the image is very spotty with bright and dark spots across the wafer surface. Figure 3.15 shows the luminescence spectrum from the GaInNAs sample in Figure 3.14(a) which was obtained by scanning the sample while measuring the spectrum in a spectrometer. The spectrum clearly shows two peaks from the material which was unresolved when measuring PL at room temperature. The image in Figure 3.14(a) was scanned with the spectrometer wavelength fixed at the peak of the CL signal at  $\sim 1230$  nm. One possible origin of the double peak emission in Figure 3.15 could be from different compositions in the quantum wells since these are 3 quantum well samples. However, a second image was taken at the lower intensity peak at  $\sim 1200$  nm in the CL spectrum and this image had relatively an inverse contrast to the first that was measured. This suggests there is a great deal of non-uniformity within the quantum well and the bandgap fluctuates laterally across the material. There could be many explanations for this type of behavior, but at this scale, phase decomposition is the most likely candidate.

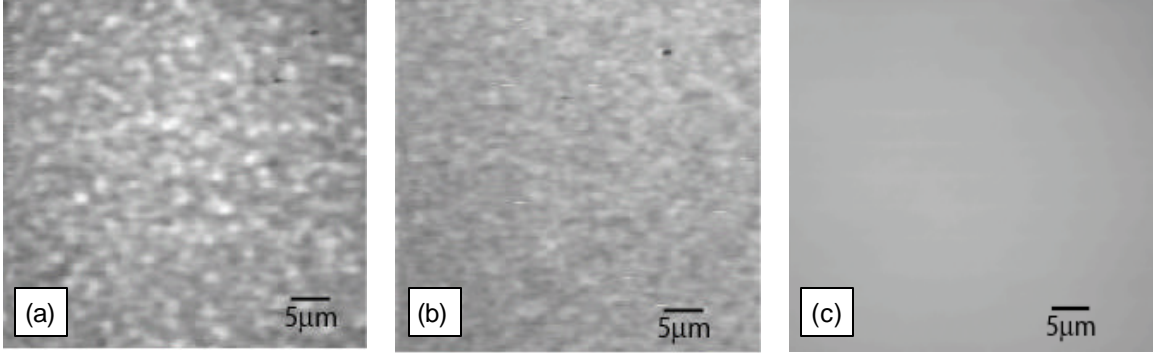


**Figure 3.14: CL scan of 3 QW samples at a temperature of 4 K: (a) annealed 1.3 mm RT-PL GaInNAs, (b) annealed 1.48 mm RT-PL GaInNAsSb and (c) a 980 nm RT-PL InGaAs.**

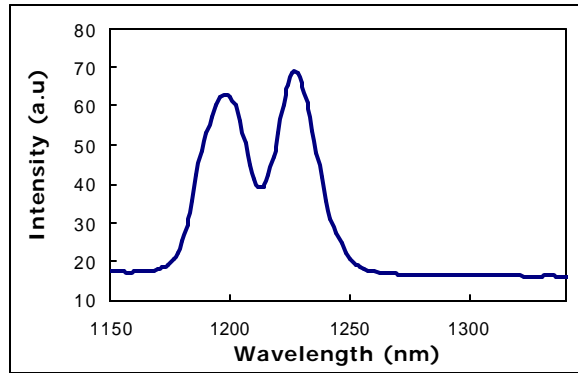


**Figure 3.15: CL spectrum for the 3 QW GaInNAs sample imaged in Figure 3.14(a). The sample temperature was 4 K.**

Next, a GaInNAsSb sample with a room temperature PL at 1.48  $\mu\text{m}$  was measured, and the CL image is shown in Figure 3.14(b). The expectation was to have increased phase segregation since the In concentration in this sample was increased compared to the sample in the Figure 3.14(a) from 30% to 39%. The N was kept the same but Sb was now added with a beam flux  $1.2 \times 10^{-7}$  Torr. The CL image from this sample, however, looks more uniform with lower contrast. The fluctuations are on a smaller scale and less pronounced. Qualitatively from the image, it appears the uniformity across the quantum wells was considerably improved by adding Sb. This suggests that Sb during GaInNAs growth acts as a surfactant and improves surface mobility of N and In improving the uniformity of incorporation.

The CL spectrum was measured with varied electron beam currents, 1.5 nA to 500 nA, while the sample was held at a temperature of 4 K. The intensity-dependent

CL from the GaInNAsSb sample in Figure 3.14(b) is plotted in Figure 3.16 for the as-grown sample and Figure 3.17 for the annealed sample. Though the intensity of CL increases with increasing beam currents, the spectra are normalized in order to allow a better visual comparison. A simplified drawing of the band structure in these samples is shown in Figure 3.18 assuming inhomogeneous GaInNAs quantum wells with fluctuation in the N composition. Since N is thought to anticross with the conduction band, for inhomogeneous material, there would be a great deal of electron localization due to fluctuations in the conduction band energy. The electron localization will be most apparent at low beam currents at low temperatures when the carriers are confined to localized band energy minima. As the beam current is increased and the conduction band density of states is filled, the carriers will occupy more de-localized levels in the band, and the spectrum will begin to look more symmetric. In Figure 3.16, at low beam currents, the CL shows a two peak spectrum which becomes more Gaussian-like with increasing current. The annealed sample in Figure 3.17 has a three peak spectrum which begins to look more Gaussian at higher currents. However, the biggest difference between the as-grown and annealed material is the change in energy with increasing current. The as-grown sample is found to blueshift with current increasing from 1.5 nA to 150 nA and saturates at 500 nA, while the annealed material does not shift as much. This suggests that the as-grown material has a greater degree of localization than the annealed material and with increasing current the carriers leave the localized states and into more de-localized wider bandgap regions in the material, resulting in a spectral blueshift.

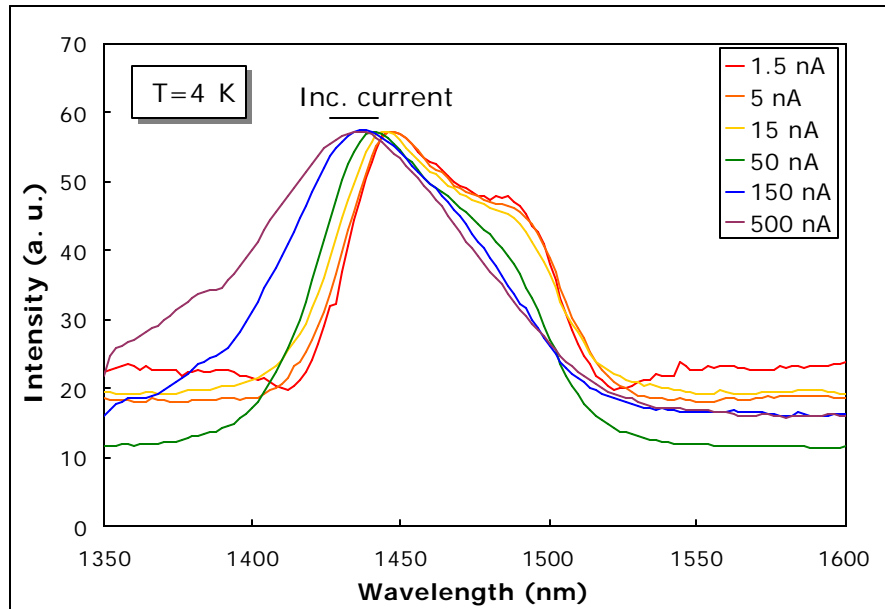


Figure 3.16: As-grown 3 QW GaInNAsSb CL spectrum with varied electron beam current from 1.5 nA to 500 nA.

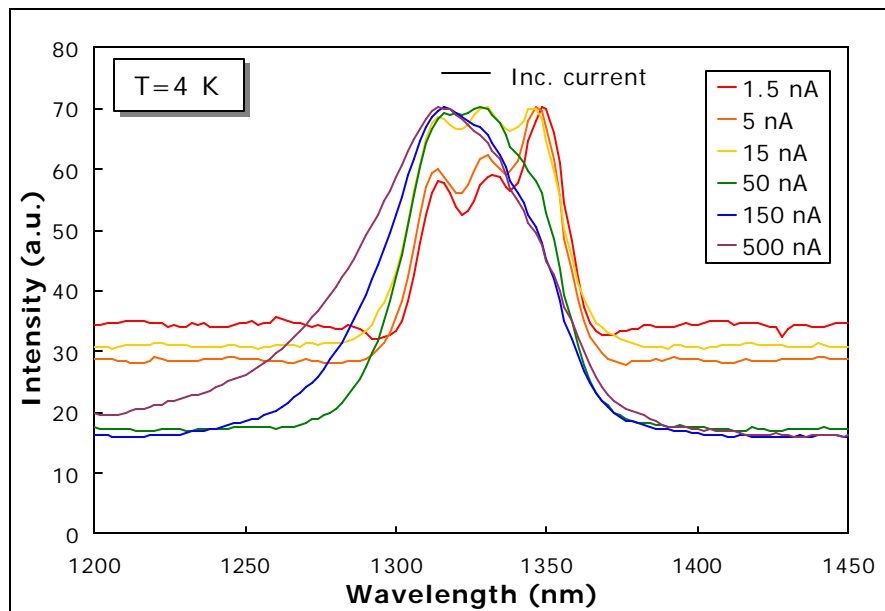
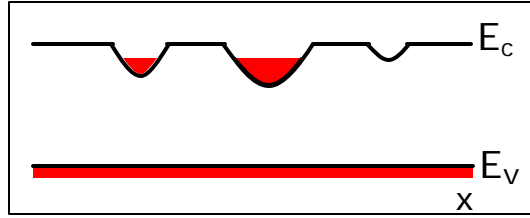
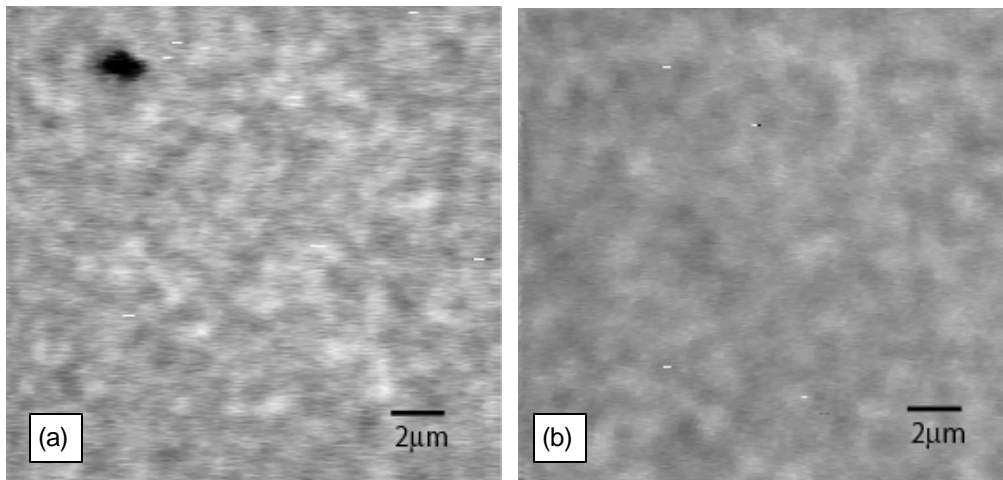


Figure 3.17: The sample in Figure 3.16 annealed for 1 minute at 760°C intensity-dependent CL spectrum with electron beam currents from 1.5 nA to 500 nA.



**Figure 3.18: A drawing of the conduction and valence energy band structure in real space assuming some non-uniformity in the N concentration.**

Further evidence of the reduction in localization after anneal can be seen in the CL images shown in Figure 3.19. When comparing these images, as opposed to the difference by adding Sb, the anneal appears to coarsen the CL, but again decreases the contrast due to localization. The uniformity improves on anneal in both GaInNAs and GaInNAsSb with the annealed GaInNAsSb having the smallest degree of CL fluctuations. However, there are a few caveats one must consider in interpreting this data. First the measurements are taken at 4 K, while the observed localization will effect room temperature luminescence the degree is unknown. Also, there are clear signs of an inhomogeneity of the bandgap across the sample, but it is also unknown how this really affects the luminescent properties such as intensity, energy, linewidth and temperature related performance. While localization may effect room temperature linewidth broadening, other factors probably contribute more strongly to the intensity improvement and blueshift on anneal.



**Figure 3.19: CL image taken from (a) an as-grown GaInNAs sample and (b) the same sample post-annealed.**

# **Chapter 4: (Ga,In)(N,As,Sb) Material Characterization**

This chapter covers various analytical techniques used to further characterize the nitride-arsenide alloy. Compositional determination of N in these alloys can be difficult, particularly in the GaInNAsSb quinary system. Techniques used to carefully separate the elemental concentrations are discussed. When annealed at high temperatures, luminescence of GaInNAs improves and the bandgap energy increases. Changes that occur in the alloy which affect the optical properties are covered. Finally, critical thickness and strain compensating structures for highly compressive films are discussed for the remainder of the chapter.

## **4.1 Compositional Analysis**

### **4.1.1 Determining the nitrogen concentration in GaNAs**

Many different techniques can be used to quantify elemental composition, each having their own sensitivity, accuracy and measurement limitations. Each measurement has its own unique qualities; such features include surface sensitivity, depth profiling, or lattice site specificity. One class of techniques is based on particle emission after electron or photon excitation of the electronic cores of constituent elements. If core electrons are excited, the emission from the target elements is independent of chemical bonding, to first order. Some examples of techniques utilizing this property include Auger emission spectroscopy (AES), X-ray photoelectron spectroscopy (XPS), X-ray fluorescence (XRF), and electron probe micro-analysis (EPMA), all commonly used for either quantifying chemical composition of highly concentrated material or as a surface sensitive measurement. Unfortunately, all of these

methods are rather insensitive to detecting the amount of N present in dilute nitride-arsenide samples.

When core electrons are excited by an incident photon or electron, the type of particle emitted will depend strongly on the atomic mass of the target element, as shown in Figure 4.1. For light elements such as N, the most likely emitted particles are Auger electrons. Therefore, techniques that detect emitted electrons, such as AES and XPS, should be the most useful candidates for N concentration calibration. However, the mean free path for electrons which do not have altered energies leaving the surface is very short (between 5-20 Å); making these techniques highly surface sensitive, as shown in Figure 4.2. Since N is both a target element and a common surface contaminant, the first step to analysis would be to sputter the first few monolayers from the sample. However, when this was performed, N preferentially sputtered and its signal was substantially reduced after the sputtering process. While this analysis does detect N it would not be very accurate since the concentration is now altered. Techniques such as XRF and EPMA use X-rays and electrons, respectively, to induce photon emission. While the photon yield is small for light elements, the escape depth for the photon is much greater (on the order of microns); making these techniques much less surface sensitive. However, these techniques are really only sensitive to high N concentrations and EPMA was only used to detect N in concentrations above 10%.

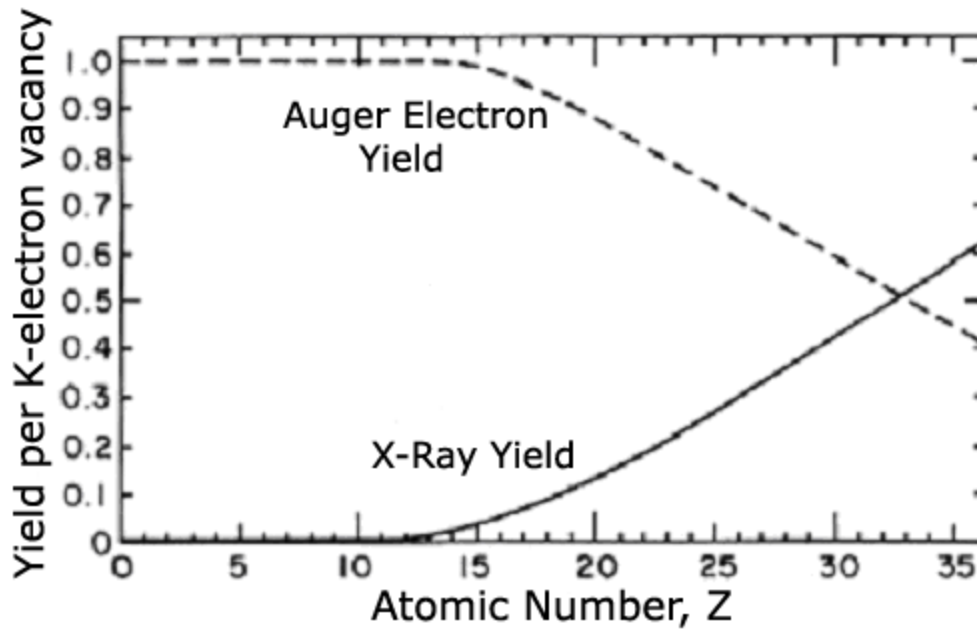


Figure 4.1: Auger electron and X-ray yield per K vacancy as a function of the atomic number  $Z$  [101].

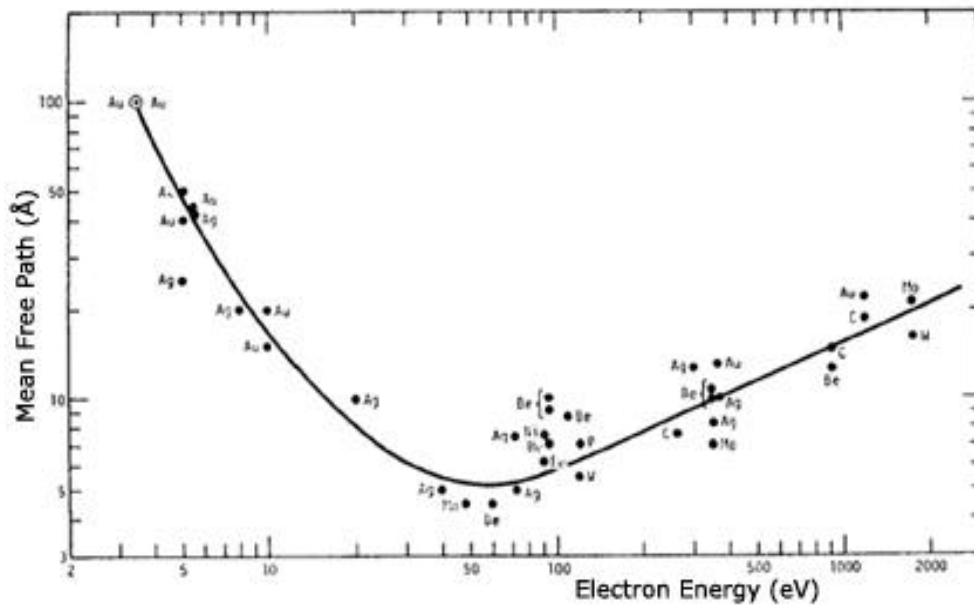


Figure 4.2: Escape depth for electrons of varying electron energy [102].

Despite problems with many analytical methods, three techniques were successfully used to accurately measure N concentrations: high resolution X-ray diffraction (HRXRD), nuclear reaction analysis RBS (NRA-RBS) and secondary ion

mass spectrometry (SIMS). HRXRD can detect components which contribute to a change in the lattice parameter, primarily atoms on substitutional sites. It can also be used to determine film thickness very accurately based on the X-ray interference between layers. For thicker films NRA-RBS can be highly accurate for quantitative chemical composition analysis and at the same time distinguish between total concentration and interstitial content of a target element. SIMS is adept at depth profiles and extremely sensitive to dilute quantities of a component but needs to be carefully calibrated using standard samples for compositional.

#### 4.1.2 Nitrogen calibration using X-ray diffraction

One of the most useful techniques for analyzing epitaxial films is XRD, which measures the lattice parameter of the film and can give information about strain, film thickness, relaxation, precise compositional information for ternary alloys that follow Vegard's Law, and useful information by fitting the data in more complex alloys. The peaks in an X-ray diffraction pattern are directly related to the atomic distances. Constructive interference of X-ray radiation occurs at certain angles of diffraction, depending on the lattice spacing as given by the Bragg's law [103],

$$n\lambda = 2d_{hkl} \sin \theta \quad (4.1)$$

where  $n$  is the order of the diffraction, since the periodicity of the waves can be any positive integer,  $\lambda$  is the wavelength of the incident X-rays,  $\theta$  is the diffraction angle and  $d_{hkl}$  is the spacing between hkl planes. For cubic crystals,  $d_{hkl}$  is related to the lattice spacing,  $a$ , with the following relationship,

$$\frac{1}{d_{hkl}^2} = \frac{h^2 + k^2 + l^2}{a^2}. \quad (4.2)$$

When measuring relaxed, unstrained films, Bragg's law is sufficient for most analysis since the film relaxes to its equilibrium lattice parameter. For the InGaAs ternary, an (004) rocking curve of a relaxed film can give information on composition based on lattice spacing  $d_{hkl}$  and film thickness based on width of the diffraction peak. In the dilute GaNAs ternary, strained films on GaAs were grown, tetragonally distorting the (004) lattice spacing. Figure 4.3 shows an example of an (004) rocking curve diffraction pattern of strained 1.27% N GaNAs on GaAs. In a cubic crystal the

equilibrium unstrained lattice parameter,  $a_{eq}$ , can be calculated from the (004) lattice parameter  $a_{004}$  with the relationship

$$\mathbf{s}_z = 0 = 2C_{12}\mathbf{e}_{in-plane} + C_{11}\mathbf{e}_{out-of-plane} \quad (4.3)$$

or rewritten as,

$$a_{eq} = \frac{2\frac{C_{12}}{C_{11}}a_{GaAs} + a_{004}}{\left(1 + 2\frac{C_{12}}{C_{11}}\right)} \quad (4.4)$$

where  $\mathbf{e}_{in-plane}$  is the in-plane strain for the unrelaxed film where

$$\mathbf{e}_{in-plane} = \frac{a_{GaAs} - a_{eq}}{a_{eq}}, \quad (4.5)$$

and  $\mathbf{e}_{out-of-plane}$  is the out-of-plane strain in which

$$\mathbf{e}_{out-of-plane} = \frac{a_{004} - a_{eq}}{a_{eq}}. \quad (4.6)$$

The constant  $a_{GaAs}$  is the lattice parameter of GaAs, and  $\mathbf{s}_z$  is the strain in the out-of-plane direction. The parameters  $C_{11}$  and  $C_{12}$  are the stiffness coefficients for the film where the ratio  $2C_{12}/C_{11}$  is around 0.9 for most III-V materials [104]. Using the unstrained lattice parameter, N concentration was calculated based on Vegard's law which should be valid in the dilute regime [63]. In order to obtain an accurate unstrained lattice parameter value, the above calculation assumes there is no relaxation. Reciprocal space maps of GaNAs on GaAs in a (224) orientation were taken to measure both in-plane and out-of-plane lattice parameters. From the space map, shown in Figure 4.4, it appears there is no relaxation of the GaNAs layer and the crystal is coherently strained to the GaAs substrate.

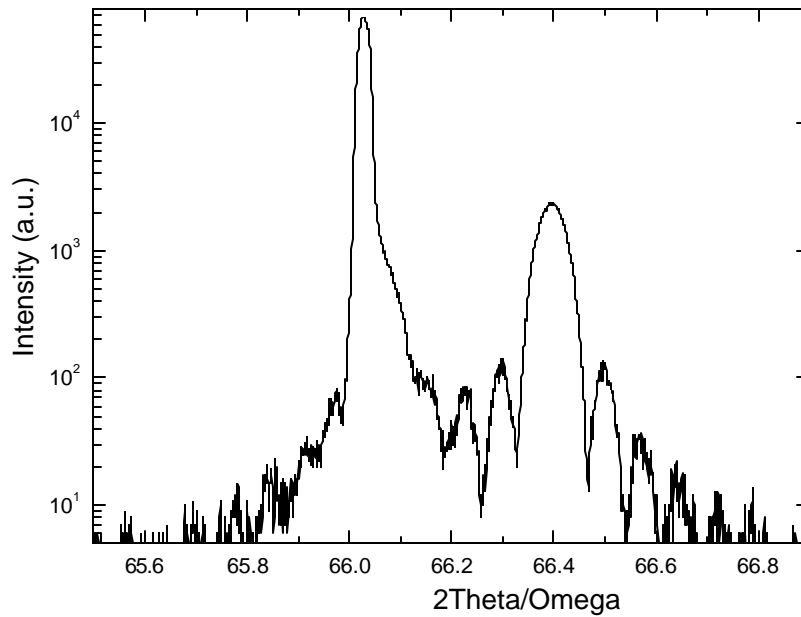


**Figure 4.3: (004) rocking curve of GaNAs on GaAs where the N was measured to be 1.27% GaN. The slightly tensile peak to the right of the GaAs peak is a thick film of dilute GaNAs formed when igniting and stabilizing the plasma cell behind a closed shutter.**

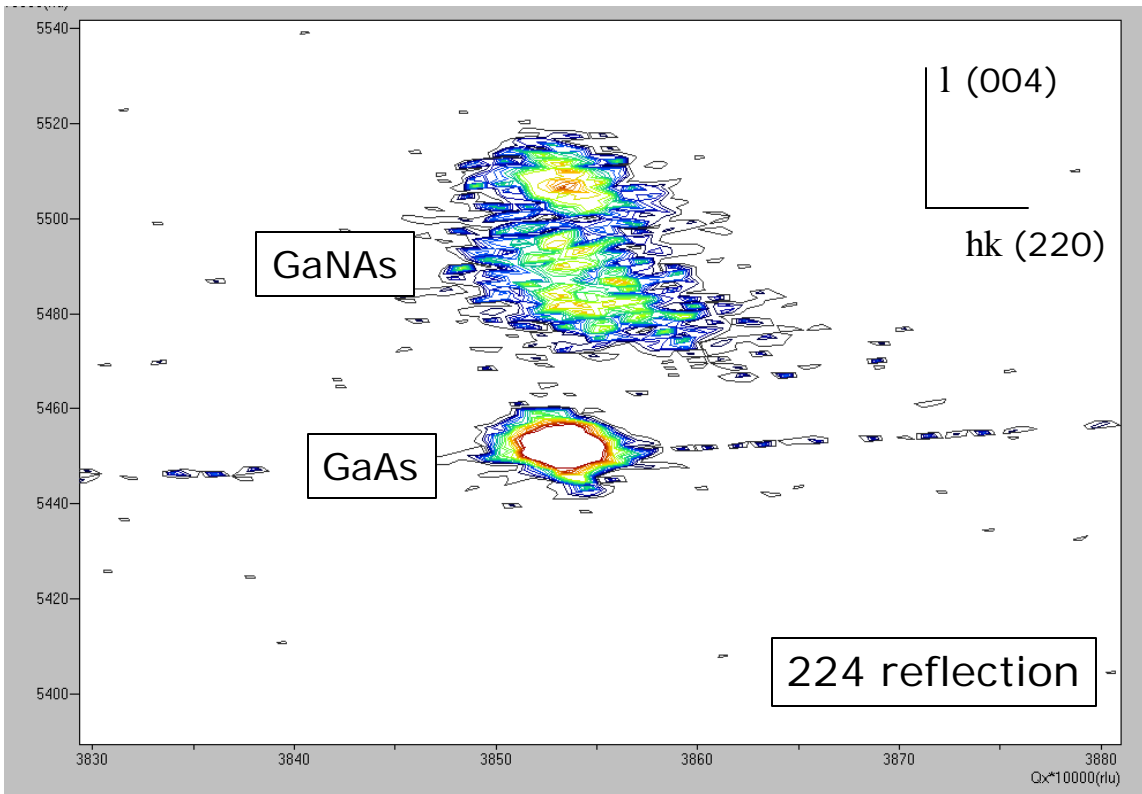


**Figure 4.4: Reciprocal space map of the (224) diffraction of GaNAs on GaAs.**

### 4.1.3 Nuclear reaction analysis Rutherford backscattering spectroscopy

Another technique that is commonly used to quantify chemical composition in semiconductor films is RBS. A schematic of the RBS setup is shown in Figure 4.5. In the RBS technique, an incident ion beam, commonly He, is accelerated toward the sample at high energies. A small fraction of He undergoes a direct collision with the atoms within a few microns of the surface and backscatter elastically. The energy of the detected He ions backscattered from the sample depends on the energy lost traveling through the material and the energy lost as a result of the collision itself. The number of ions that backscatter from a particular element depends on both the concentration of the element and the effective size of its nucleus. The probability of a collision event for an element is called its scattering cross section. This technique is particularly effective for heavy metal thin films on light substrates using  $^4\text{He}^{++}$  ions. A heavy element will have a signal from high energy backscattered ions separated from the lower energy backscattered He ion signal from the substrate. Then as the ions escape from the film they lose energy as they travel, the spread in energy between high energy surface scattering and lowest energy ion escaping is related to the thickness of the film. With a thin layer of a heavy element on a thick light elemental substrate, there will be a clear separation between the backscattered peaks from the film and substrate. However for a film such as GaNAs on GaAs the lighter GaNAs film will be obscured by the substrate signal, making analysis difficult.

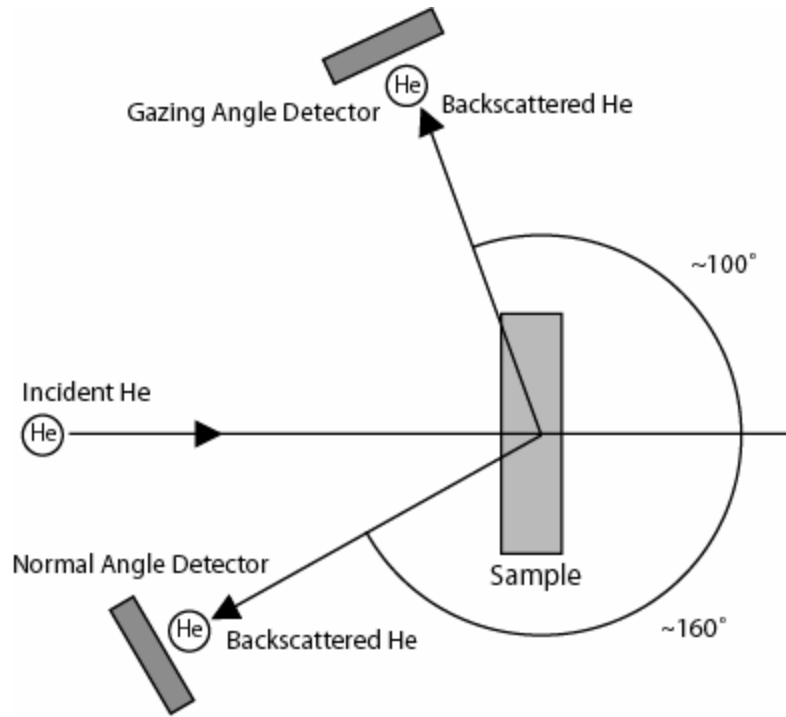
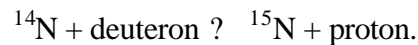


**Figure 4.5: Schematic of RBS setup.**

To improve N detection sensitivity and accuracy NRA-RBS was used to measure the N areal density in the film. Typical (non-NRA) RBS experiments are done with lower energy beams, since He ions with energies below 2.2 MeV scatter elastically with all the elements. At energies higher than this, the ions collide non-elastically with the nuclei, increasing the collision cross section at certain resonant energies. At these resonant energies, the incident ion is absorbed and reemitted by the nucleus instead of simply scattered by it. For such nuclear reactions, a variety of particles, such as protons or  $\gamma$  rays are emitted. In this NRA-RBS analysis, a deuteron beam was used at an energy of 2.275 MeV, initiating the nuclear reaction  $^{14}\text{N}(\text{d},\text{p})^{15}\text{N}$ , or rewritten as,



The detection of the resulting proton spectrum allows for parts per million sensitivity of the N concentration when calibrated with a standard sample of known N content. The RBS spectra are fit using a theoretical model simultaneously fitting the normal and grazing detector spectra to determine the physical structure of the sample.

Another variation on the RBS technique which can provide more structural information of the material is ion channeling. Using single crystal samples, the ion

beam can be focused down crystallographic directions, allowing the incident ions to be channeled down the open regions in the crystal lattice. The ions are steered down rows of atoms reducing the backscattered yield from substitutionally located atoms. The beam will then be highly sensitive to non-substitutional sites and can quantify impurity atoms, such as interstitials, in the crystal. In order to study the interstitial concentration,  $^2\text{He}$  ions were channeled down the (001) crystal axis of a GaNAs film. In this orientation, substitutional atoms have a very low backscattering yield and interstitial atoms are highly visible. To measure total elemental concentration the sample is held in a rotating random orientation off a crystallographic axis. Figure 4.6 shows the NRA-RBS results comparing the channeled versus random crystal orientation. The N signal, shown on channel 200, is reduced in channeled orientations. Other peaks present in the data close to the N signal are surface contaminants, such as C and O, which appear in both random and channeled orientations. Table V summarizes the data from the NRA-RBS experiment taken in both channeling and random orientations before and after rapid thermal annealing (RTA) the sample. It lists both %N which is the total concentration of N in a random orientation and interstitial %N which is the portion of the total N that is on interstitial sites. Shown in gray and listed as a previous design are the values of total N and interstitial N for a sample grown with 9 instead of 4 holes in the front aperture and double the flow rate, as described in section 2.3.2. With the new plasma cell configuration and altered operating parameters only 5.8% of the total N was incorporated as interstitials while with low flow rates and nine hole initial front aperture, the interstitials were as high as 26% [61].

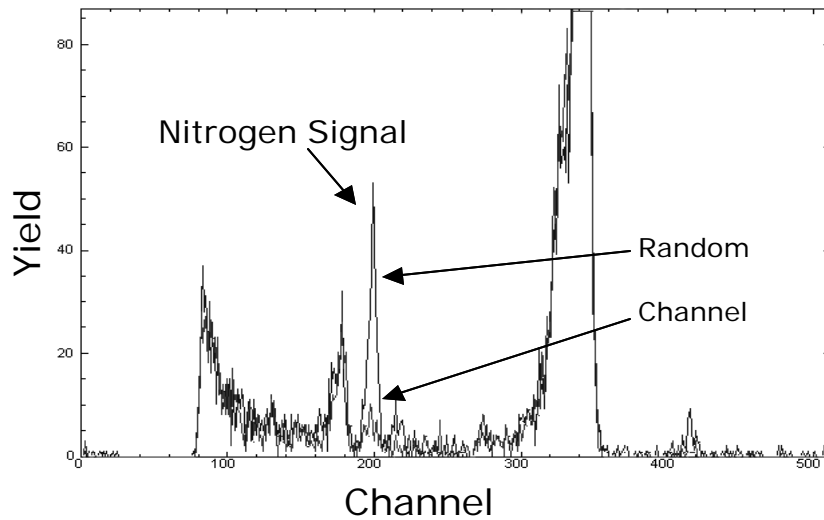


**Figure 4.6: NRA-RBS spectrum of a 150 nm GaInNAs film. The arrows point to the nitrogen peak for both channel and random crystal orientations.**

**Table V. Total nitrogen and interstitial nitrogen content on GaNAs, GaInNAs and GaInNAsSb before and after anneal. Rows in grey, labeled “prev. design”, are data taken from material grown with the initial nine hole front plasma cell aperture.**

	% N	Interstitial N %
GaNAs	2.4	5.8
<b>-annealed</b>	<b>2.0</b>	<b>8.3</b>
GaIn <sub>0.08</sub> NAs	2.4	3.7
<b>-annealed</b>	<b>2.4</b>	<b>4.2</b>
GaIn <sub>0.08</sub> NAsSb <sub>0.07</sub>	3	6.9
<b>-annealed</b>	<b>3</b>	<b>8.2</b>
GaNAs (prev. design)	3	26
<b>-annealed</b>	<b>3</b>	<b>16</b>

#### 4.1.4 Secondary ion mass spectrometry (SIMS)

Another powerful analytical tool commonly used for semiconductor thin films is SIMS depth profiling. A focused energetic ion beam is used to carefully sputter atoms from the surface of the sample generating secondary ions. These secondary ions are then detected by a mass spectrometer. To measure N composition, data was acquired using a 60 degree off normal incident 1 keV Cs primary ion beam in a high depth resolution quadrupole SIMS. The incident beam energy was chosen to sputter the sample and minimize ion-beam mixing and knock-on broadening of the interfaces in the depth profile. Many secondary ions that can be used for material analysis are

generated from the sputtering process. For N profiles, both GaN<sup>-</sup> and CsN<sup>+</sup> can be analyzed when sputtering with a Cs beam. Since N does not form a negative atomic secondary ion, it is necessary to measure a molecular ion such as GaN<sup>-</sup>. This ion is produced with high yield, giving depth profiles with good detection limits, but for layers where the Ga concentration changes, the apparent N signal (measured as GaN<sup>-</sup>) will also show a change. As a result, changes in the GaN<sup>-</sup> signal may be due to the variations in Ga, and not necessarily due to a real change in the N concentration, making it difficult to quantify. The CsN<sup>+</sup> data used for the quantitative N profiles should not be subject to this matrix effect. However, because of lower secondary ion yields in the CsM<sup>+</sup> configuration, the CsN<sup>+</sup> profiles tend to be noisier than the GaN<sup>-</sup> profiles.

The fraction of sputtered particles that are actually ionized by the primary beam is usually much less than 1%. The likelihood that a sputtered particle escapes from the surface as an ion depends on the relative probabilities of ionization and de-excitation as it passes through the near surface region. Therefore, the ion yield depends strongly on the electronic properties of the matrix. While this can make quantitative analysis difficult, known standard samples can be used in order to obtain accurate results. To reduce the effect of the matrix of N in GaNAs, an NRA-RBS measured GaNAs film of similar composition to the SIMS sample was used to calibrate the N signal. This technique was used for the SIMS data in Figure 3.7 to calibrate the composition of the N profile.

#### **4.1.5 GaInNAsSb compositional analysis**

Similar analytical techniques were used to calibrate In and Sb in the five component alloy. However, the alloys grown with a bandgap near 1.3  $\mu\text{m}$  are highly strained on GaAs, therefore, using thick film measurement techniques are not possible. Surface sensitive tools, such as XPS, were used on some samples to accurately measure the composition of In and Sb of a thin film on the surface.

With highly strained layers, X-ray diffraction of superlattice layers can give highly accurate information of the strain and thickness of individual layers. XRD rocking curves of PL samples with strained GaInNAs and GaInNAsSb quantum wells

were measured to determine layer thickness, layer strain, interfacial roughness, and the degree of relaxation. Figure 4.7 shows the (004) superlattice diffraction pattern from three 8 nm quantum well GaInNAsSb sample with 20 nm GaNAsSb barriers between the quantum wells. The broad background peak at angles smaller than the GaAs substrate peak ( $-6000$  arcsec) comes from diffraction of the thin 8 nm quantum wells. From the diffracted angle, the strain of the layers can be determined. The superlattice fringes present in the pattern come from thickness interference reflections between strained layers and the surface of the sample. Finally, the peaks at angles larger than the substrate peak originate from the slightly tensile thicker barriers between quantum well layers used for strain compensation. The simulation of the diffraction pattern and the results from the simulation are also shown on the plot. While the layer thickness and strain can be very accurately determined, very little compositional information can be obtained. Different components do alter the diffraction pattern due to difference in scattering factors, but the effect is so slight that very little information can be derived beyond statistical error.

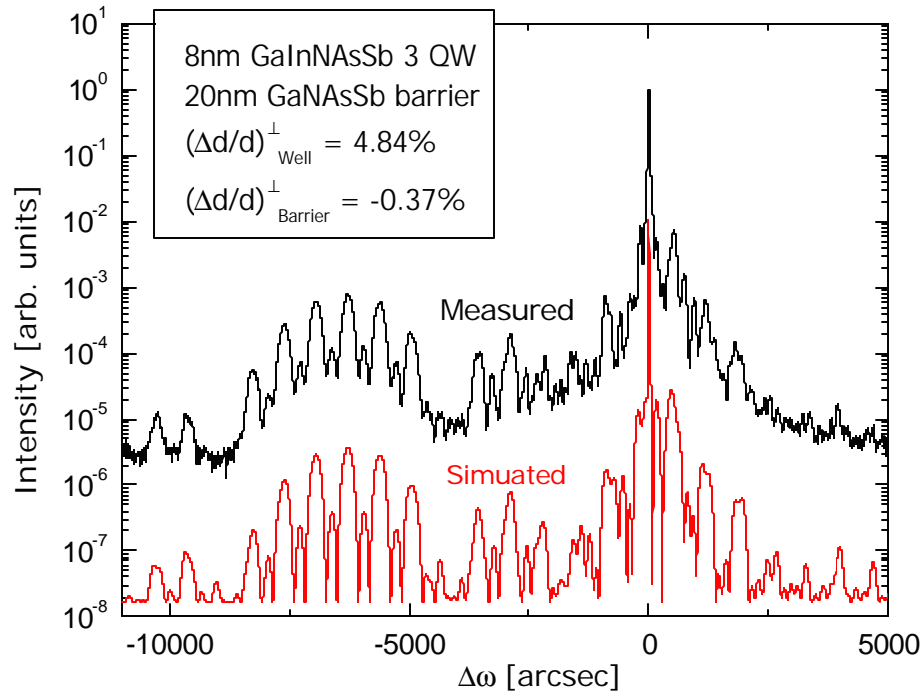


**Figure 4.7: XRD (004) rocking curve measurement of three 8 nm QW GaInNAsSb with 20 nm GaNAsSb barrier superlattice. Dynamical simulation shown below measured curve.**

Similar to GaNAs, RBS and SIMS can also be powerful techniques for compositional determination in GaInNAsSb. In order to calibrate SIMS profiles RBS samples are used to determine the ionization yields of In and Sb and to compensate for matrix effects. However, RBS is not a surface sensitive technique and films as thick as 100 nm needed to be grown. Therefore lattice matched films of GaInNAsSb with small concentrations of In and Sb were used for standards. Furthermore, due to the similar sized cross section of In and Sb, particle induced X-ray emission (PIXE) RBS was used to distinguish between the elements. PIXE-RBS is similar to NRA-RBS, except the incident beam produces characteristic X-rays from the target elements which are then detected. This technique is useful for heavy elements with RBS signals at similar energies, such as In and Sb. The Sb concentration in the GaInNAsSb sample in Table V was calibrated using PIXE-RBS and then used as a calibration standard in the SIMS sample of Figure 3.7.

The Sb incorporation rate in GaInNAs was determined using RBS calibrated SIMS and an expanded SIMS profile of Figure 3.7 is shown in Figure 4.8 for the N and Sb concentrations. The layer profile of this sample is shown schematically within the plot. From this data it was found that N incorporates with inverse proportionality to the group-III growth rate within 4%. Thus, the N incorporation is less in the quantum well region because the total group-III flux is increased since the In flux is added in this region while the Ga flux is kept constant. However, the Sb does not follow this behavior and 54% less Sb was found in the quantum wells indicating In inhibits Sb incorporation. This quantity was determined using a predicted concentration based on the measured concentration of the barriers and offsetting based on the difference of the growth rate in the quantum wells. Recent measurements suggest that the Sb does not have unity sticking coefficient but incorporation is reduced when In is present. Furthermore, SIMS data has suggested that N incorporation increases with increased Sb, further contributing to the bandgap reduction by adding Sb.

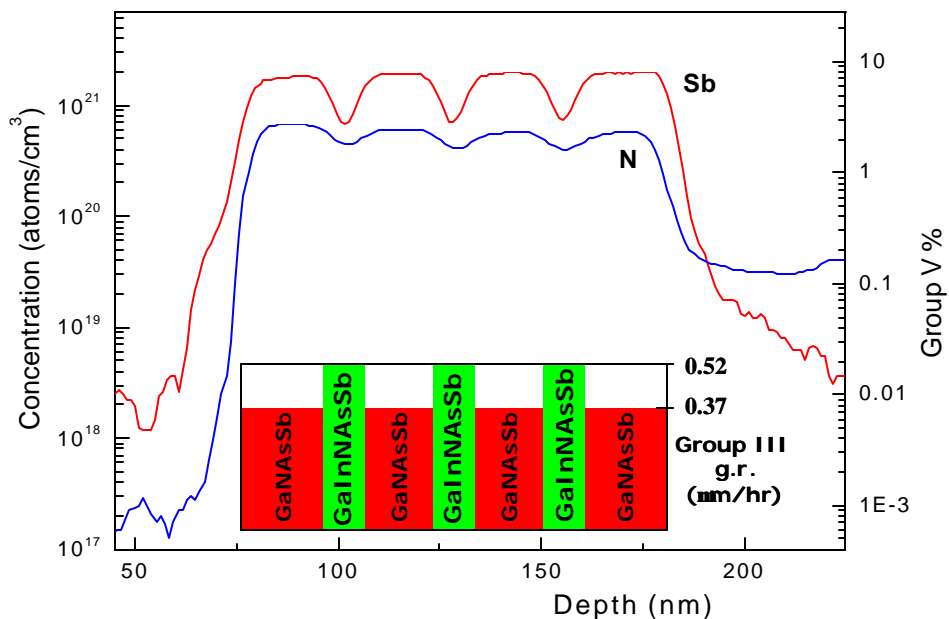


**Figure 4.8: Nitrogen and antimony SIMS profiles of a three QW GaInNAsSb sample with GaNAsSb barriers. The flux of N and Sb remained constant during growth.**

## 4.2 Structural Changes on Anneal

### 4.2.1 Atomic rearrangement in GaInNAs

Understanding the mechanisms which improve luminescence and blueshift the bandgap after annealing GaInNAs has recently become a major focus of research. From the anneal behavior shown in Figure 3.4, three specific changes occur in the material. First, the optical properties improve at lower anneal temperatures, second, at higher temperatures the luminescence decreases, and throughout the above is a continuous blueshift and increase in bandgap. Conventional wisdom would suggest that competing diffusion mechanisms control the optical quality and bandgap during post-growth anneal. It is possible that the removal, or diffusion and annihilation of point defects, such as interstitials or antisites, control the improvement of radiative emission in the material. The blueshift of emission may be caused by the out-diffusion or interdiffusion of atoms in a direction that increases the bandgap. The last competing diffusion mechanism could be phase segregation or the reduction of interfacial quality which could reduce PL intensity at even higher anneal temperatures.

In a four component system there could be many different types of likely diffusion in the GaInNAs alloy. First is the diffusion of N out of the quantum wells. Since N is a small atom and incorporated under metastable conditions, it would seem possible for N to quickly diffuse away from the active region and blueshift the bandgap. The next type of atomic rearrangement could be N and As phase segregation within the active region caused by the post-growth thermal treatment. Due to the miscibility gap between GaN and GaAs, growth of high N content GaNAs quantum wells can decompose under enough strain, or during higher temperature growth. Figure 4.9 shows a cross sectional transmission electron microscope (TEM) image of high N content GaNAs quantum wells in which the upper layers began to phase segregate during growth and significantly roughen the surface. While the layers grown in device structures have much less N incorporated, some degree of phase segregation could occur during growth or anneal. Some degree of phase segregation, or atomic clustering and then a change in the microstructure after anneal was observed in the CL study done in section 3.5. Similar to N-As phase segregation, In and Ga could also undergo slight

phase segregation. While this is not common for traditional InGaAs, it is a major problem in the high In concentration InGaN system. A typical XRD rocking curve of phase segregated InGaN on GaN is shown in Figure 4.10. With N present in the alloy, phase segregation of InAs and GaAs could become energetically favorable. If this does occur, it could contribute to bandgap intensity changes of PL after anneal and could also help explain the CL non-uniformity in GaInNAs. A fourth diffusion mechanism possible is the interdiffusion of atomic components and a redistribution of the nearest neighbors in the alloy. With a change in the short range order of components in the alloy, the bandgap of the material can change, particularly since N has such a strong effect on the bandgap in the dilute nitride-arsenide alloys.

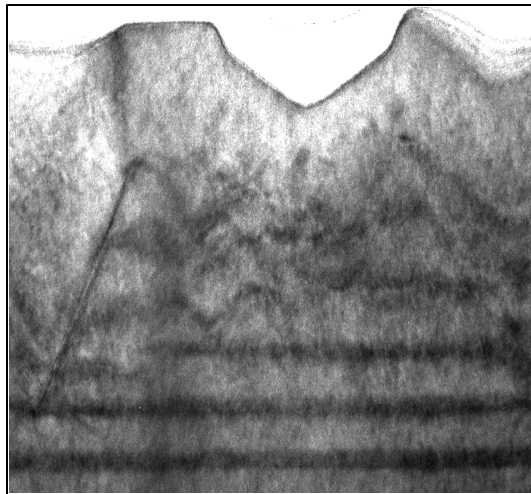


**Figure 4.9: Cross section TEM of six GaNAs QW with 10% N [61].**

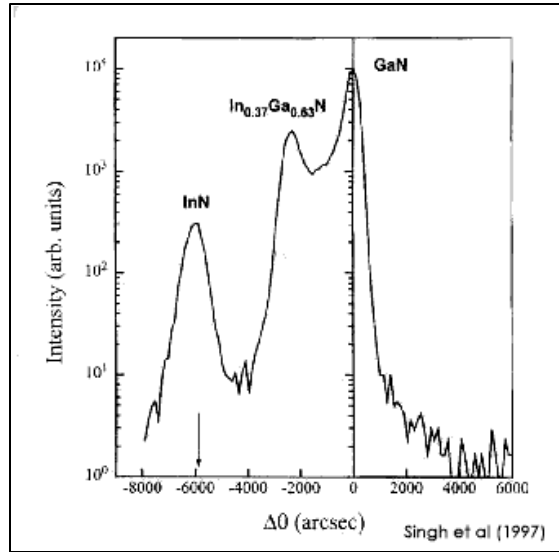


**Figure 4.10: XRD rocking curve of phase segregated InGaN grown on GaN [105].**

#### 4.2.2 Deep level defects

One common reason for an improvement of PL on anneal is the removal of non-radiative defects such as point defects. These deep level defects diffuse on anneal and annihilate one another improving radiative emission. Many groups have found deep levels in as-grown GaInNAs [106-109] and in the samples grown for this thesis research, deep levels were also found [31,110-113]. Unfortunately, the origin of many of these deep levels is currently unknown since deep level defects are not as well characterized in GaAs compared with Si.

One common deep level defect arising from a point defect is the As antisite,  $As_{Ga}$ . This defect is common during low temperature growth of GaAs, around the same temperatures GaInNAs is typically grown. Other defects present in GaInNAs are thought to be N related, either from radiation damage from the plasma, N or  $N_2$  interstitials, or an inherent deep level caused by lattice distortion in the GaNAs alloy. The defects in GaNAs are also known to be very growth related; changing plasma conditions, using different substrate temperature, MBE versus MOCVD growth, may greatly influence the presence of these defects and their annealing behavior. Currently, the As antisite is a very common defect that some groups find is removed on anneal, while others, like the samples grown for this work, find that it is not removed. The N

interstitial is also a common point defect, and as described in section 4.1.3, is related to plasma conditions during growth. While a N interstitial may not greatly effect the band structure in the crystal, a N split interstitial may be the origin of deep levels in the bandgap. Due to the widespread presence of point defects in GaNAs, their origin, anneal behavior, and the influence of deep levels on radiative recombination in N-As alloys is still a current topic of research.

#### **4.2.3 Nitrogen out-diffusion**

Clear signs of N leaving as-grown layers after a post-growth anneal has been found in the nitride-arsenide alloy. Figure 4.11 shows a SIMS measurement of the N profile in two quantum wells of GaInNAs on GaAs. Measuring the profile before and after anneal, it was found that over 35% of the N diffused out of the quantum wells and dispersed throughout the crystal. While it at first seems to prove that a great deal of N leaves on anneal, it must be noted that this sample was grown with the previous plasma cell aperture and flow rate and, therefore, had a large concentration of interstitials (see Table V). These interstitials are the main out-diffusing component and could influence the ionization potential of the sputtered species reducing calibration certainty. However, even in the rocking curves of GaNAs thin films, the (004) lattice constant does increase on anneal, as seen in Figure 4.12, which is further proof of substitutional N out-diffusion.

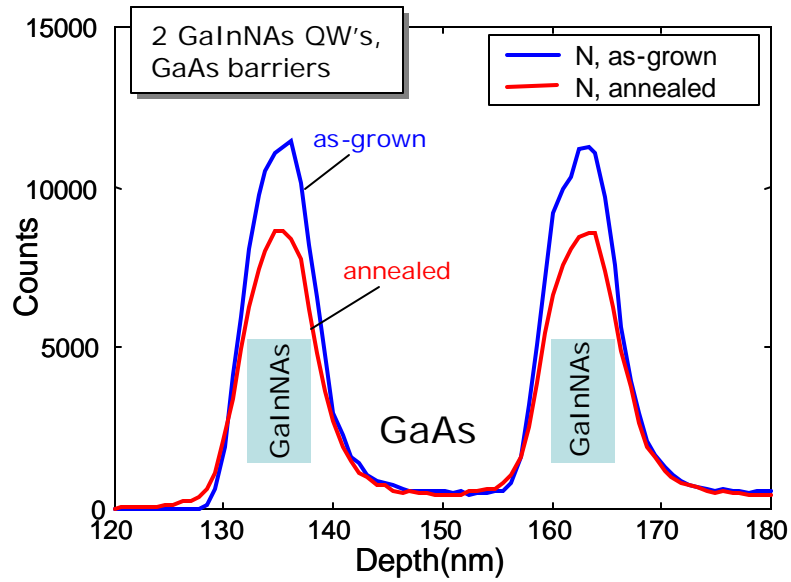


**Figure 4.11: SIMS profile of the N signal from 2 GaInNAs QW in GaAs before and after anneal [61].**

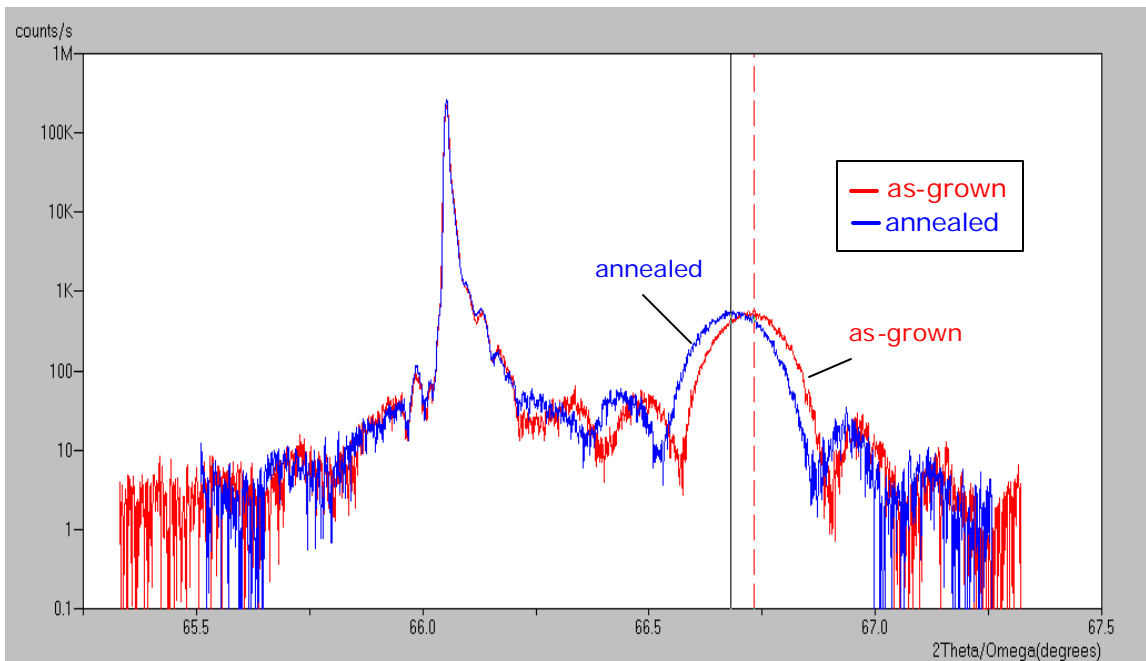


**Figure 4.12: As-grown and annealed (004) XRD rocking curve of a GaNAs 150 nm thin film.**

In order to reduce the effects of this N loss, a new structure was developed in which GaNAs barriers were grown between GaInNAs quantum wells [61]. The barrier layers were grown with a N concentration higher than in the quantum wells such that

the barriers acted as a reservoir of N for the quantum wells and N would diffuse into the wells instead of out. This layer design actually simplifies growth since N incorporation is inversely proportional to growth rate, and the quantum wells with In present have a higher growth rate. Therefore, the N flux is held constant for the entire barrier and quantum well growth and only the In is modulated. Figure 4.13 graphs the SIMS profiles for the new GaNAs barrier structure. Here, 10% N was removed from the barriers while only 8% N was removed from the quantum wells after the anneal. While N out-diffusion is still an issue in the GaInNAs active region, there must be a secondary effect which further increases the bandgap rather than just the reduction of N alone. For instance, in GaNAs quantum well samples, there is a PL blueshift of 20 meV, while in GaInNAs, the typical blueshift is as high as 35-80 meV. This large shift in bandgap cannot be explained by N removal alone, so other diffusion mechanisms have been examined.

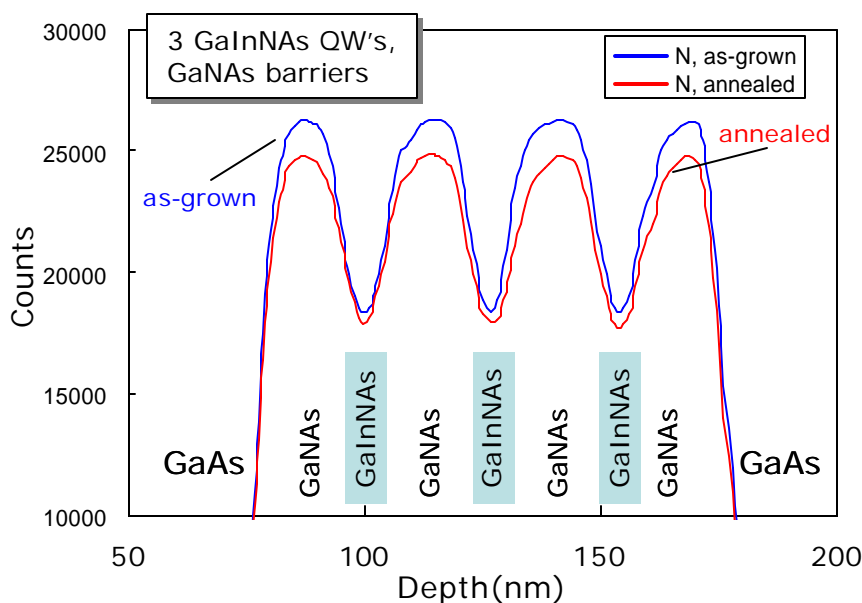


**Figure 4.13: SIMS profile of 3 GaInNAs QW's grown between GaNAs barriers.**

#### 4.2.4 Phase segregation in GaInNAs

Phase segregation and carrier localization has been evident on a large scale in scanning CL measurements [95]. At this point it is unclear which component, whether

it is a group-III or group-V atom, is segregating. Considering that the GaN-GaAs system has a large miscibility gap and the solid solution is grown under metastable conditions, it is very likely that the GaN and GaAs are segregating. Figure 4.9 showed an example of GaNAs phase segregation in high N content films. A similar phase separation occurs in low N GaNAs but when grown at elevated substrate temperatures. Figure 4.14 shows (004) XRD rocking curves of 150 nm GaNAs films grown under the same growth condition except for the substrate temperature. At 400°C the sample morphology was smooth and a single phase was evident in the rocking curve diffraction. Above 450°C, the surface of the film looked very rough and from the XRD pattern, it was found to be segregated into a two phase material. At even higher temperature, very little N was found to incorporate, suggesting increased N desorption at these elevated temperatures. A (224) diffraction pattern was also taken on all three samples to ensure that the films were not relaxed.

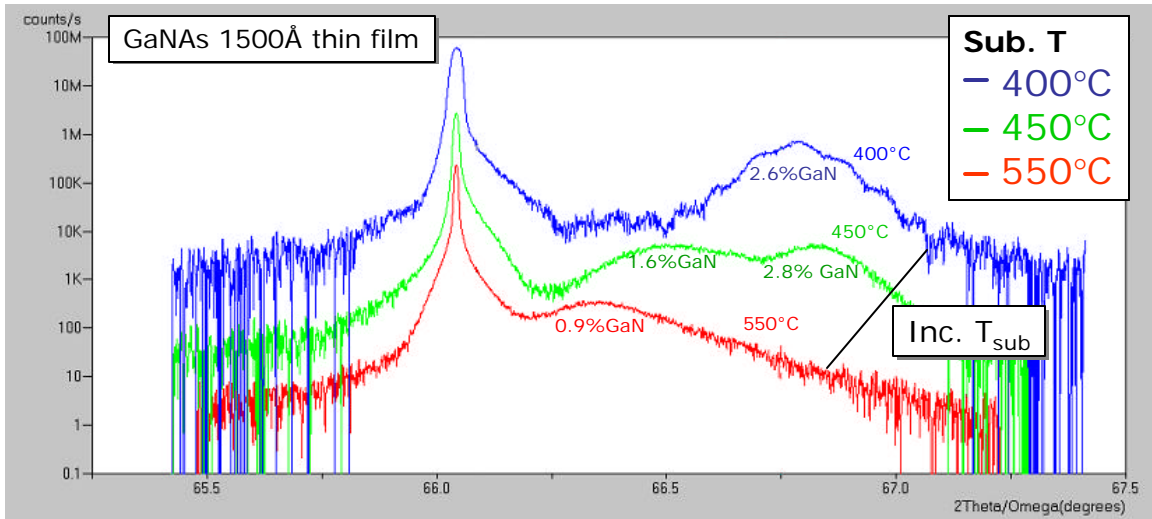


**Figure 4.14: XRD (004) rocking curves of the same GaNAs thin film on GaAs grown at different substrate growth temperatures.**

Another possibility is that the group-III components, In and Ga, may phase segregate. Poor quality GaInNAs material can show a great deal of phase segregation as grown by another research group and shown in Figure 4.15 [114]. In these TEM images, N is not clearly visible since there is not enough mass contrast and it is in very dilute concentrations. Indium creates the largest contrast in this sample and, therefore,

In must be segregated in the layers. For the material grown in this thesis research, there is no evidence of In phase segregation, as shown in the TEM image in Figure 4.16. In this sample, nine GaInNAs quantum wells were grown on GaAs and even at atomic resolution, there is no sign of phase decomposition of In. However, from the CL observations, the decomposition occurs on a scale of microns, and may not appear in these high resolution images. More work is currently being done to determine if phase segregation of N or In occurs in this material, as well as the scale, magnitude, and the participating components of the segregation.

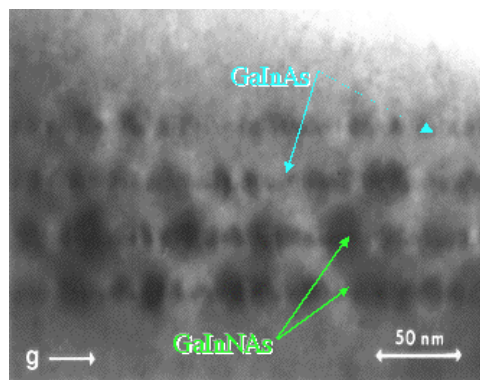


**Figure 4.15: Cross section TEM image of poor quality GaInNAs, showing signs of quantum dot like behavior [114].**

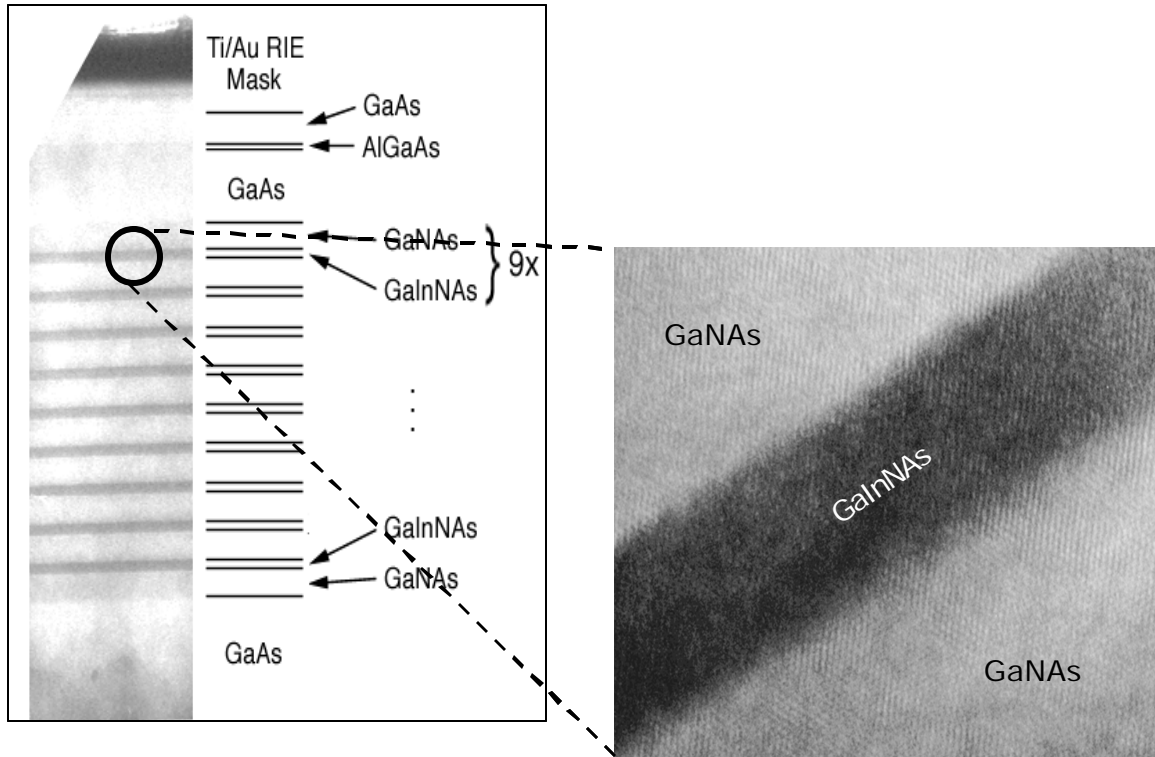


**Figure 4.16: Cross section atomic resolution TEM image of a 9 QW sample of GaInNAs with GaNAs barriers. The blown up image is from the top QW which shows little sign of phase decomposition.**

#### 4.2.5 Changes in short range order

Recent Monte Carlo simulations show that the redistribution of bonds in the GaInNAs alloy can have a strong blueshift effect on the bandgap [115]. It has been found that through changes in nearest neighbor configuration, the bandgap can blueshift as much as 150 meV from the bandgap of the perfectly random alloy. When considering diffusion, two directions for the rearrangement in short range order in the quaternary were considered—the increase or reduction of In-N bonds. The force driving increased Ga-N coordination could be the reduction of free energy of the local bonding, since the GaN bond has a lower energy than the InN bond. For the preferred In-N case, In and N could rearrange together to relieve local strain in the system since In is bigger and N is smaller in the GaAs lattice. Recent measurements using Raman and Fourier transform infrared (FTIR) spectroscopy have confirmed structural changes after anneal. However, these measurements were taken with thick films of closely

lattice matched material due to the small interaction cross-section of the incident light [116]. Instead, in this work X-ray absorption fine structure (XAFS) was used to determine changes in short range order in the GaInNAs alloy before and after anneal. In our XAFS measurements, the probe depth of the X-rays is on the order of a hundred nanometers, allowing thin and even highly strained films to be measured with high sensitivity.

Both fluorescent X-ray absorption near edge structure (XANES) and extended XAFS (EXAFS) were used to measure the nearest neighbor configuration of atoms in the alloy. As-grown and annealed samples with varied thickness and composition, as well as reference samples, were measured. In both techniques, incident X-rays with sufficient energy are absorbed in the material and excite a core level electron to an energy above the Fermi level. The XANES spectrum is a subset of the absorption spectrum measured within tens of eV above this absorption edge. This measurement probes the partial local density of states (PLDOS) into which the electron will be excited. At higher excitation energies, the resulting photoelectrons have a small amount of excess kinetic energy and a small wavelength, and can be backscattered by the atoms surrounding the emitting atom. The outgoing and the backscattered electron wavefunctions interfere constructively or destructively, depending on the electron wavelength, and this process itself will modify the absorption coefficient. The result is a series of oscillations on the high energy side of the absorption edge. This portion of the absorption spectra is referred to as the EXAFS signal, and gives direct information on bond lengths. A monochromatic tunable source of X-ray photons is necessary in order to scan the incident energy across the absorption edge, therefore, the use of synchrotron radiation is required for this type of spectroscopy. As an alternative to measuring the absorption of the excitation radiation through the material, X-ray fluorescence after the photoelectron relaxes was measured. This method permits the measurement of target elements in thin films.

The XAFS technique measures the X-ray absorption coefficient,  $\mu$  as a function of photon energy,  $E$ , above the absorption edge,  $E_0$  [117]. A photon with energy  $E = h\nu$  above energy  $E_0 = h\nu_0$  will release a photoelectron from the absorber atom with kinetic energy,  $E_K$ , where,

$$E_k = h\mathbf{n} - h\mathbf{n}_0 = \frac{\hbar^2 k^2}{2m}. \quad (4.7)$$

This photoelectron expands as a spherical wave and propagates with a wavelength  $2\mathbf{p}/k$  and has a probability for backscattering from neighboring atoms with a phase shift  $f_j(k)$ . The propagating electron coherently returns to the original atom interfering constructively or destructively with the original outgoing electron wave. As the energy increases, the wavelength decreases causing an alternating destructive and constructive interference. This changing interference pattern modulates the transition matrix element of the photon absorption process. The modulation in the absorption coefficient,  $\Delta\mathbf{m}$  for the K-edge spectra normalized to the isolated atomic background,  $\mathbf{m}_0$ , is known as the EXAFS component  $\mathbf{c}(k)$ , where [118],

$$\mathbf{c}(k) = \frac{\Delta\mathbf{m}}{\mathbf{m}_0} = -\sum_j \frac{S(k)N_j}{kr_j^2} |f_j(k, \mathbf{p})| \sin [2kr_j + \mathbf{j}_j(k)] e^{-2s_j^2 k^2} e^{-2r/I(k)} \quad (4.8)$$

where  $N_j$  is the number of nearest neighbors,  $k$  is the photoelectron wave vector,  $f_j$  is the scattering amplitude,  $S(k)$  is the amplitude reduction term due to many-body effects, and  $r_j$  is the radial distance from the absorbing atom.  $I(k)$  is the electron mean free path which is nearly proportional to  $k$ , allowing the exponential term to be approximated as  $e^{-2\gamma r/k}$  where  $\gamma$  is a constant. Mean square fluctuations in  $r_j$  are accounted for in the exponential Debye-Waller factor by  $s_j$ , and the term  $\mathbf{j}_j(k)$  accounts for the total phase of the curved wave scattering amplitude along the scattering trajectory [119]. A Fourier transform is used to convert the spectral data from  $k$ -space to  $R$ -space. Upon integrating, the Fourier transform gives a peak shift from the true value of  $R$ . The actual bond length can then be extracted by correcting this shift by using a system with known distances. The Fourier transform of  $\mathbf{c}(k)$  in momentum ( $k$ ) space gives a modified radial distribution function  $\mathbf{r}(r)$  in the distance ( $r$ ) space:

$$\mathbf{r}(r) = \frac{1}{4\mathbf{p}^{1/2}} \int_{k_{\min}}^{k_{\max}} k^n \mathbf{c}(k) e^{i2kr} dk. \quad (4.9)$$

A schematic of the XAFS experiment and process is shown in Figure 4.17(a). Synchrotron X-ray radiation is sent through a monochromator in order to tune the incident energy across the absorption edge. The monochromatic X-rays are then focused onto the sample and the resulting X-ray fluorescent signal is detected by a

liquid nitrogen cooled Ge detector. The first EXAFS experiment was the measurement of the In K-edge at 27.92 keV, detecting changes in the interference fringes resulting from the nearest neighbor atomic configuration around the In atom, as shown in Figure 4.17(b). Beamline BL01B1 at the Spring-8 synchrotron in Hyogo, Japan was used for this measurement. A drawing of the beamline is shown in Figure 4.18 and a close-up schematic of the X-ray focusing optics is shown in Figure 4.19. The beamline chosen was optimized for XAFS measurements and had a peak X-ray emission at around 30 keV (see Figure 4.20), almost the same energy as the In K-edge.

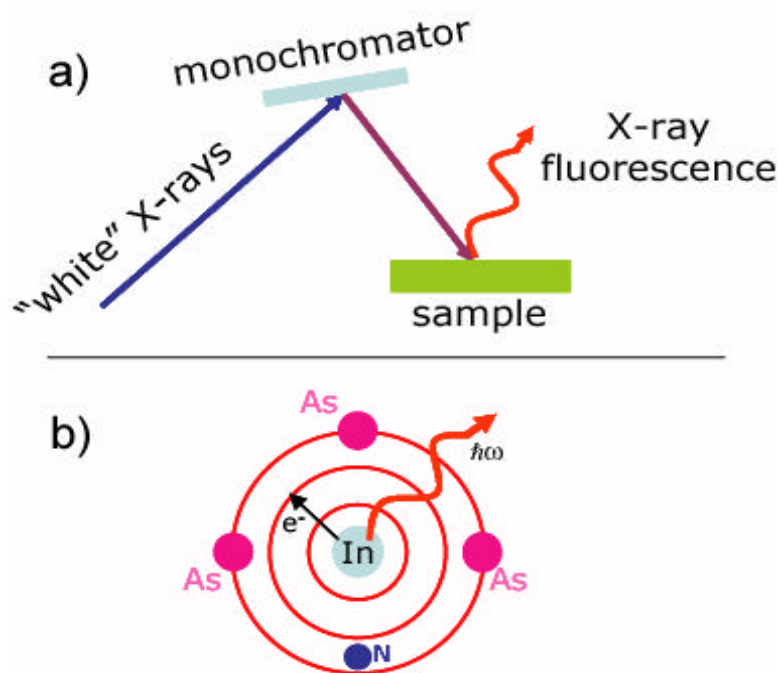


**Figure 4.17: (a) Schematic of an XAFS experiment, and (b) a drawing showing EXAFS interference of an emitted photoelectron based on nearest neighbor configuration and the subsequent fluorescent photon.**

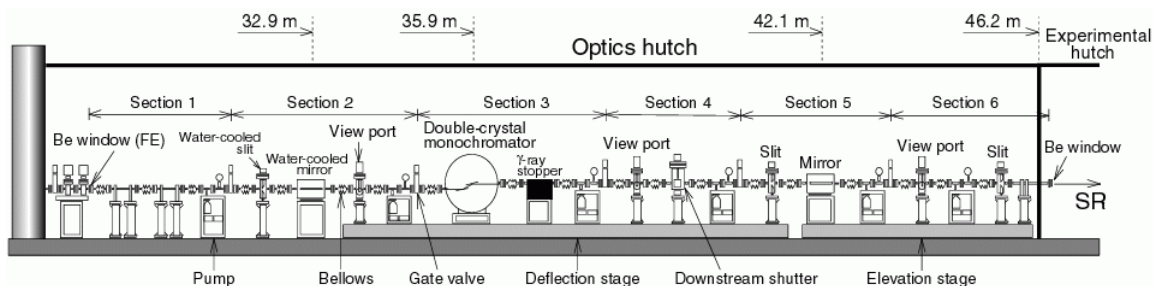


**Figure 4.18: The BL01B1 beamline at Spring-8 used for measuring the XAFS signal for the In K-edge [120].**

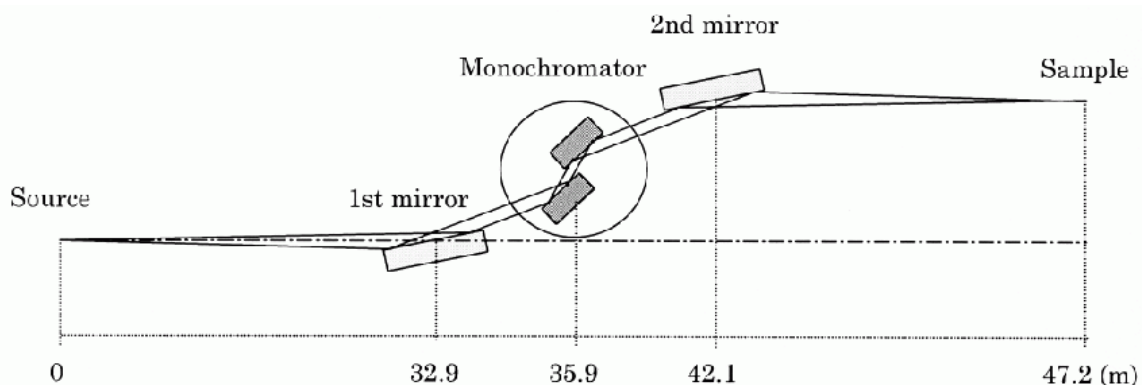


**Figure 4.19: The focusing optics and monochromator for the incident X-rays [120].**

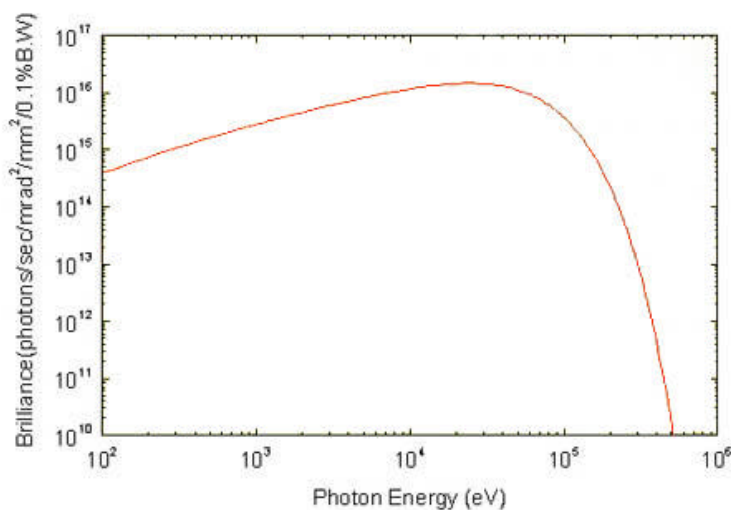


**Figure 4.20: Brilliance versus X-ray energy for the BL01B1 beam line. The In K-edge is at 27.92 keV [120].**

There are a few different ways to measure the XAFS signal. The first and most straightforward is X-ray absorption. Here a thin sample or powder is made and the attenuation of incident X-rays is measured. However, due to the small absorption length of around  $0.1 \mu\text{m}$  this technique does not work for a thin film on a thick substrate. The next technique, called “total yield,” measures the Auger electrons ejected from the sample. Total yield is a surface sensitive technique and works best with conducting samples. To measure insulating samples, the ejected photons, which are emitted after the backscattered electrons recombine, are instead measured from the

sample. The fluorescence detection method has better sensitivity for low concentrations than total yield and does not require a conducting sample.

The fluorescent XAFS signal from the In K-edge is shown in Figure 4.21. In this experiment, the incident X-ray energy was varied from 27.9 to 29 keV while the fluorescence was detected by a Ge photodetector. Plotted in Figure 4.21 is the integrated intensity of the fluorescence versus the incident X-ray energy. First a 500  $\mu\text{m}$  InAs sample was measured as a reference point for the InAs bond length. Then a 10 nm GaInNAs thin film with 30% In and 2% N with a post-anneal bandgap of 0.95 eV (1.3  $\mu\text{m}$ ) was measured before and after anneal. The sharp peak around the absorption edge is known as the XANES peak, while oscillations beyond that peak are considered the EXAFS fringes. The XANES peak was separated from the EXAFS fringes and the Fourier transform was taken [121,122]. After extensive filtering to remove the high frequency sampling noise from the data, the radial distribution function (RDF) was obtained, see Figure 4.22. The RDF plots the distance between the In atom and its neighbors; the first nearest neighbors are around 2.25  $\text{\AA}$  away. The RDF changes after anneal, suggesting the redistribution of atoms within the crystal beyond some statistically random distribution. While changes are small, they were reproducible among many samples with varied thickness and composition. The data suggests that the atoms are more closely spaced around the In for the annealed sample. This would correspond to more In-N bonds, which are shorter than In-As bonds. Modeling of the nearest neighbor bond lengths confirms that the number of In-N bonds increases after anneal [123]. One of the difficulties in this measurement is the high As to N ratio, which means the majority of the In atoms remain bonded to As atoms, reducing the experimental sensitivity to changes in In-N bonding. Also, second nearest neighbors could also have an effect on first nearest neighbors, since the redistribution of Ga and In may effect all bond lengths in the lattice.

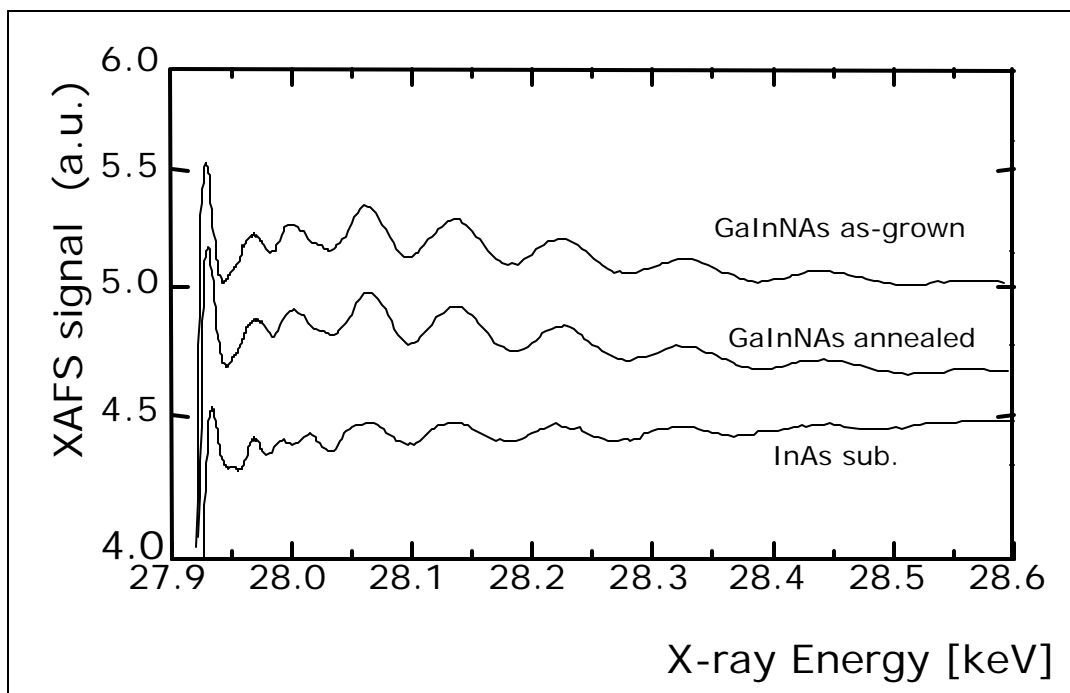


Figure 4.21: The fluorescence intensity from excited photoelectrons versus the incident X-ray beam energy for an InAs substrate and 10 nm GaInNAs films before and after anneal.

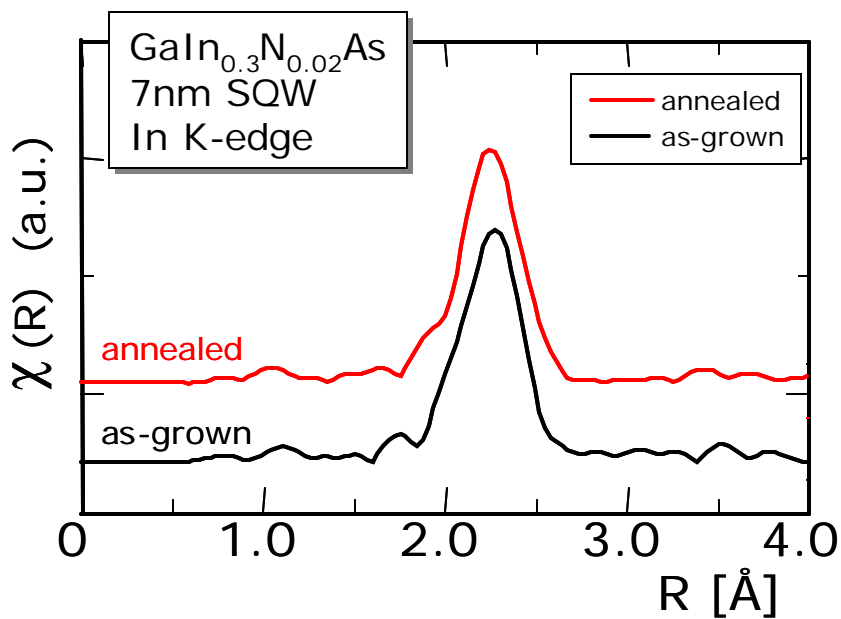


Figure 4.22: The radial distribution function for the In atom in the GaInNAs alloy before and after anneal.

Samples were also measured at the Lawrence Berkeley National Labs Advanced Light Source (ALS) using soft X-rays to measure the fine structure of the N absorption

edge. In this experiment 400 eV X-rays were used and fluorescence was detected with a superconducting tunnel junction (STJ) Nb detector with a 1.5 meV bandgap cooled to 0.1 K. This detector was used to improve the signal to noise ratio over traditional Ge detectors by more than an order of magnitude [124,125]. Measuring the N absorption edge however, posed even more problems than the In edge. First, N is in very dilute concentrations in the sample, and second there is an O absorption edge at 540 eV which limits the number of EXAFS oscillations that can be measured from the N edge at 400 eV. Furthermore, the absorption depth of the X-rays was 0.11  $\mu\text{m}$ , so only thicker films gave sufficient fluorescence. In order to reduce the O signal intensity, samples were As capped and placed in a vacuum desiccator during transportation, also, samples were measuring at grazing incidence angle for thinner samples. The N absorption edge in a 3000  $\text{\AA}$  GaInNAs film before and after anneal is shown in Figure 4.23. The signal is normalized to the XAFS signal from a 1500  $\text{\AA}$  film of GaNAs with the same concentration of N. Significant changes occur in the near edge of the N XANES signal. The absorption edge energy with the addition of In pushes the edge to lower energies, and by annealing, the edge shifts further. This suggests that the random orientation of nearest neighbors, including In, reduces the K-shell energy, and annealing increases the number of In neighbors around the N atoms. Energy band simulations were done to better relate changes in the N absorption edge with structural changes on anneal of the material. *Ab-initio* band structure models have calculated a random alloy of GaInNAs to have a smaller N K-shell energy than GaNAs, while increasing the In-N nearest neighbor bonds further reduces this energy [123]. Figure 4.24 presents the calculated data of the N edge energy with changing In-N coordination, relative to GaNAs. From the models, it is found that the increasing In-N bonds in the crystal reduces the N absorption edge energy. Table VI compares the calculated data with the experimentally determined data. The best fit between experiment and theory was that N was surrounded by two In atoms in the as-grown sample, and after anneal the In-N bonds increased by about one. This data also agrees with EXAFS data above taken from the In K-shell transition.

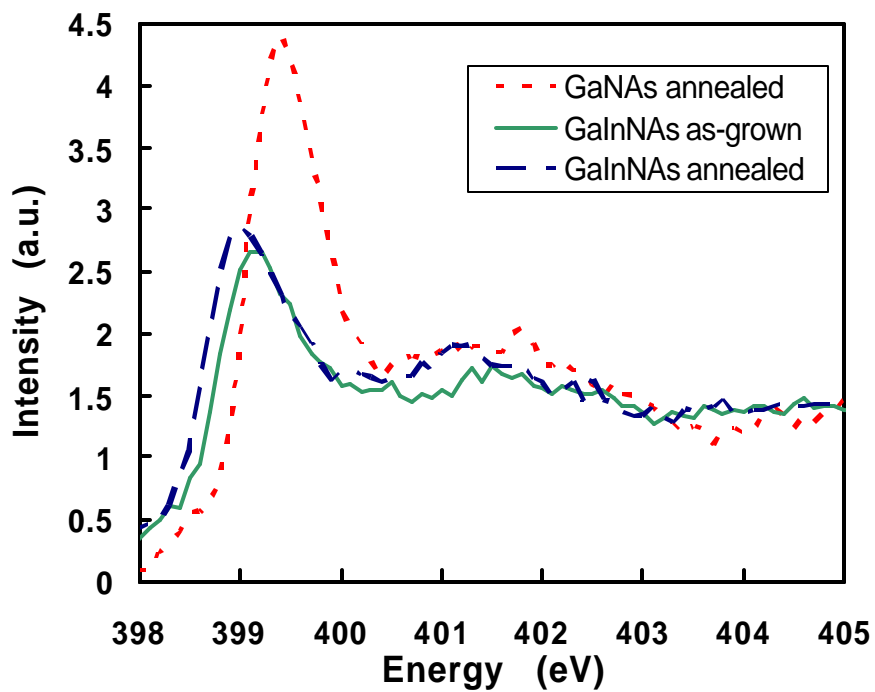


Figure 4.23: Normalized N XAFS spectrum for as grown and annealed 3000 Å GaInNAs samples with 15% In, and a GaNAs 1500 Å film, all with 1.5% N.

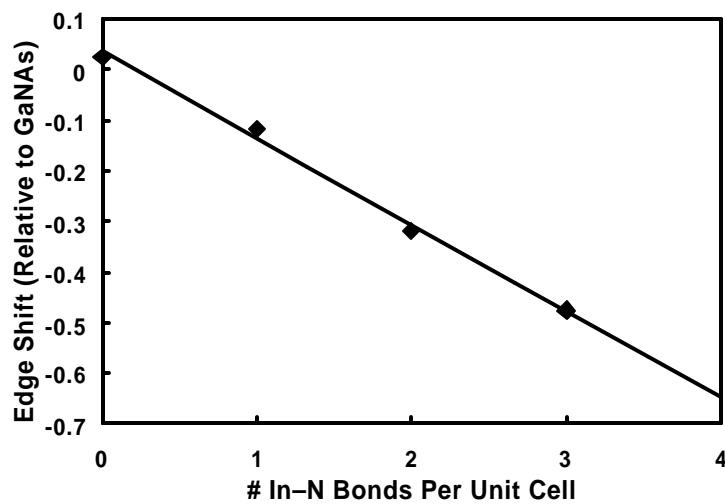


Figure 4.24: Nitrogen K-edge energy shift in GaInNAs with increasing In-N bonds. The energy shift is plotted relative to GaNAs [123].

**Table VI. Summary of N K-edge as modeled and measured experimentally. In the calculated vales changes which best match the experimentally determined values are tabulated.**

	N edge shift [eV]	
	Theory	Exp.
<b>GaNAs ® GaInNAs as grown no In ® 2 In-N</b>	-0.32	-0.3
<b>as grown ® anneal 1 In-N ® 2 In-N</b>	-0.2	-0.1
<b>2 In-N ® 3 In-N</b>	-0.16	

Figure 4.25 shows the statistical distribution of In-N bonds in GaInNAs alloy for a completely random crystal. For the samples measured with EXAFS above, the concentrations are most like the curve representing 30% In and 3% N. From the statistical findings for our composition, the most likely configuration is one In atom around each N atom in the crystal. This is what can be expected if the atoms incorporate in a random distribution, which may be expected during the low temperature growth. Next, the bandgap energy versus number of In-N bonds in the crystal was calculated in Figure 4.26 based on LDA simulations. From the bandgap calculations, the model shows that increasing the number of In-N bonds from one to three blueshifts the bandgap by over 100 meV. Finally, calculations also show that increasing the number of In-N bonds lowers the total energy of the crystal, shown in Figure 4.27. However, the strain energy increases with increased In-N coordination due to increasing the GaInNAs lattice parameter. While the strain energy increases by moving In toward N, a larger reduction in the electronic energy drives the short range ordering. Therefore, this driving force for energy reduction could increase the number of In-N bonds during a thermal anneal through atomic diffusion, which would blueshift the bandgap on the order of 100 meV, which is the same behavior seen when measuring the PL of annealed samples.

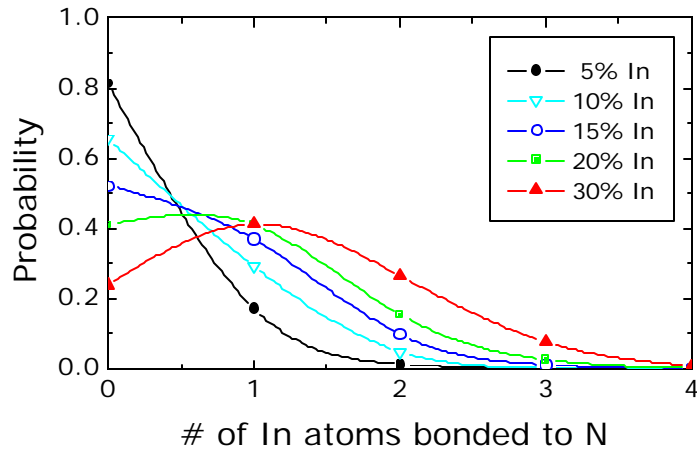


Figure 4.25: The statistical probability for the number of In-N bonds for different In compositions with 3% N in a completely random alloy [123].

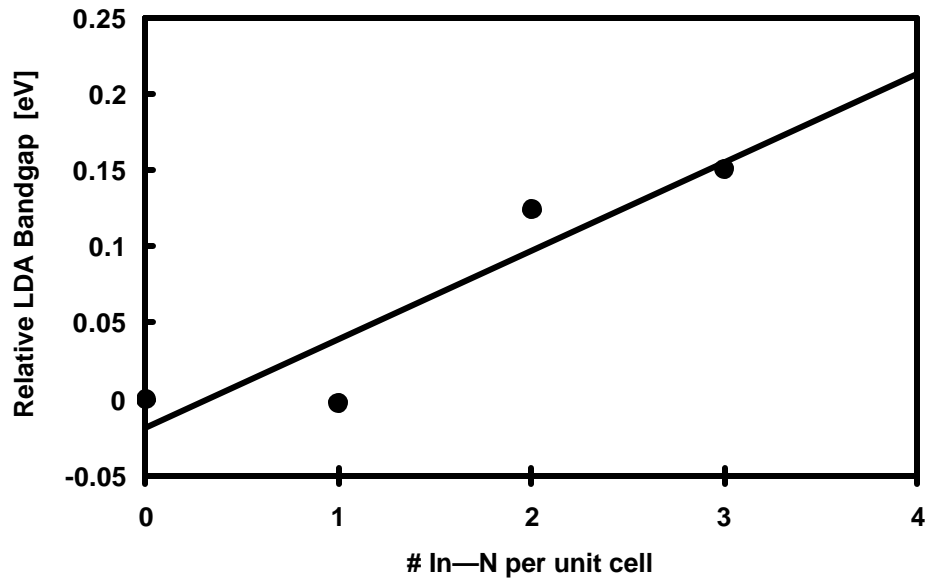


Figure 4.26: Bandgap shift by increasing the number of In-N bonds in the crystal using a local density approximation (LDA) simulation [123].

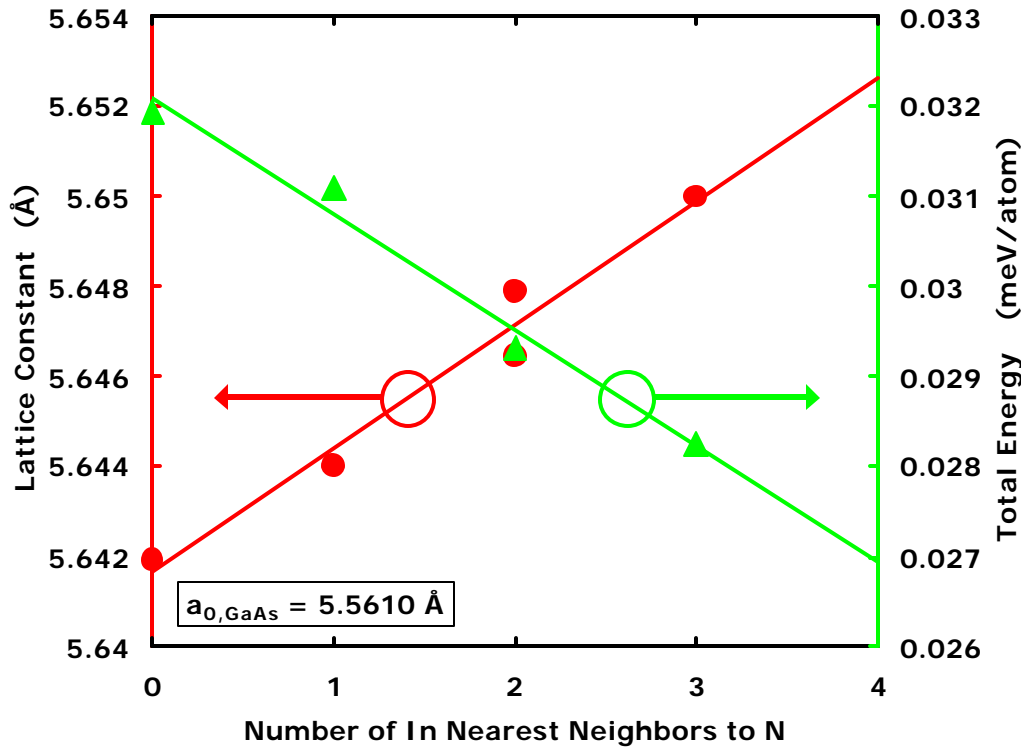


Figure 4.27: Lattice constant and total crystal energy in GaInNAs as a function of the number of In-N bonds [123].

### 4.3 Critical Thickness and Strain Compensation

GaInNAs quantum wells are typically grown near the critical thickness for dislocation formation. Because the N concentration is kept low to minimize defects, a great deal of In is added to obtain the longest possible wavelength. For high power devices, the amount of output power is proportional to the volume of the gain medium, or the number of quantum wells. Furthermore, in order to grow material with a bandgap longer than 1.3  $\mu\text{m}$ , more In and Sb are added to the quantum well, further increasing the layer strain and reducing the critical thickness. Figure 4.28 shows an (004) superlattice XRD rocking curve comparing three 8 nm quantum well GaInNAs and GaInNAsSb structures. From simulation of the diffraction pattern it was found that the (004) strain increased from 3.6% for a GaInNAs alloy with a bandgap of 1.3  $\mu\text{m}$  to 4.84% for a GaInNAsSb alloy with a 1.5  $\mu\text{m}$  bandgap. Because of this extra strain and

the need for increasing number of quantum wells, strain compensated barriers were grown between highly strained quantum wells.

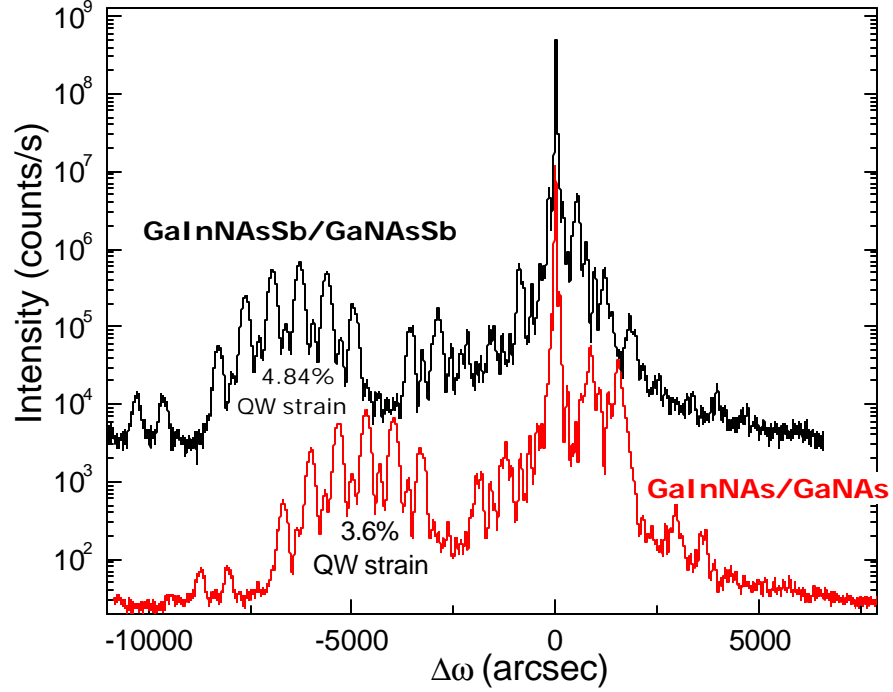


Figure 4.28: (004) XRD pattern from three QW GaInNAs/GaNAs and GaInNAsSb/GaNAsSb structures.

The Matthews and Blakeslee model [126] is typically used to calculate the critical thickness for a strained film. The critical thickness is given by:

$$h_c = \frac{b(1-\nu \cos^2 \mathbf{q})}{8\rho(1+\nu)\mathbf{e} \cos \mathbf{l}} \ln\left(\frac{\mathbf{a}h_c}{b}\right) \quad (4.10)$$

where  $b$  is the Burgers vector,  $\nu$  is the Poisson ratio,  $\mathbf{q}$  is the angle between the Burgers vector and the dislocation line,  $\mathbf{e}$  is the linear strain between the film and substrate,  $\mathbf{l}$  is the angle between the Burgers vector and the normal to the dislocation line direction in the interface, and  $\mathbf{a}$  is a factor which accounts for the dislocation core energy. For cubic III-V semiconductors, the most commonly observed dislocation is along the [114] slip plane with a Burgers vector of  $1/2[110]$ . Therefore, the length of the Burgers vector is

$$b = \frac{a}{\sqrt{2}}, \quad (4.11)$$

and  $\mathbf{q}$  is  $60^\circ$ . The constant  $\alpha$  in equation 4.10 is 4 in GaAs, and for a dislocation at the (110) interface,  $\cos I=0.5$ . The linear strain  $\mathbf{e}$  is defined as

$$\mathbf{e} = \frac{a_f - a_s}{a_f}. \quad (4.12)$$

where  $a_f$  and  $a_s$  is the in-plane lattice parameters for the film and substrate, respectively. Typically, the Matthews and Blakeslee model underestimates the real critical thickness found experimentally, and several models have been developed which better predict actual critical thickness by taking into account the kinetics of misfit dislocation formation [127].

Traditional strain compensation in GaAs based alloys is done with tensile GaAsP [128]. However, the GaAsP ternary has a larger bandgap and would block carriers from the quantum wells if placed near the active region. The GaNAs ternary has many advantages for use as a strain compensation layer with long wavelength GaInNAs quantum wells. The primary use of GaNAs barriers is tensile strain compensation. In fact the XRD samples in Figure 4.28 were grown with strain compensation N-As barriers. The tensile barriers can be observed in the diffraction plot at angles larger than the GaAs substrate peak. The thickness of the tensile GaNAs barriers compensating the strain from the quantum wells can be calculated as follows [61]. First the lattice parameter of the  $\text{Ga}_x\text{In}_{1-x}\text{N}_y\text{As}_{1-y}$  quantum well with thickness  $t_{\text{QW}}$  can be calculated using Vegard's law as:

$$a_{\text{Ga}_x\text{In}_{1-x}\text{N}_y\text{As}_{1-y}} = (1-y)xa_{\text{GaAs}} + (1-y)(1-x)a_{\text{InAs}} + yxa_{\text{GaN}} + y(1-x)a_{\text{InN}}. \quad (4.13)$$

Assuming that the  $\text{Ga}_x\text{In}_{1-x}\text{N}_y\text{As}_{1-y}$  layer is not relaxed, the strain is defined as:

$$\mathbf{e} = \frac{a_{\text{Ga}_x\text{In}_{1-x}\text{N}_y\text{As}_{1-y}} - a_{\text{GaAs}}}{a_{\text{Ga}_x\text{In}_{1-x}\text{N}_y\text{As}_{1-y}}}. \quad (4.14)$$

The  $\text{GaN}_z\text{As}_{1-z}$  barrier composition is related to the  $\text{Ga}_x\text{In}_{1-x}\text{N}_y\text{As}_{1-y}$  composition with the relation,

$$z = \frac{y}{x}, \quad (4.15)$$

since the N composition is inversely proportional to the group-III concentration due to the incorporation dependence of the plasma. The barrier thickness should then be,

$$t = \frac{2t_{QW}(ya_{GaN} + (x-y)a_{GaAs})(1-y)xa_{GaAs} + (1-y)(1-x)a_{InAs} + yxa_{GaN} + y(1-x)a_{InN} - a_{GaAs}}{3y(a_{GaN} - a_{GaAs})(1-y)xa_{GaAs} + (1-y)(1-x)a_{InAs} + yxa_{GaN} + y(1-x)a_{InN}}, \quad (4.16)$$

for the case of three barriers and two quantum wells.

The second advantage to GaNAs barriers was previously described in section 4.2.3. Some contribution to the blueshift on anneal could be the out-diffusion of N from the quantum wells and with high N GaNAs barriers between GaInNAs layers, N would diffuse into the quantum wells instead of out, or at least limit the out diffusion. The third advantage, which also in some cases may be a disadvantage, is the reduction in quantum confinement using smaller bandgap GaNAs barriers. Figure 4.29 shows the PL spectra of two GaInNAs samples, one with 20 nm GaAs barriers and one with 20 nm GaNAs barriers. The composition of the quantum wells are exactly the same. Due to smaller quantum confinement between GaNAs and GaInNAs, the first bound level is at a longer wavelength. Furthermore, from this measurement it can be seen that by using GaNAs the blueshift is reduced since less N is removed from the quantum wells. Table VII summarizes this PL data and shows that using GaNAs barriers the luminescence shifts to longer wavelengths and the bandgap shift is smaller after anneal.

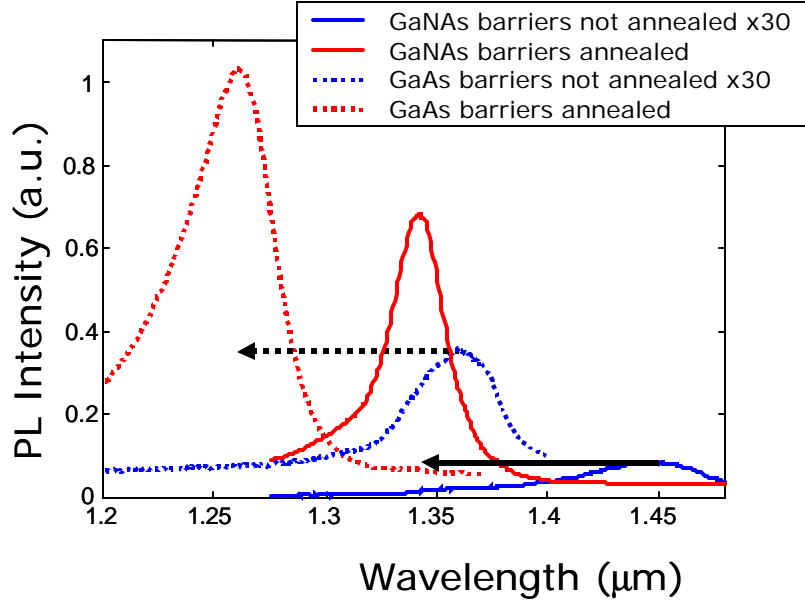


**Figure 4.29:** PL from as-grown and anneal GaInNAs, with and without GaNAs barriers. The composition of the quantum wells where the same for both samples [61].

**Table VII.** PL energy difference between as-grown and annealed GaInNAs quantum wells with and without GaNAs barriers.

	GaAs barriers	GaNAs barriers
<b>As-grown</b>	1.36 $\mu\text{m}$	1.44 $\mu\text{m}$
<b>Annealed</b>	1.26 $\mu\text{m}$	1.34 $\mu\text{m}$
<b>Energy shift</b>	73 meV	64 meV

While longer wavelength operation is gained with less confinement, the tradeoff is that the carriers may not be as well confined to the active region and there may be some sacrifice in the high temperature stability of a device based on this structure. At this time, the effect of GaNAs barriers on temperature stability in laser structures has not been carefully studied. Another disadvantage to using GaNAs barriers is that N deposition incorporates non-radiative defects in the material. This is evident in the increased anneal time necessary for structures grown with GaNAs barriers. However, the effect of possible defects in the barriers on PL and device performance is not yet known.

With the goal of high-power device structures, multiple strained quantum wells were grown with tensile compensated GaNAs barriers. Figure 4.30 shows luminescence of three, six and nine quantum well PL samples grown with GaNAs barriers. As the number of quantum wells increased, the PL intensity scaled linearly. A cross section TEM sample was made from the nine quantum well sample and was shown previously in section in Figure 4.16. From the TEM image it can be seen that dislocation free quantum wells were grown with this strain compensated structure. Without the tensile barriers no more than three quantum wells could be grown before the material relaxed and the PL intensity dropped below detectable levels.

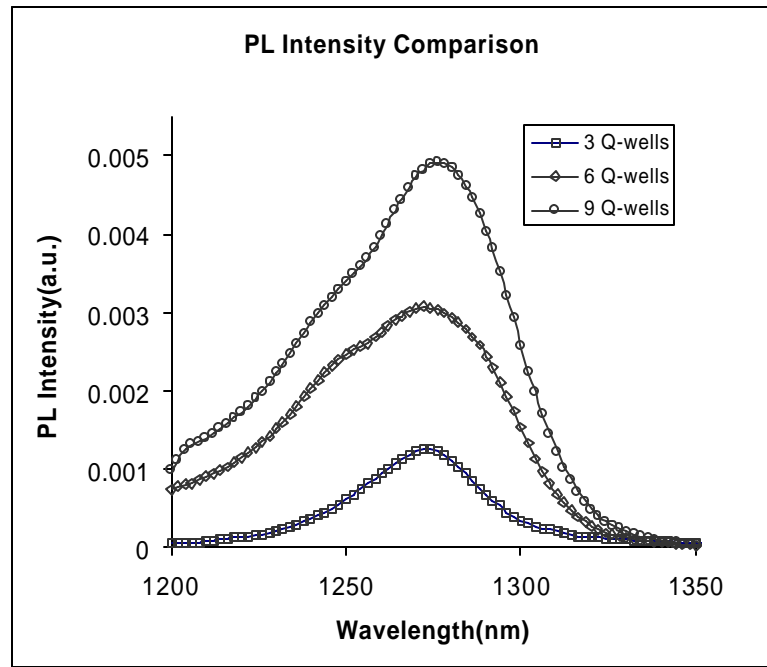


**Figure 4.30: PL spectra for 3, 6, and 9 GaInNAs QWs with tensile strain compensated GaNAs barriers.**

## Chapter 5: GaInNAs(Sb) Lasers

The purpose of this chapter is to report on laser devices grown with the dilute nitride active region and based on material characterized by PL. Much of the work presented in this chapter is a direct result of the work of my colleagues who were responsible for device fabrication and testing. First is an overview of a GaInNAs-based long wavelength VCSELs which was grown and fabricated by Chris Coldren and Mike Larson. Next, edge emitting lasers, based on GaInNAs and GaInNAsSb, fabricated by Wonill Ha, are presented.

### 5.1 GaInNAs Long Wavelength VCSELs

Lasers based on GaInNAs active regions have been grown and fabricated. The first VCSEL was designed for substrate emission at 1230 nm with an active region of three 70 Å GaInNAs quantum wells separated by 200 Å GaAs barriers embedded in a one wavelength cavity. The *p*-mirror doping was reduced below normal 850 nm VCSEL levels in a trade-off for higher reflectivity and lower threshold current at the expense of a higher voltage drop at each mirror interface [129]. The upper Be doped mirror consisted of 20 pairs total of AlAs/GaAs quarter wave layers with a hole concentration of  $5 \times 10^{17} \text{ cm}^{-3}$  for the first 10 periods and  $1 \times 10^{18} \text{ cm}^{-3}$  for the final 10 periods. A gold contact layer was deposited on the top mirror serving to increase the overall reflectivity, thus making a bottom-emitting device. Selective wet oxidation of three AlAs layers closest to the active region in the *p*-type DBR mirror was used to provide a current confining aperture. The devices were mounted without heat sinking on a glass slide for optical emission through the substrate.

The output power and voltage vs. injection current for a  $5 \times 5 \text{ }\mu\text{m}^2$  device operating CW at room temperature are shown in Figure 5.1(a). The threshold current is approximately 1.3 mA and the slope efficiency is 0.045 W/A. The conservative doping

profile in the  $p$ -mirror to minimize free carrier absorption resulted in a threshold voltage of 10.3 V. This large voltage drop created a large degree of self-heating, limiting the maximum output power to 8  $\mu$ W at 3.8 mA. The fact that cw operation was possible in spite of this excess power dissipation is indicative of the high gain and low temperature sensitivity of the GaInNAs MQW active region. Figure 5.1(b) shows the emission spectra just above threshold with a lasing wavelength of 1201 nm. At 2.6 times threshold, the emission shifts to 1205 nm. The spectra indicate the device lased in a single transverse and longitudinal mode, even far above threshold, with a side mode suppression ratio greater than 40 dB. Using a wavelength shift with temperature of 0.0743 nm/K obtained from pulsed VCSELs, this indicates a temperature rise of approximately 60°C above ambient temperature at the peak output power. CW laser operation was obtained for devices with square sides between 3.6 and 6.4  $\mu$ m, with threshold currents from 0.94 to 2.3 mA, respectively and a slope efficiency as high as 0.049 W/A. These devices were far from optimum because little band/doping engineering was possible in these conventional mirrors because the MBE system did not have a C doping source, hence we were limited in the range and ability to maintain abrupt doping profiles with Be because of its propensity to diffuse at high concentrations. Furthermore, with only one Al and one Ga source available at the time, no grading of the GaAs/AlAs junctions was possible.

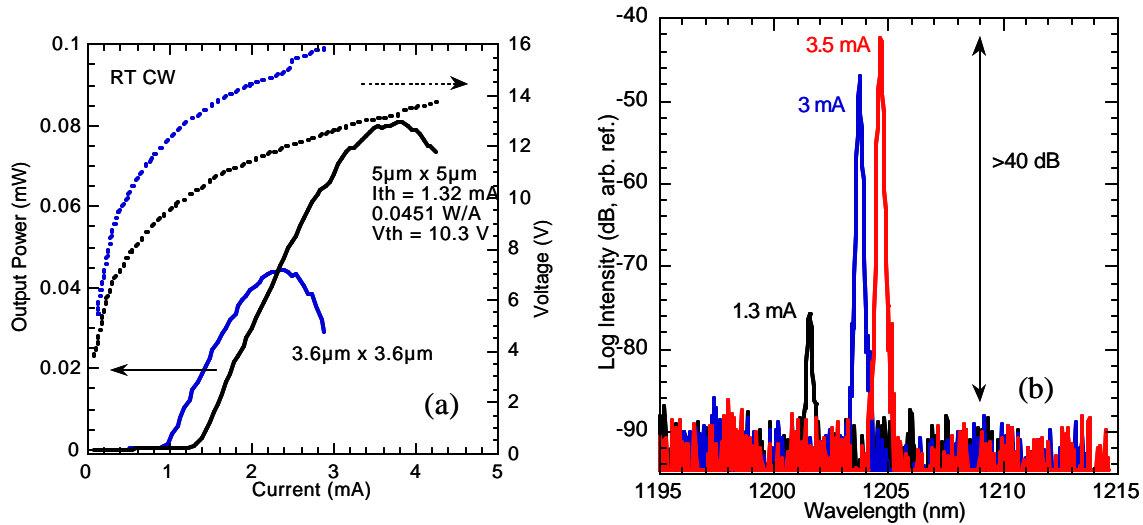


**Figure 5.1: (a) Light output power and voltage vs. injection current (L-I-V) characteristic under room temperature continuous wave operation for  $3.6 \times 3.6 \mu\text{m}^2$  and  $5 \times 5 \mu\text{m}^2$  VCSELs. (b) Emission spectra at 1.3 mA ( $\sim I_{th}$ ) and 3.5 mA ( $\sim 2.6 I_{th}$ ) for a  $5 \times 5 \mu\text{m}^2$  GaInNAs oxide confined VCSEL.**

## 5.2 GaInNAsSb High Power Edge Emitting Lasers

High power (>500 mW) single mode lasers are highly desirable as pumps for Raman fiber amplifiers and many non-linear channel switching applications in optical networks. While VCSELs at 1.3  $\mu\text{m}$  will be extremely useful for MANs and LANs, Raman pump lasers must work at 1.45  $\mu\text{m}$  to be useful in combination with EDFAs at 1.55  $\mu\text{m}$ . In order to provide fiber amplifiers over the entire low loss fiber region, pump lasers must provide high power over the entire 1.2-1.5  $\mu\text{m}$  range.

Separate confinement heterojunction (SCH) multiple quantum well lasers were grown on (100) *n*-GaAs substrates. The active region consists of three 7 nm GaInNAsSb quantum wells separated by 20 nm GaNAsSb barriers. The active region is symmetrically embedded between 120 nm thick undoped GaAs waveguides. A 1.8  $\mu\text{m}$  Si doped ( $5 \times 10^{18} \text{ cm}^{-3}$ ) *n*-type bottom cladding layer was grown below the active region with a 1.7  $\mu\text{m}$  Be doped ( $2 \times 10^{18} \text{ cm}^{-3}$ ) *p*-type top cladding. A 50 nm *p+* ( $1 \times 10^{19} \text{ cm}^{-3}$ ) GaAs cap layer was grown for metallization. The samples were then post-growth

annealed at 720°C for 2 minutes by RTA [130]. All lasers were tested under pulsed conditions of 1  $\mu$ s with a 1% duty cycle because they were not heat sunk.

Ridge waveguide lasers were fabricated with 5  $\mu$ m wide and 800  $\mu$ m long ridges with cleaved uncoated end facets and 3 GaInNAsSb quantum wells and GaNAsSb barriers. An SEM image was taken of the wafer after fabrication and Figure 5.2(a) shows three 5, 10, and 20  $\mu$ m mesa lasers with a close up of the 5  $\mu$ m laser in Figure 5.2(b). Figure 5.3(a) shows the light output power versus injection current, and Figure 5.3(b) the spectrum at 1.465  $\mu$ m with a maximum power of exceeding 70 mW and a slope efficiency of 0.21 W/A. The minimum threshold current density was 2.8 kA/cm<sup>2</sup> or 930 A/cm<sup>2</sup> per quantum well. This is by far the lowest reported threshold current density for lasers with GaInNAs quantum wells beyond 1.4  $\mu$ m on a GaAs substrate. However, this threshold is still ~2 times higher and the slope efficiency 2 times poorer than our best lasers at 1.39  $\mu$ m [130], indicating that while substantial improvements have been achieved by the addition of Sb, the long wavelength material is still not as good as the shorter wavelength material.

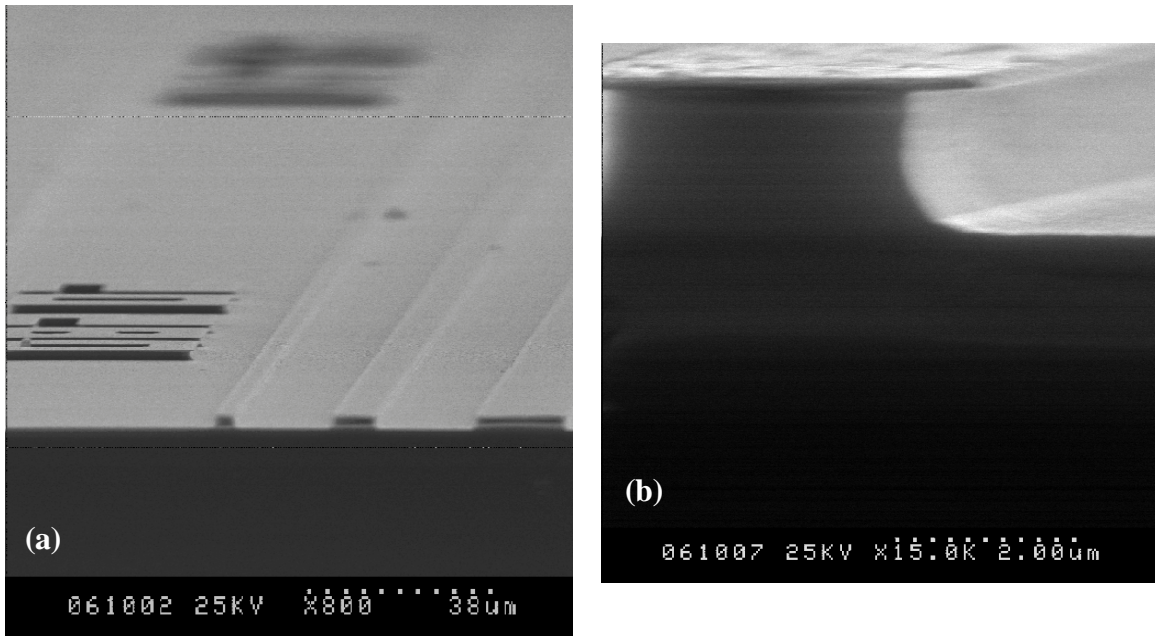


**Figure 5.2: (a) SEM image of 3 ridge waveguide lasers, of 5, 10 and 20  $\mu$ m mesa structures. (b) Close up of the 5  $\mu$ m laser.**

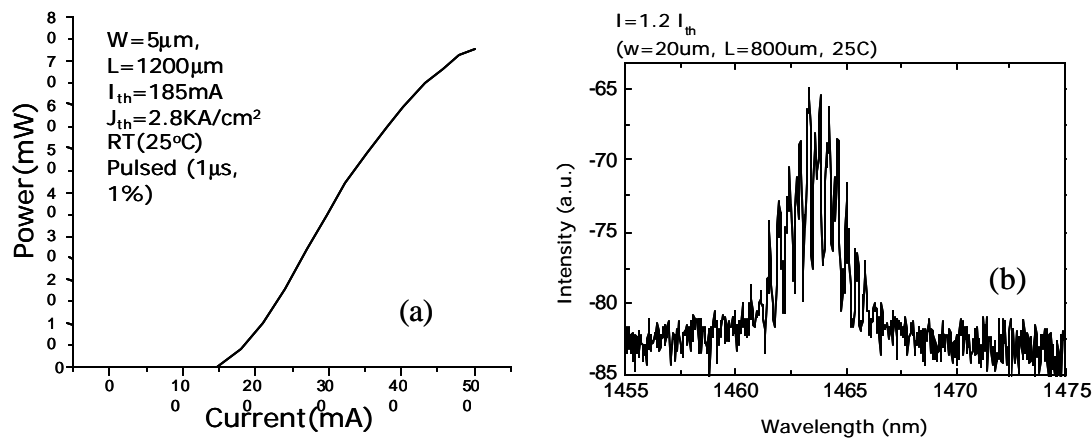


**Figure 5.3: (a) Light output power vs. injection current (L-I) characteristic for 5  $\mu\text{m}$  wide ridge waveguide edge emitting GaInNASb laser under room temperature pulsed operation. (b) Emission spectra at 200 mA ( $\sim 1.2 I_{th}$ ) under pulsed operation at room temperature.**

Ridge waveguide lasers with 46% In and 2.5% N of GaInNASb quantum wells and GaNASb barriers were also grown and fabricated. The Sb flux during growth of the active region was  $1.4 \times 10^{-7}$  Torr which was calibrated in other samples to be an Sb concentration of around 3-4%. The light output power versus injection current for the 10  $\mu\text{m}$  wide and 660  $\mu\text{m}$  long mesa in-plane laser is shown in Figure 5.4(a) while the emission spectrum at 1.2 times threshold is shown in Figure 5.4(b). Emission was found to be at 1.49  $\mu\text{m}$ . Further information about laser performance can be found in previous publications [131]. Lasers with emission at 1.55  $\mu\text{m}$  and superior performance should be possible with further optimization of the In, N, and Sb compositions, growth temperature and annealing conditions.

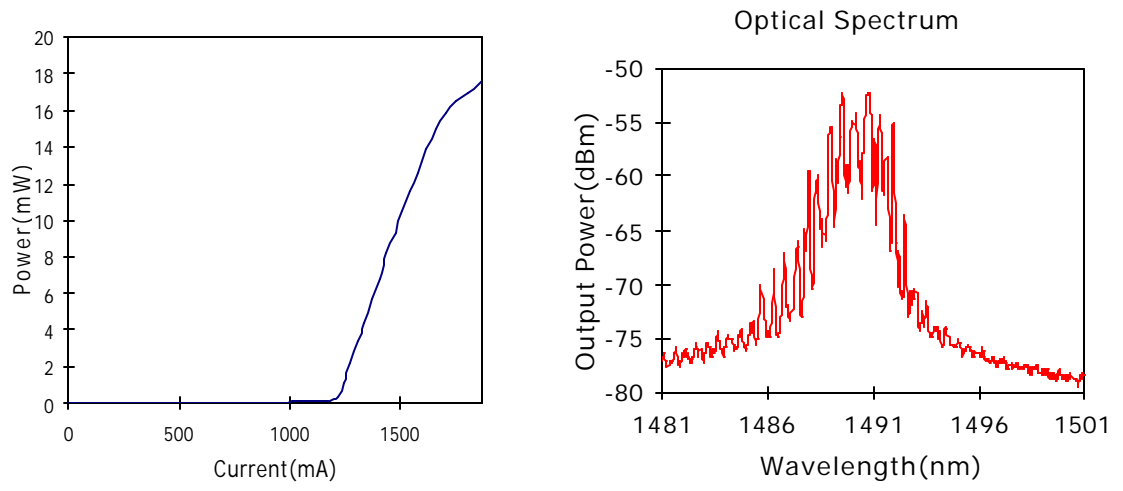


**Figure 5.4: (a) L-I for a 3 QW GaInNAsSb ridge waveguide edge emitting laser. (b) Emission spectra at  $1.2 I_{th}$  for same device.**

# Chapter 6: Conclusions and Future Work

## 6.1 Conclusions

Dilute N GaInNAs was grown by MBE using a N RF plasma source. While the solubility of N in GaAs is extremely low, by growing under metastable conditions such as low substrate temperatures, high As overpressures, and using a reactive radical N source, high concentrations of N can be incorporated in the crystal. This growth differs greatly from traditional III-V growth and steps have to be taken to optimize growth conditions to minimize defects. There are many parameters controlling the plasma properties, and damage from the plasma from species, such as ions and high energy neutrals, must be minimized.

The large degree of bandgap bowing by adding N to GaAs can be better explained as an isoelectronic impurity level rather than true alloying. Nitrogen does not readily alloy with GaAs due to dissimilar properties, such as bond lengths and electronegativity. In one theoretical model, the N level exists above the conduction band and anticrosses with the GaAs de-localized conduction band. This is a favorable device property since most of the bandgap reduction is in the conduction band which better confines the light electrons at higher temperatures.

Unfortunately, as-grown GaInNAs does not have very strong PL due to defects incorporated from the plasma, the low temperature growth, and possibly the basic thermodynamics of this system. Thermal anneal after growth dramatically improves radiative efficiency, but at the same time, blueshifts the luminescence. Some type of atomic rearrangement is the most likely reason for the intensity increase and bandgap change on anneal. A likely reason for the PL increase is the removal of point defects which cause non-radiative deep level defects in the material. Bandgap changes can be best explained by some degree of phase segregation and a change in the short range order. There is evidence of an increased presence of the In-N bond above the statistical

average for the random alloy, which has been modeled to increase the bandgap. Another change in the material on anneal is the change in uniformity. CL studies exhibit non-uniform luminescence on a micron scale which tends to improve on anneal.

Recently, a new component, Sb, has been added to the GaInNAs alloy to further reduce the bandgap. Not only does Sb incorporate into GaInNAs but it acts as a surfactant, reducing the surface energy during growth and improves uniformity by increasing surface mobility. The GaInNAs alloy has bright emission out to about 1.3  $\mu\text{m}$  but the GaInNAsSb alloy can have high intensity PL out to 1.6  $\mu\text{m}$ . Only a small addition of Sb is necessary to shift the bandgap to much longer wavelengths. It is suggested that In on the group-III lattice site pushes the conduction band away from the N related level, reducing the effect of N on bandgap reduction. While Sb on the group-V site can shift the conduction band towards the N resonant level, further increases N effects of the bandgap. Furthermore, even though the longer wavelength GaInNAsSb has increased In and Sb has been added, the uniformity improves on the micron scale, as seen with CL.

Finally, using the GaInNAs active region, VCSELs and edge emitting lasers were grown and fabricated. Low threshold GaInNAsSb edge emitting lasers were fabricated at 1.46  $\mu\text{m}$ , and with even more Sb, lasers were grown with laser emission as long as 1.49  $\mu\text{m}$ .

## **6.2 Future Work**

A great deal of material analysis still needs to be done to further understand the complicated properties of the GaInNAsSb alloy. Some of the mysteries which still remain include the true origin of the blueshift and intensity improvement on anneal, the reasons for the non-uniform luminescence, and the source of defects in the material which reduce efficiency at longer wavelengths with the addition of either In and N. Better plasma operation and ways to increase the growth temperature may play a significant role in material quality improvements. Enhancing the role of Sb as a surfactant with optimized cracking and vapor pressure may also help reduce defects in the alloy. With further optimization of the material, device design and thermal

annealing, high-power, high-efficiency VCSELs can be grown with the GaInNAsSb active region at the important telecommunication wavelength of 1.55  $\mu\text{m}$ .

## Chapter 7: References

- [1] A. F. Phillips, S. J. Sweeney, A. R. Adams, and P. J. A. Thijs, "The temperature dependence of 1.3 and 1.55 $\mu\text{m}$  compressively strained InGaAs(P) MQW semiconductor lasers," *IEEE J. Select. Topics Quantum Electron.*, vol. 5, pp. 301-352, 1999.
- [2] C. W. Coldren, M. C. Larson, S. G. Spruytte, and J. S. Harris Jr., "1200nm GaAs based vertical cavity lasers employing GaInNAs multiple quantum well active region," *Electron. Lett.*, vol. 36, no. 11, pp. 951-952, May 25, 2000.
- [3] S. Sato, Y. Osawa, T. Saitoh, and I. Fujimura, "Room-temperature pulsed operation of 1.3 $\mu\text{m}$  GaInNAs/GaAs laser diode," *Electron. Lett.*, vol. 33, no. 16, pp. 1386-1387, July, 1997.
- [4] M. R. Gokhale, P. V. Studentkov, J. Wei, and S. R. Forrest, "Low threshold current, high efficiency 1.3 $\mu\text{m}$  wavelength aluminum-free InGaAsN-based quantum-well lasers," *IEEE Photon. Tech. Lett.*, vol. 12, pp. 131-133, 2000.
- [5] M. Kondow, K. Uomi, A. Niwa, T. Kitantai, S. Watahiki, and Y. Yazawa, "GaInNAs: A Novel Material for Long-Wavelength-Range Laser Diodes with Excellent High-Temperature Performance," *Jpn. J. Appl. Phys.*, vol. 35, no. 2B, pp. 1273-1275, Feb., 1996.
- [6] M. O. Fischer, M. Reinhardt, and A. Forchel, "Room-temperature operation of GaInAsN-GaAs laser diodes in the 1.5- $\mu\text{m}$  range," *IEEE J. Select. Topics Quantum Electron.*, vol. 7, no. 2, pp. 149-151, Mar., 2001.
- [7] H. Shimizu, K. Kumada, S. Uchiyana, and A. Kasukawa, "High-performance CW 1.26 $\mu\text{m}$  GaInNAsSb-SQW ridge lasers," *IEEE J. Select. Topics Quantum Electron.*, vol. 7, no. 2, pp. 355-364, Mar., 2001.
- [8] X. Yang, M. J. Jurkovic, J. B. Heroux, and W. I. Wang, "Molecular beam epitaxial growth of InGaAsN:Sb/GaAs quantum wells for long-wavelength

- semiconductor lasers," *Appl. Phys. Lett.*, vol. 75, no. 2, pp. 178-180, July 12, 1999.
- [9] T. H. Maiman, "Stimulated Optical Radiation in Ruby," *Nature*, vol. 187, no. 4736, pp. 493-494, Sept. 6, 1960.
- [10] T. H. Maiman, *Brit. Commun. Electron.*, vol. 1, pp. 674, 1960.
- [11] I. Melngailis, "Longitudinal injection-plasma laser of InSb," *Appl. Phys. Lett.*, vol. 6, no. 3, pp. 59-60, 1965.
- [12] Potter, R., "Surface Emitting Lasers." MPhil Dissertation, University of Essex, 1998.
- [13] Z. I. Alferov, V. M. Andreyev, S. A. Gurevich, R. F. Kararinov, V. R. Larionov, M. N. Mizerov, and E. L. Portnoy, "Semiconductor lasers with the light output through the diffraction grating on the Surface of the waveguide layer," *IEEE J. Quantum Electron.*, vol. QE-11, pp. 449-451, 1975.
- [14] R. D. Burnham, D. R. Scifres, and W. Striefer, "Single-heterostructure distributed feedback GaAs diode lasers," *IEEE J. Quantum Electron.*, vol. QE-11, pp. 439-449, 1975.
- [15] H. Soda, K. Iga, C. Kitahara, and Y. Suematsu, "GaInAsP/InP Surface Emitting Injection Laser," *Jpn. J. Appl. Phys.*, vol. 18, pp. 2329-2330, 1979.
- [16] A. Chailertvanitkul, S. Uchiyama, Y. Kotaki, Y. Kokobun, and K. Iga, 1983, Annual Meeting Japanese Society Applied Physics.
- [17] I. Ibaraki, S. Ishikawa, S. Ohkouchi, and K. Iga, *Electron. Lett.*, vol. 20, pp. 420, 1984.
- [18] G. M. Yang, M. H. MacDougal, and P. D. Dapkus, "Ultralow threshold current vertical-cavity surface-emitting lasers obtained with selective oxidation," *Electron. Lett.*, vol. 31, no. 11, pp. 886, 1995.
- [19] K. S. Giboney, L. R. Aronson, and B. E. Lemoff, "The ideal light source for datanets," *IEEE Spectrum*, vol. 35, pp. 43-53, 1998.
- [20] Courtesy of John E. Bowers, UCSB.
- [21] J. S. Harris Jr., "GaInNAs long-wavelength lasers: progress and challenges," *Semicond. Sci. Technol.*, vol. 17, pp. 880-891, 2002.

- [22] J. Hecht, *Understanding Fiber Optics*. Upper Saddle River, NJ: Prentice Hall, 2002.
- [23] G. Patriarche, F. Jeannes, J. Oudar, and F. Glas, "Structure of the GaAs/InP interface obtained by direct wafer bonding optimised for surface emitting optical devices," *J. Appl. Phys.*, vol. 82, pp. 4892-4903, 1997.
- [24] L. Goldstein, C. Fortin, C. Starck, A. Plais, J. Jacquet, J. Boucart, A. Rocher, and C. Poussou, "GaAlAs/GaAs metamorphic Bragg mirror for long wavelength VCSELs," *Electron. Lett.*, vol. 34, pp. 268-270, 1998.
- [25] S. Uchiyama and S. Kashiwa, "GaInAsP/InP SBH surface emitting lasers with Si/Al<sub>2</sub>O<sub>3</sub> mirror," *Electron. Lett.*, vol. 31, pp. 1449-1451, 1995.
- [26] M. Yano, H. Imai, and M. Takusagawa, "Analysis of threshold temperature characteristics for InGaAsP/InP double heterojunction lasers," *J. Appl. Phys.*, vol. 52, no. 5, pp. 3172-3175, May, 1981.
- [27] N. K. Dutta and R. J. Nelson, "Temperature dependence of threshold of InGaAsP/InP double-heterostructure lasers and Auger recombination," *Appl. Phys. Lett.*, vol. 38, no. 6, pp. 407-409, Mar. 15, 1981.
- [28] M. Yamada, T. Anan, K. Tokutome, A. Kamei, K. Nishi, and S. Sugou, "Low-threshold operation of 1.3  $\mu\text{m}$  GaAsSb quantum well lasers directly grown on GaAs substrates," *IEEE Photon. Tech. Lett.*, vol. 12, pp. 774-776, 2000.
- [29] J. A. Lott, N. N. Ledentsov, V. Ustinov, A. Maleev, A. Zhukov, A. Kovsh, M. Maximov, B. Volovik, Z. Alferov, and D. Bimberg, "InAs-InGaAs quantum dot VCSELs on GaAs substrates emitting at 1.3  $\mu\text{m}$ ," *Electron. Lett.*, vol. 36, pp. 1384-1386, 2000.
- [30] T. Kitatani, M. Kondow, T. Kikawa, Y. Yazawa, M. Okai, and K. Uomi, "Analysis of Band Offset in GaNAs/GaAs by X-Ray Photoelectron Spectroscopy," *Jpn. J. Appl. Phys.*, vol. 38, pp. 5003-5006, 1999.
- [31] P. Krispin, S. Spruytte, J. S. Harris, and K. Ploog, "Electrical depth profile of p-type GaAs/Ga(As,N) heterostructures determined by capacitance-voltage measurements," *J. Appl. Phys.*, vol. 88, pp. 4153, 2000.

- [32] T. Kitatani, K. Nakahara, M. Kondow, K. Uomi, and T. Tanaka, "A 1.3- $\mu\text{m}$  GaInNAs/GaAs Single-Quantum-Well Laser Diode with a High Characteristic Temperature over 200 K," *Jpn. J. Appl. Phys.*, vol. 39, pp. 86-87, 2000.
- [33] A. Cho, "Film Deposition by Molecular Beam Techniques," *J. Vac. Sci. Tech.*, vol. 8, pp. S31-S38, 1971.
- [34] A. Cho and J. Arthur, "Molecular Beam Epitaxy," *Prog. Solid-State Chem.*, vol. 10, pp. 157-192, 1975.
- [35] van der Wagt, J. P. A., "Reflection High-Energy Electron Diffraction during Molecular-Beam Epitaxy." Ph.D. Thesis, Stanford University, 1994.
- [36] SVT Associates website: [www.svta.com](http://www.svta.com)
- [37] Oxford Scientific website: [www.oxsci.com](http://www.oxsci.com)
- [38] Applied Epi website: [www.applied-epi.com](http://www.applied-epi.com)
- [39] K. Nanbu, J. Saito, T. Ishikawa, K. Kondo, and A. Shibatomi, "Classification of Surface Defects on GaAs Grown by Molecular Beam Epitaxy," *J. Electrochem. Soc.*, vol. 133, no. 3, pp. 601, 1986.
- [40] C. T. Lee and Y. C. Chou, "Types of oval defects on GaAs grown by MBE," *J. Cryst. Growth*, vol. 91, no. 1-2, pp. 169-172, 1988.
- [41] D. G. Schlom, W. S. Lee, T. Ma, and J. S. Harris, Jr., "Reduction of gallium-related oval defects," *J. Vac. Sci. Tech. B*, vol. 7, no. 2, pp. 296-298, 1989.
- [42] W. Breiland and K. Kileen, "Virtual Interface Method for Extracting Growth Rates and High Temperature Optical Constants from Thin Semiconductor Films using in situ Normal Incidence Reflectance," *J. Appl. Phys.*, vol. 78, no. 11, pp. 6725-6736, 1995.
- [43] G. Li, W. Yuen, K. Toh, L. Eng, S. Lim, and C. Chang-Hasnain, "Accurate Molecular Beam Epitaxial growth of Vertical-Cavity Surface Emitting Laser Using Diode Laser Reflectometry," *IEEE Photon. Tech. Lett.*, vol. 7, pp. 971-973, 1995.
- [44] R. Sacks, R. Sieg, and S. Ringel, "Investigation of the Accuracy of Pyrometric Interferometry in Determining  $\text{Al}_x\text{Ga}_{1-x}\text{As}$  Growth Rates and Compositions," *J. Vac. Sci. Tech. B*, vol. 12, no. 3, pp. 2157-2162, 1996.

- [45] W. Gilmore III and D. Aspnes, "Performance Capabilities of Reflectometers and Ellipsometers for Compositional Analysis During  $\text{Al}_x\text{Ga}_{1-x}\text{As}$  Epitaxy," *Appl. Phys. Lett.*, vol. 66, no. 13, pp. 1617-1619, 1995.
- [46] C. Kuo, M. Boonzaayer, D. Schreder, G. Maracas, and B. Jons, 1996 Ninth International Conference on Molecular Beam Epitaxy, Malibu, CA.
- [47] P. Pinsukanjana, A. Jackson, J. Tofte, K. Maranowski, S. Campbell, J. English, S. Chalmers, L. Coldren, and A. Gossard, "Real-time Simultaneous Optical-Based Flux Monitoring of Al, Ga, and In using Atomic Absorption for Molecular Beam Epitaxy," *J. Vac. Sci. Tech. B*, vol. 14, no. 3, pp. 2147-2150, 1996.
- [48] J. J. Harris, B. A. Joyce, and P. J. Dobson, "Oscillations in the surface structure of Sn-doped GaAs during growth by MBE," *Surf. Sci.*, vol. 103, pp. 90-96, 1981.
- [49] J. P. A. van der Wagt and J. S. Harris, Jr., "Reflection high-energy electron diffraction intensity oscillations during molecular-beam epitaxy on rotating substrates," *J. Vac. Sci. Tech. B*, vol. 12, no. 2, pp. 1236-1238, 1994.
- [50] A. J. SpringThorpe, S. J. Ingreby, B. Emmerstorfer, P. Mandeville, and W. T. Moore, "Measurement of GaAs surface oxide desorption temperatures," *Appl. Phys. Lett.*, vol. 50, no. 2, pp. 77-79, Jan. 12, 1987.
- [51] J. Emsley, *The Elements*. Oxford, UK: Clarendon Press, 1991.
- [52] H. W. L. Phillips, *Annotated Equilibrium Phase Diagrams of Some Aluminium Alloy Systems*. London, UK: The Institute of Metals, 1959.
- [53] E. C. Larkins and J. S. Harris Jr., "Molecular Beam Epitaxy of High Quality GaAs and AlGaAs," in *Molecular Beam Epitaxy: Applications to Key Materials*, R. F. C. Harrow, Ed. Noyes Publications, 1995, pp. 114-274.
- [54] J. M. Garcia, J. P. Silveira, and F. Briones, *Appl. Phys. Lett.*, vol. 77, pp. 409, 2000.
- [55] J. P. Silveira and F. Briones, *J. Cryst. Growth*, vol. 201, pp. 113, 1999.
- [56] Helix Technology Corporation website: [www.helixtechnology.com](http://www.helixtechnology.com)

- [57] V. Kerchner, H. Heinke, U. Birkle, S. Einfeldt, D. Hommel, H. Selke, and P. L. Ryder, "Ion-induced crystal damage during plasma-assisted MBE growth of GaN layers," *Phys. Rev. B*, vol. 58, pp. 15749-15755, 1998.
- [58] Courtesy of SVT Associates.
- [59] Unit Instruments website: [www.celerity.net](http://www.celerity.net)
- [60] R. M. Park, "Low-resistivity p-type ZnSe:N grown by molecular beam epitaxy using a nitrogen free-radical source," *J. Vac. Sci. Tech. A*, vol. 10, pp. 701-704, 1992.
- [61] Spruytte, S., "MBE Growth of Nitride-Arsenides for Long Wavelength Optoelectronics." PhD Thesis, Stanford University, 2001.
- [62] G. B. Stringfellow, *Organometallic vapor-phase epitaxy: theory and practice*. Academic Press Boston, 1989, pp. 123.
- [63] J. Neugebauer and C. G. Van de Walle, "Electronic structure and phase stability of GaAs<sub>1-x</sub>N<sub>x</sub> alloys," *Phys. Rev. B*, vol. 51, pp. 10568-10571, 1995.
- [64] I. H. Ho and G. B. Stringfellow, "Solubility of nitrogen in binary III-V systems," *J. Cryst. Growth*, vol. 178, pp. 1-7, 1997.
- [65] I. Vurgaftman and J. R. Meyer, "Band parameters for III-V compound semiconductors and their alloys," *J. Appl. Phys.*, vol. 89, no. 11, pp. 5815-5875, June 1, 2001.
- [66] K. H. Hellwege, O. Madelun, M. Schulz, and H. Weiss, *Landolt-Börnstein numerical data and functional relationships in science and technology, New Series, Group III: Crystal and solid state physics, Physics of group IV elements and III-V compounds*. Springer-Verlag, 1982, pp. 181-350.
- [67] C. H. P. Lupis, *Chemical Thermodynamics of Materials*. Elsevier Science Publishing Co., Inc., 1983, pp. 76-83.
- [68] G. B. Stringfellow, "Calculation of regular solution interaction parameters in semiconductor solid solutions," *J. Phys. Chem. Solids*, vol. 34, pp. 1749-1750, 1973.
- [69] I. H. Ho and G. B. Stringfellow, 1997 Material Research Society Symposium.
- [70] Y. Qui, S. A. Nikishin, H. Temkin, N. N. Faleev, and Y. A. Kudriavtsev, "Growth of single phase GaAs<sub>1-x</sub>N<sub>x</sub> with high nitrogen concentration by metal-

- organic molecular beam epitaxy," *Appl. Phys. Lett.*, vol. 70, pp. 3242-3245, 1997.
- [71] Y. Qui, S. A. Nikishin, H. Temkin, V. A. Elyukhin, and Y. A. Kudriavtsev, "Thermodynamic considerations in epitaxial growth of GaAs<sub>1-x</sub>N<sub>x</sub> solid solutions," *Appl. Phys. Lett.*, vol. 70, pp. 2831-2833, 1997.
- [72] S. Wei and A. Zunger, "Giant and Composition-Dependent Optical Bowing Coefficient in GaAsN Alloys," *Phys. Rev. Lett.*, vol. 76, no. 4, pp. 664-667, Jan. 22, 1996.
- [73] A. Mascarenhas and Y. Zhang, "Dilute nitride based III-V alloys for laser and solar cell applications," *Current Opinion in Solid State & Materials Science*, vol. 5, pp. 253-259, 2001.
- [74] W. Orellana and A. C. Ferrax, "Ab initio study of substitutional nitrogen in GaAs," *Appl. Phys. Lett.*, vol. 78, no. 9, pp. 1231-1233, Feb. 26, 2001.
- [75] J. D. Perkins, A. Mascarenhas, Y. Zhang, J. F. Geisz, D. J. Friedman, J. M. Olson, and S. R. Kurtz, "Nitrogen-Activated Transitions, Level Repulsion, and Band Gap Reduction in GaAs<sub>1-x</sub>N<sub>x</sub> with x<0.03," *Phys. Rev. Lett.*, vol. 82, no. 16, pp. 3312-3315, Apr. 19, 1999.
- [76] W. Shan, W. Walukiewicz, J. W. Ager III, E. E. Haller, J. F. Geisz, D. J. Friedman, J. M. Olson, and S. R. Kurtz, "Band Anticrossing in GaInNAs Alloys," *Phys. Rev. Lett.*, vol. 82, no. 6, pp. 1221-1224, Feb. 9, 1999.
- [77] Y. Zhang and W. Ge, "Behavior of nitrogen impurities in III-V semiconductors," *J. Lumin.*, vol. 85, pp. 247-260, 2000.
- [78] Y. Zhang, A. Mascarenhas, H. P. Xin, and C. W. Tu, "Formation of an impurity band and its quantum confinement in heavily doped GaAs:N," *Phys. Rev. B*, vol. 61, no. 11, pp. 7479-7482, Mar. 15, 2000.
- [79] Y. Zhang and A. Mascarenhas, "Isoelectronic impurity states in GaAs:N," *Phys. Rev. B*, vol. 61, no. 23, pp. 15562-15564, June 15, 2000.
- [80] Y. Zhang, A. Mascarenhas, H. P. Xin, and C. W. Tu, "Scaling of band-gap reduction in heavily nitrogen doped GaAs," *Phys. Rev. B*, vol. 63, no. 161303-1, pp. 161303-4, 2001.

- [81] Y. Zhang, A. Mascarenhas, J. F. Geisz, H. P. Xin, and C. W. Tu, "Discrete and continuous spectrum of nitrogen-induced bound states in heavily doped GaAs<sub>1-x</sub>N<sub>x</sub>," *Phys. Rev. B*, vol. 62, no. 085205-1, pp. 085205-8, 2001.
- [82] H. M. Cheong, Y. Zhang, A. Mascarenhas, and J. F. Geisz, "Nitrogen-induced levels in GaAs<sub>1-x</sub>N<sub>x</sub> studied with resonant Raman scattering," *Phys. Rev. B*, vol. 61, no. 20, pp. 13687-13690, May 15, 2000.
- [83] E. D. Jones, A. A. Allerman, S. R. Kurtz, N. A. Modine, K. K. Bajaj, S. T. Tozer, and X. Wei, "Photoluminescence-linewidth-derived reduced exciton mass for In<sub>y</sub>Ga<sub>1-y</sub>As<sub>1-x</sub>N<sub>x</sub> alloys," *Phys. Rev. B*, vol. 62, no. 11, pp. 7144-7148, Sept. 15, 2000.
- [84] M. Kozhevnikov, V. Narayanamurti, C. V. Reddy, H. P. Xin, C. W. Tu, A. Mascarenhas, and Y. Zhang, "Evolution of GaAs<sub>1-x</sub>N<sub>x</sub> conduction states and giant Au/GaAs<sub>1-x</sub>N<sub>x</sub> Schottky barrier reduction studied by ballistic electron emission spectroscopy," *Phys. Rev. B*, vol. 61, no. 12, pp. 7861-7863, Mar. 15, 2000.
- [85] E. D. Jones, N. A. Modine, A. A. Allerman, S. R. Kurtz, A. F. Wright, S. T. Tozer, and X. Wei, "Band structure of In<sub>x</sub>Ga<sub>1-x</sub>As<sub>1-y</sub>N<sub>y</sub> alloys and effects of pressure," *Phys. Rev. B*, vol. 60, no. 7, pp. 4430-4433, Aug. 15, 1999.
- [86] S. Wilson, C. R. Brundel, and C. Evans, *Encyclopedia of Materials Characterization: Surfaces, Interfaces, Thin Films*. Boston: Butterworth-Heinemann, 1992.
- [87] P. T. Landsberg, *Recombination in Semiconductors*. Cambridge, UK: Cambridge University Press, 1991.
- [88] D. J. Eaglesham, F. C. Unterwald, and D. C. Jacobson, "Growth Morphology and the Equilibrium Shape: The Role of "Surfactants" in Ge/Si Island Formation," *Phys. Rev. Lett.*, vol. 70, no. 7, pp. 966-969, Feb. 15, 1993.
- [89] R. T. Lee, C. M. Fetzer, S. W. Jun, D. C. Chapman, J. K. Shurtleff, G. B. Stringfellow, Y. W. Ok, and T. Y. Seong, "Enhancement of compositional modulation in GaInP epilayers by the addition of surfactants during organometallic vapor phase epitaxy growth," *J. Cryst. Growth*, vol. 233, no. 3, pp. 490-502, 2001.

- [90] N. Grandjean, J. Massies, and V. H. Etgens, "Delayed relaxation by surfactant action in highly strained III-V semiconductor epitaxial layers," *Phys. Rev. Lett.*, vol. 69, no. 5, Aug. 3, 1992.
- [91] X. Yang, J. B. Heroux, M. J. Jurkovic, and W. I. Wang, "High performance 1.3  $\mu\text{m}$  InGaAsN:Sb/GaAs quantum well lasers grown by molecular beam epitaxy," *J. Vac. Sci. Tech. B*, vol. 18, no. 3, pp. 1484-1487, 2000.
- [92] X. Yang, J. B. Heroux, M. J. Jurkovic, and W. I. Wang, "High-temperature characteristics of 1.3  $\mu\text{m}$  InGaAsN:Sb/GaAs multiple-quantum-well lasers grown by molecular-beam epitaxy," *Appl. Phys. Lett.*, vol. 76, no. 7, pp. 795-797, Feb. 14, 2000.
- [93] X. Yang, J. B. Heroux, L. F. Mei, and W. I. Wang, "InGaAsNSb/GaAs quantum wells for 1.55  $\mu\text{m}$  lasers grown by molecular-beam epitaxy," *Appl. Phys. Lett.*, vol. 78, no. 26, pp. 4068-4070, June 25, 2001.
- [94] H. Shimizu, K. Kumada, S. Uchiyama, and A. Kasukawa, "1.2 $\mu\text{m}$  range GaInAs SQW lasers using Sb as surfactant," *Electron. Lett.*, vol. 36, no. 16, pp. 1379-1381, Aug. 3, 2000.
- [95] V. Gambin, W. Ha, M. Wistey, S. Kim, and J. S. Harris, 2001 MRS Proceedings.
- [96] Y. P. Varshni, *Physica*, vol. 34, pp. 149, 1967.
- [97] L. Vina, S. Logothetidis, and M. Cardona, *Phys. Rev. B*, vol. 30, pp. 1979, 1984.
- [98] H. Shen, S. H. Pan, Z. Hang, J. Leng, F. H. Pollak, J. M. Woodall, and R. N. Sacks, "Photoreflectance of GaAs and Ga<sub>0.82</sub>Al<sub>0.18</sub>As at Elevated Temperatures up to 600°C.," *Appl. Phys. Lett.*, vol. 53, no. 12, pp. 1080-1082, 1988.
- [99] H. Teisseyere, P. Perlin, T. Suski, I. Grzegory, S. Porowski, J. Jun, A. Pietraszko, and T. D. Moustakas, "Temperature dependence of the energy gap in GaN bulk single crystals and epitaxial layer," *J. Appl. Phys.*, vol. 76, pp. 2429, 1994.
- [100] T. Matsukawa, R. Shimizu, K. Harada, and T. Kato, "Investigation of kilovolt electron energy dissipation in solids (by beam-induced currents in MOS capacitor)," *J. Appl. Phys.*, vol. 45, pp. 733, 1974.

- [101] K. Siegbahn, C. Nordling, A. Fahlman, R. Nordberg, K. Hamrin, J. Hedman, G. Johansson, T. Bergmark, S. Karlsson, I. Lindgren, and B. Lindberg, *ESCA Atomic, Molecular and Solid State Structure Studied by Means of Electron Spectroscopy*. Uppsala: Almpuist and Wiksells, 1967.
- [102] M. P. Seah and W. A. Dench, "Quantitative Electron Spectroscopy of Surfaces: Standard Data Base for Electron Inelastic Mean Free Path in Solids," *Surf. Interf. Anal.*, vol. 1, pp. 2-11, 1979.
- [103] B. E. Warren, *X-Ray Diffraction*. New York: Dover Publication, Inc., 1990.
- [104] K. T. Faber and K. J. Malloy, *The mechanical properties of semiconductors, semiconductors and semimetals Volume 37*. Academic press, Inc., 1992, pp. 31.
- [105] R. Singh, D. Doppalapudi, T. D. Moustakas, and L. T. Romano, "Phase separation in InGaN thick films and formation of InGaN/GaN double heterostructures in the entire alloy composition," *Appl. Phys. Lett.*, vol. 70, no. 9, pp. 1089, Mar. 3, 1997.
- [106] I. A. Buyanova, G. Pozina, P. N. Hai, N. Q. Thinh, J. P. Bergman, W. M. Chen, H. P. Xin, and C. W. Tu, "Mechanism for rapid thermal annealing improvements in undoped GaN<sub>x</sub>As<sub>1-x</sub>/GaAs structures grown by molecular beam epitaxy," *Appl. Phys. Lett.*, vol. 77, no. 15, pp. 2325-2327, Oct. 9, 2000.
- [107] D. Kwon, R. Kaplar, S. Ringel, A. A. Allerman, S. Kurtz, and E. D. Jones, "Deep levels in *p*-type InGaAsN lattice matched to GaAs," *Appl. Phys. Lett.*, vol. 74, no. 19, pp. 2830-2832, May 10, 1999.
- [108] N. Thinh, I. Buyanova, P. Hai, W. Chen, H. P. Xin, and C. W. Tu, "Signature of an intrinsic point defect in GaN<sub>x</sub>As<sub>1-x</sub>," *Phys. Rev. B*, vol. 63, no. 033203-1, pp. 033203-4, 2001.
- [109] L. Wei, M. Pessa, T. Ahlgren, and J. Decker, "Origin of improved luminescence efficiency after annealing of Ga(In)NAs materials grown by molecular-beam epitaxy," *Appl. Phys. Lett.*, vol. 79, no. 8, pp. 1094-1096, Aug. 20, 2001.
- [110] P. Krispin, S. G. Spruytte, J. S. Harris, and K. H. Ploog, "Deep-level defects in MBE-grown Ga(As,N) layers," *Physica B*, vol. 308-310, pp. 870-873, Dec., 2001.

- [111] P. Krispin, S. Spruytte, J. S. Harris, and K. Ploog, "Admittance dispersion of  $n$ -type GaAs/Ga(As,N)/GaAs heterostructures grown by molecular beam epitaxy," *J. Appl. Phys.*, vol. 90, no. 5, pp. 2405-2410, Sept. 1, 2001.
- [112] P. Krispin, S. G. Spruytte, J. S. Harris, and K. H. Ploog, "Electron traps in Ga(As,N) layers grown by molecular-beam epitaxy," *Appl. Phys. Lett.*, vol. 80, no. 12, pp. 2120-2122, Mar. 25, 2002.
- [113] P. Krispin, V. Gambin, J. S. Harris, and K. Ploog, "Ga(As,N) layers in the dilute N limit studied by depth-resolved capacitance spectroscopy," *to be published*, 2002.
- [114] I. A. Buyanova, W. M. Chen, and B. Monemar, "Electronic Properties of Ga(In)NAs Alloys," *MRS Internet Journal Nitride Semiconductor Research*, vol. 6, no. 2, pp. 1-19, 2001.
- [115] K. Kim and A. Zunger, "Spatial Correlations in GaInAsN Alloys and their Effects on Band-Gap Enhancement and Electron Localization," *Phys. Rev. Lett.*, vol. 86, no. 12, pp. 2609-2612, Mar. 19, 2001.
- [116] S. Kurtz, J. Webb, L. Gedvilas, D. Friedman, J. Geisz, J. Olson, R. King, D. Joslin, and N. Karam, "Structural changes during annealing of GaInAsN," *Appl. Phys. Lett.*, vol. 78, no. 6, pp. 748-750, Feb. 5, 2001.
- [117] E. A. Stern, "Theory of the Extended X-Ray-Absorption Fine Structure," *Phys. Rev. B*, vol. 20, no. 9, pp. 3027-3037, Oct. 15, 1974.
- [118] P. A. Lee, P. H. Citrin, P. Eisenberger, and B. M. Kincaid, "Extended X-ray Absorption Fine Structure-Its Strengths and Limitations as a Structural Tool," *Rev. Mod. Phys.*, vol. 53, no. 4, pp. 769-806, Oct., 1981.
- [119] P. A. Lee and J. B. Pendry, *Phys. Rev. B*, vol. 11, pp. 2795-2811, 1975.
- [120] Courtesy of Spring 8, Hyogo, Japan, 2002.
- [121] B. K. Teo, *EXAFS: Basic Principles and Data Analysis*. Berlin: Springer-Verlag, 1986.
- [122] J. Stohr, *NEXAFS Spectroscopy*. Berlin: Springer, 1992.
- [123] V. Lordi, V. Gambin, S. Friedrich, T. Takizawa, K. Uno, and J. S. Harris, *to be published*, 2002.

- [124] S. Friedrich, T. Funk, O. Drury, S. E. Labov, and S. P. Cramer, "A multichannel superconducting soft x-ray spectrometer for high-resolution spectroscopy of dilute samples," *Rev. Sci. Instrum.*, vol. 73, pp. 1629-1631, 2002.
- [125] K. Segall, C. Wilson, L. Frunzio, L. Li, S. Friedrich, M. C. Gaidis, D. E. Prober, A. E. Szymkowiak, and S. H. Moseley, "Noise mechanisms in superconducting tunnel-junction detectors," *Appl. Phys. Lett.*, vol. 76, no. 26, pp. 3998-4000, June 26, 2000.
- [126] J. W. Matthews and A. E. Blakeslee, "Defects in epitaxial multilayers I. Misfit dislocations," *J. Cryst. Growth*, vol. 27, pp. 118-125, 1974.
- [127] R. Hull and J. C. Bean, "Misfit dislocations in lattice-mismatched epitaxial films," *CRC Solid State and Material Science*, vol. 17, pp. 507-546, 1992.
- [128] K. Hiramoto, M. Sagawa, and T. Toyonaka, "Strain-compensation effect on the reduction of lattice distortion in InGaAs/(In)GaAs(P) strained quantum-well structures on GaAs substrates," *Jpn. J. Appl. Phys.*, vol. 36, pp. L1632-L1633, 1997.
- [129] J. S. Harris, Jr., "Tunable long-wavelength vertical-cavity lasers: the engine of next generation optical networks?," *IEEE J. Select. Topics Quantum Electron.*, vol. 6, no. 6, pp. 1145-1160, Dec., 2000.
- [130] W. Ha, V. Gambin, M. Wistey, S. Bank, S. Kim, and J. S. Harris, 2001 Conference Proceedings LEOS, San Diego, CA.
- [131] W. Ha, V. Gambin, M. Wistey, S. Bank, H. Yuen, S. Kim, and J. S. Harris, "Long wavelength GaInNAsSb/GaNAsSb multiple quantum well lasers," *Electron. Lett.*, vol. 38, pp. 277-278, Mar., 2002.